UNIVERSITY OF ADELAIDE LIBRARY
31.3.98

The University of Adelaide

Department of Mechanical Engineering

Mixing and Combustion in Precessing Jet Flows

Ph.D. Thesis

submitted by

Gregory John Robert Newbold

March 1998

Abstract

A wide range of qualitative and quantitative experimental techniques are used to investigate the effect of jet precession on the mixing and combustion characteristics of a simple turbulent jet flow. Here precession of the jet flow results from the addition of a chamber section downstream from the throat of the simple jet which issues from a sharp edged orifice. The chamber generates a fluid mechanical instability so that the emerging jet precesses about the nozzle axis. The nozzle is termed the fluidic precessing jet (FPJ) nozzle. This nozzle has been the subject of ongoing research at the University of Adelaide because of the benefits that FPJ gas flames offer to industry.

The flow and flame characteristics associated with FPJ flows are compared with those of simple turbulent jets by use of laser sheet visualisation, particle image velocimetry and mixture field diagnostics for non-reacting flows and by use of high-speed flame visualisation and reaction zone imaging for reacting flows.

The non-reacting jet flow emerging from the FPJ nozzle is seen to form large-scale roller structures that are responsible for entrainment of significant ambient fluid. Velocity measurements demonstrate that the flow velocities in the region immediately downstream from the nozzle are dramatically reduced, by two orders of magnitude relative to the jet throat. The mixing characteristics throughout a jet produced by the sharp edged orifice are shown to be different from that produced by a nozzle with a smooth contraction. Measurements of the mean and RMS jet concentration fields, concentration half-widths and centre-line unmixedness, intermittency, integral length-scale and scalar mixing rate are compared for the simple jet flow and the FPJ flow. The findings of this comparison support the conclusion that the effect of precession is to change the underlying structure of the turbulence in a manner that reduces the magnitude of the local strain rate in the flow. The results also demonstrate conclusively that *the effect of precession of a jet is to enhance large-scale engulfment of ambient fluid and to suppress fine-scale mixing between the jet and ambient fluid streams.*

Mixing and combustion characteristics of FPJ flames have been considered in relation to the possible stabilisation mechanisms. Large-scale buoyant structures, which propagate through the unconfined FPJ flames, are concluded to be the result of, rather than the cause of, the flame stabilisation. It has been demonstrated that combustion occurs in reaction zones that are located at the edge of the flow field. The instantaneous structure of the reaction field can be seen qualitatively to coincide with the structure of the flammable region in the non-reacting flow case. The reaction layers are thick compared with the thickness of dissipation layers in the region in which reaction occurs. High values of scalar dissipation are only found within the jet as it emerges from the FPJ nozzle, which is well upstream from the mean stabilisation point.

The results demonstrate that *the physical mechanisms discussed here which have been proposed for simple jet flame stabilisation, other than those which include the existence of a premixed flame zone, are inappropriate for the fluidic precessing jet diffusion flame*. That is, stabilisation depends upon the mixing characteristics upstream from the reaction zone providing regions of sufficiently low velocity that are within the flammability limits.

Mixing and combustion characteristics of FPJ flames have been considered in relation to the reduced NO_x emissions and increased emissivity that have been measured elsewhere. The strain rate at the tip of the flame has been measured using local flame conditions for the FPJ and shown to be an order of magnitude lower than the local strain in simple jet flows based on calculations from data reported in the literature. It is demonstrated that the effect of radiation on the temperature of jet flames can become significant when the structure of jet turbulence and hence the mixing characteristics have been modified to reduce the characteristic strain rate of the reacting flow and thereby promote soot formation. A mechanism by which NO_x emissions can be reduced and simultaneously radiant heat transfer increased by proper control of turbulent mixing parameters has therefore been demonstrated.

Contents

1. Introduction

2. Experimental Apparatus and Techniques

3. Mixing in Precessing Jet Flows

4. Flame Stabilisation in Precessing Jet Flames

5. The Influence of Mixing on Sooting and NO_x Emission Characteristics of Precessing Jet Flames

List of Figures

Notation

Abbreviations

FPJ	Fluidic precessing jet
MPJ	Mechanical precessing jet

Variable Quantities

c	Instantaneous mixed fluid concentration
d	Jet throat diameter
d_c	FPJ nozzle centre body diameter
d_1	FPJ nozzle inlet diameter
d_2	FPJ nozzle exit diameter
d_{eq}	FPJ nozzle equivalent exit diameter
$d_{\frac{1}{2}}$	Jet concentration half-width
D	FPJ nozzle chamber internal diameter (The characteristic FPJ nozzle dimension)
D	Molecular diffusion coefficient
f	Frequency of large-scale puffing motion in buoyant flames
f_p	Frequency of precessional motion
g	Gravitational constant
h	Step height of the sudden expansion at the inlet to the FPJ chamber section $h = (D - d_1) / 2$
I	Intermittency
I	Intermittency flame length
l	Flow length scale
l_{xx}	Integral length-scale of the jet concentration fluctuations
L	FPJ nozzle chamber length

L_c	FPJ nozzle chamber length from the upstream orifice to the back face of the centre-body
M	Jet source momentum
Q	Flame thermal output
r	Radial coordinate
R	Correlation coefficient of the jet concentration fluctuations
S	Celerity (speed of a large-scale flame structure)
t	Time
u	Fluid velocity
U	Bulk mean fluid velocity
w_c	FPJ nozzle centre-body length
x	Stream-wise (axial) coordinate
x_0	Virtual origin of the jet concentration measurements
x_0^*	Virtual origin of the jet fluid concentration half-width
X	Flame length
y	Cross-stream coordinate - in the image plane
z	Cross-stream coordinate - out of the image plane
χ	Scalar dissipation $= 2\mathrm{D}\nabla^2\xi$
ε	Kinetic energy dissipation rate
λ	Resolution length-scale
λ_b	Batchelor length-scale $= \left(\frac{\varepsilon}{\nu\mathrm{D}}\right)^{-\frac{1}{4}}$
λ_k	Kolmogorov length-scale $= \left(\frac{\varepsilon}{\nu^3}\right)^{-\frac{1}{4}}$
ν	Kinematic viscosity of a fluid
θ	Angle of the jet exiting the MPJ nozzle

ρ	Fluid density
τ_b	Batchelor mean passage frequency $= \dfrac{\lambda_b}{u}$
τ_G	Residence time of the gases in a flame
ξ	Jet concentration/conserved scalar mixture fraction
ψ	Intermittency variable

Non-dimensional Parameters

Re	Reynolds number $= \dfrac{ud}{\nu}$
Sc	Schmidt number $= \dfrac{\nu}{\mathrm{D}}$
St_d	Strouhal number of precession of the MPJ nozzle $= \dfrac{f_p d}{u_d}$
St_h	Strouhal number of precession for the FPJ nozzle based on step height, h, $= \dfrac{f_p h}{u_{d_1}}$
St_M	Strouhal number of precession for the FPJ nozzle based on jet source momentum, M, $= \dfrac{f_p \sqrt{\rho} D^2}{\sqrt{M}}$

Subscripts

d	Denotes quantity at the simple jet throat
d_1	Denotes quantity at the upstream throat of the FPJ nozzle
0	Denotes quantity at the source
∞	Denotes quantity in the far-field/ambient
i,j	Denotes quantity at a given pixel
x,y,z	Denotes quantity at a given geometric point

Statement of Originality

The material in this thesis is original and has not been submitted or accepted for the award of a degree or diploma at any other university and, to the best of my knowledge and belief, the thesis contains no material previously published or written by another person except where due reference is made in the text of the thesis.

Greg Newbold

Permission to Copy

The author consents to the thesis being made available for loan and photocopying provided that the thesis is accepted for the award of the degree.

Greg Newbold

Acknowledgment

The valuable contribution made to this project by many people is greatly appreciated and will be long remembered. Dr. Graham Nathan and Professor Sam Luxton have provided enthusiastic supervision and strong academic support for this project. This work has benefited greatly from the active participation of Mr. David Nobes and Dr. Zeyad Alwahabi in the conduct of laboratory experiments and discussing the work.

The wide variety of experimental equipment has been made available through the shared resources of the Jet and Flame Research Group in the Department of Mechanical Engineering and the Department of Chemical Engineering. During the course of this project each team member of the group has freely made time for valuable discussions, particularly by Dr. Gerald Schneider, Mr. Neil Smith and Mr. Steven Hill.

The work that is presented here has made use of new experimental facilities and diagnostic techniques that have been established through the efforts of the technical staff in the Department of Mechanical Engineering. The contributions made by all the technical staff, in particular Mr Ron Jager, Mr. Craig Price and Mr. Anthony Sherry in the Mechanical Workshop and Mr. Silvio de Ieso, Mr. Herwig Bode and Mr. George Osborne in the Instrumentation Workshop, are appreciated. The development of image analysis tools has been made possible by Mr Jonathan May and Mr. Wayne Johnson. The staff and student members of the Department of Mechanical Engineering are all deserving of thanks.

This project has been made possible by the financial support provided by the Australian Postgraduate Research Award scheme.

Thank you.

Greg Newbold

March 1998

To my son, Jarrad

UNIVERSITY OF ADELAIDE LIBRARY

Chapter 1

1. Introduction

1.1. Mixing and Combustion

"It has become standard practise to state that in the case of premixed homogeneous combustible gas mixtures that reaction rate phenomena control and ***in initially unmixed fuel-oxidiser systems that diffusion phenomenon control****... In the case of laminar flames, and indeed in most aspects of turbulent flame propagation, it should be emphasised that it is the diffusion of heat (and mass) that causes the flame to propagate*" (Glassman, 1987). Thus the combustion process in turbulent non-premixed (diffusion) flames is "mixing-limited" and chemical kinetic effects may be assumed to be sufficiently fast to be considered of second order importance.

Recent experimental studies in diffusion flames have investigated mixing of the fuel with the oxidant and the interaction between this mixing field, the velocity field and the reaction zone (flame). These studies have considered the physical characteristics of fundamental combustion phenomena, such as the existence and role of organised vortical structures (eddies), extinction phenomenon, the propagation of the flame through the flow field (flame stabilisation) and the emission of pollutant species from the flame, notably the oxides of nitrogen (NO_x). Models which seek to predict flame behaviour should therefore be assessed not only on their prediction of flame behaviour but also on the consistency of the physical mechanisms they propose with the known flow field and flame zone structure.

In the present thesis the mixing and combustion within the flow produced by a fluidic precessing jet (FPJ) burner (Nathan, 1988), which has recently been patented (Luxton *et al.*

1991), are investigated. Precessing jet flows and flames have been found to be of considerable benefit to industries that employ high temperature gas flames because the heat transfer characteristics tend to be well suited to process requirements. Specific benefits are improved flame stability, lower NO_x emissions, increased productivity and enhanced product quality. However precessing jets are a recently discovered phenomenon and very few detailed investigations of their characteristics have been conducted. Their importance in the broader field of combustion is that their commercial success clearly demonstrates that significant benefits can be derived by changing the mixing process.

Nathan (1988) demonstrated that jet precession provides substantial improvements in flame stability. The blowout velocity was measured to be increased and the lift-off height reduced by an order of magnitude. While a rapid reduction in mean velocity associated with the rapid initial spread of the jet has been linked to the improved flame stability, no detailed investigation is available to explain the stabilisation of FPJ flames. As a first step in this process, the stabilisation models that have been proposed for simple turbulent jet diffusion flames are reviewed.

Soot formation has been deduced to be important in precessing jet flames. Nathan *et al.* (1996) measured an increase in the radiant fraction from precessing jet flames and found that this correlates with reduced NO_x emissions. Nathan and Luxton (1992) also measured an increase in radiant energy in the visible and near IR region by an order of magnitude in comparison with a commercial swirl burner and deduced that soot formation is significant in FPJ flames.

The present work describes an experimental investigation designed to quantify the behaviour of the mixing field and the characteristics of the subsequent combustion in precessing jet flows. A wide range of non-reacting and reacting experimental techniques have been used to investigate the effect of precession of a jet on mixing. Many published investigations of jets and jet flames are considered here that seek to relate the mixing processes to combustion phenomena. The applicability of flame stabilisation, soot and NO_x models, proposed for jet flames, to precessing jet flames is considered.

1.2. Mixing Characteristics of Free Turbulent Jet Diffusion Flames

1.2.1. Mixing and Stabilisation in Jet Flames

Simple turbulent jet diffusion flames from axisymmetric nozzles are stabilised in an annular region at the burner rim when the exit velocity is sufficiently low. With increases in the jet velocity a critical value is reached where the flame "lifts-off" from the burner rim and at a second critical velocity "blowout" occurs. Several different flame stabilisation mechanisms have been proposed to predict, in part, the observed lift-off height or blowout velocity. These predictions employ assumptions concerning physical mixing and combustion phenomena. Additional models attempt to explain the qualitative structure of the reaction zone that has been observed in turbulent jet diffusion flames.

Vanquickenborne and van Tiggelen (1966) propose that the base of a lifted diffusion flame is stabilised in a turbulent premixed flame zone. In their model the flame is stabilised where the maximum turbulent premixed flame velocity just balances the local mean gas velocity. It was found from measurements in a non-burning mixing study that the locations at which the lifted flame stabilises, on average, are in an annular region at the outer edge of the jet flow where the time-averaged fuel-air composition is approximately stoichiometric. Increasing turbulence intensity at the region of stabilisation was found to be associated with an increasing turbulent burning velocity. Blowout is predicted to occur where the turbulent burning velocity in the stoichiometric region is not sufficiently high to balance the mean gas velocity there. It is suggested that the blowout condition will occur at a downstream location where the stoichiometric contour reaches its maximum radial extent and the mean gas velocity increases both upstream and downstream along the contour.

Peters and Williams (1983) have developed an alternative stabilisation model following the theoretical analysis which concluded that there is insufficient time for a significant quantity of fuel to become molecularly mixed to stoichiometry at the stabilisation point in a lifted flame and hence that premixed models are invalid. They propose instead that a turbulent diffusion flame is an ensemble of laminar diffusion flamelets, which are stretched and contorted by the turbulence in the flow. These flamelets are assumed to be small relative to the local turbulence structure (ie. smaller than the Kolmogorov scale, λ_k) so that laminar conditions are assumed to exist in the flame zone. In the flamelet model, reactions are extinguished if the local instantaneous strain rate (which can be related to the scalar gradient) to which it is subjected becomes too large and heat conduction out from the reaction zone exceeds heat generation due to reaction. Agreement is found between the model that was developed and measured values of the lift-off height found by Horch (1978).

Broadwell *et al.* (1984) propose yet another stabilisation mechanism involving upstream propagation of the flame between large-scale structures spanning the full width of the jet. Such structures have been observed in non-reacting jet flows by Dimotakis *et al.* (1983) and Dahm and Dimotakis (1987). In this model, for blowout, hot reaction products are ejected from a combusting structure and reentrained by the next upstream non-combusting structure and rapidly mixed with jet fluid, where they act as a hot ignition source. It is a necessary condition for stable combustion that there is sufficient time for the fuel and air to achieve a combustible mixture before the temperature and radical species population drops below some critical value due to mixing within the non-reacting structure. Blowout occurs when the ignition time is insufficient for this to occur. Agreement is found between the prediction of blowout and the experimental results of Kalghatgi (1981). Lifting of the flame base is predicted to occur when the reaction products are not mixed with the unburned jet fluid rapidly enough to ignite the next upstream non-burning structure. However, Pitts (1989) has shown that the predicted dependencies for lift-off are inconsistent with the experimental findings of Kalghatgi (1984).

Byggstøyl and Magnussen (1985) have also developed a model for stabilisation, in this case based on local extinction of fine scale structures in a non-premixed flame. Extinction is proposed to occur based on conditions in those smallest eddies throughout the flow that contain homogenously mixed fuel and air. These eddies are closely related to the Kolmogorov scales. The condition for extinction in the fine scale structures is that there is insufficient residence time for the complete combustion of the mixture. Predicted values are in agreement with the experimental results obtained by Horch (1978).

Pitts (1988) has conducted a review of these jet diffusion flame stabilisation models. The models were critically assessed on the basis that they predict the experimental lift-off heights and blowout velocities and *"that the proposed physical mechanisms are consistent with the known turbulence structure"*. Despite the (partial) success of all of the above models in predictions of the lift-off height and blowout velocity they all contained assumptions regarding the fundamental combusting structure which are now known or were demonstrated to be incorrect. Later work (see below) provides a more up-to-date picture of flame stabilisation phenomenon in turbulent jet diffusion flames.

Bilger (1988) has proposed a quasi-equilibrium distributed reaction (QEDR) model, where reaction is fully described by two variables, the concentration of a scalar and the scalar gradient (scalar dissipation). Application of this model to experimental data for a mixing study of a non-reacting Freon-12 jet in air resulted in the prediction that qualitatively agree with the OH-LIF study of Seitzman *et al.* (1990) in an hydrogen jet diffusion flame. The reaction zone aligns with the stoichiometric contour near equilibrium and shifts to align with the peak scalar dissipation for departures far from equilibrium. Their study shows that the reaction is confined to thin zones at the edge of the fuel jet, except in the vicinity of the flame tip where combustion occurs throughout a large diffuse structure. Buch *et al.* (1992) has since demonstrated that the QEDR model, in fact, predicts that the species reaction rate fields are composed entirely of locally layer–like structures throughout the entire length of the flame, based on the application of the model to experimental data of mixture fraction in a propane jet in air.

Dahm *et al.* (1991) and Buch and Dahm (1996) have made *x,y,z,t* concentration measurement in the far field of a turbulent jet and show that mixing occurs in locally one-dimensional layer-like structures. Bish and Dahm (1995) have proposed that the chemical state of combustion is related to the mixing state of a conserved scalar, which suggests that the reaction layers are confined to these thin layer-like structures so that the underlying chemical species fields will also be locally one-dimensional. Their strained diffusion and reaction layer (SDRL) model predicts that the reaction field will be layer-like near equilibrium conditions and broader (distributed) reaction zones for equilibrium departures that also qualitatively agrees with the OH-LIF study of Seitzman *et al.* (1990).

Simultaneous determination of the local flow field, reaction zone and temperature in turbulent jet diffusion flames permits validation of the combustion mechanisms proposed in the above mentioned studies. This has been made possible by the use of multi-species (non-intrusive) imaging of fuel species, reaction intermediaries, such as CH and OH radicals, or temperature.

Namazian *et al.* (1988) have conducted simultaneous measurements at the base of a turbulent methane flame. They imaged the fuel (CH_4) and the reaction zone (CH) and showed that combustion occurs in a thin annular reaction zone surrounding the fuel jet with an overall thickness many times greater than the scale of the smallest turbulent structure. The fuel mass fraction across the reaction zone in the region of flame stabilisation is approximately within the flammability limits of the fuel, suggesting that a premixed model is appropriate. In another investigation in methane flames, Schefer *et al.* (1994a) have simultaneously imaged the fuel (CH_4), the reaction zone (CH) and the temperature. They conclude that the scalar gradient (scalar dissipation) is not important because the flame zone falls well outside the region where this parameter is high enough to cause extinction. These observations indicate that flamelet theories may be discounted in diffusion flames of methane. They also found that the instantaneous temperature measured immediately upstream from the location of flame stabilisation is near to ambient for these open flames, demonstrating that preheating of the reactants is not significant in the stabilisation process. Their perspective on the mechanism for flame stabilisation is that *"flame propagation is a consequence of large-scale turbulent motion, which establishes the local turbulence field through which the flame can propagate"*.

Schefer *et al.* (1994b) imaged the fuel (CH_4) and reaction zone (CH) simultaneously at two closely spaced instants in time in unconfined methane flames. Two images were collected at closely spaced time steps and revealed that large-scale Kelvin-Helmholtz structures in the central fuel jet act to push the flame stabilisation point far downstream. Further images showing the influence of these structures in the jet of the flame are found in Eickhoff and Winandy (1985) and Chen *et al.* (1986 and 1988). Occasional outward protrusions of high concentration jet fluid (fuel) interfere with the reaction zone and the flame stabilisation point convects downstream with the structure. Extinction of the flame zone has been observed at both the upstream and downstream edge of the large-scale structures. As the structure convects downstream flame propagation past the extinct zone becomes possible and so the flame stabilisation point shifts rapidly upstream and the flame propagates through a premixed zone. The velocity at the mean location of the stabilisation point roughly coincides with the maximum turbulent burning speed for the fuel. More recently Muñiz and Mungal (1997) have shown that the flame front in a turbulent jet diffusion flame propagates in regions where the local velocity equals the maximum laminar flame speed, and does not exceed three times the laminar flame speed.

In order to determine the extent to which the various combustion models developed for turbulent jet diffusion flames are applicable to the FPJ flame, it is necessary to investigate the interactions or coupling between the mixing field, the velocity field and the reaction zone. It is important to consider the velocity field, the scalar field, the scalar dissipation, the existence of central jet structures and the dynamics of large-scale structures within the flame.

1.2.2. Mixing and Soot Formation in Jet Flames

Becker and Yamazaki (1977) suggest that mixing controls soot formation and burnout (oxidation) in turbulent propane flames. They show that the maximum centre-line soot concentration in propane flames increases as conditions progress from momentum driven conditions to buoyancy driven conditions.

Mixing effects on soot volume fraction and flame temperature in acetylene turbulent jet diffusion flames have been investigated by Kent and Bastin (1984). They observe that at low strain rates soot formation and oxidation are controlled by the mixing rate and at high strain rate by soot kinetics. Soot volume fraction profiles scale with respect to the flame mixing time d/u_0, defined by the jet throat velocity u_0 and diameter d, being the inverse strain rate. That is, low strain rate correlates with high soot volume fraction. Soot oxidation (burnout) is mainly mixing rate dependent but temperature and species concentrations also play a significant role. A balance between the soot production and soot oxidation rates is necessary for a non-smoking flame. At sufficiently low temperature (<1100°C) the oxidation of soot can be quenched and the flame will emit smoke.

1.2.3. Mixing and NO_x Emissions in Jet Flames

Turns and Myhr (1991) have proposed that NO_x is predominantly formed in large-scale structures at the flame tip. They formulated a time-temperature relation for the global flame NO_x emissions that collapses emissions data determined for jet flames firing a wide variety of hydrocarbon fuels to a single line. A characteristic flame temperature is derived from the adiabatic flame temperature, with consideration of radiant heat losses from the flame as a whole, and a residence time of the gases at high temperature is determined from the flame volume, which is assumed to be a cone of hot gases.

Røkke *et al.* (1992 and 1994) has derived scaling relations for the NO_x emissions from turbulent jet diffusion flames based on a strained laminar diffusion flamelet model that also collapses emissions data determined for jet flames firing a wide variety of hydrocarbon fuels to a single line. Simplified reaction models are developed that determine the relative contributions of thermal (Zeldovich) and prompt NO_x as functions of the scalar dissipation, which is related to the flame bulk strain rate. The prompt mechanism dominates for flames near to extinction, where strain rate is high the fuel consumption zone is broadened and peak temperatures are reduced, and the thermal mechanism dominates for gentle flames where increased NO_x emissions result.

The principle difference between these NO_x emission models is that the reduction in the flame temperature due to radiant loss is not considered to be important by Røkke *et al.* (1992), but is crucial the scaling relation of Turns and Myhr (1991). In order to consider the applicability of the NO_x models for turbulent jet diffusion flames to the FPJ flame, it is necessary to consider a comparison of the residence time and strain rate.

1.3. Application of the Fluidic Precessing Jet Nozzle

A gaseous fuel burner employing the fluidic precessing jet (FPJ) nozzle has been developed in the University of Adelaide, Australia, and is being marketed as the Gyro-Therm burner by Fuel and Combustion Technology International. The FPJ burner has been found to reduce simultaneously both pollutant emissions and specific fuel consumption in rotary kilns (Manias and Nathan, 1993 and 1994), and this provides the client company with a positive return on investment. Similar benefits have been achieved in the alumina industry (Jenkins *et al.*, 1995) and potential also exists to utilise the technology in power station applications (Ward *et al.*, 1990). Development is in progress for further application in metallurgical processes, glass and lime manufacture and the steel industry.

The Gyro-Therm burner throughput can be tailored to suit a wide range of industrial applications. Capacities range from tens of kilowatts to more than one hundred megawatts (Figure 1.1). The burner operates stably over a broad range of driving pressures (up to 700kPa) and thus allows a turndown ratio in excess of 10:1 to be achieved in kiln applications. Laboratory trials in a 30kW furnace show that simulated blast furnace gas can be burned stably (Nathan and Luxton, 1991a). Information on the in-service performance of the burner, operating in the cement industry both in Australia and overseas, may be found in Manias and Nathan (1993 and 1994). They summarise the major advantages of the burner for cement clinker production in rotary kilns as being:

- reduction of NO_x emissions by 30-70% while maintaining low CO emissions, in contrast to conventional burner designs where high CO normally correlates with low NO_x,
- increased kiln output, typically 5% more product, through better control of heat transfer near to the front of the kiln,

- reduced specific fuel consumption, by up to 8%, through more a efficient thermal profile, deduced to result from increased radiant het transfer, which closely matches the needs of the process,
- significant improvement in product quality, also through better control of heat transfer near the front of the kiln, and
- additional savings of fuel and electricity through reduction of the primary air requirements in the kiln and improvement of the grinding characteristics of the clinker produced.

Conventional burner designs use about 10% primary air to achieve mixing through high momentum. In rotary kilns there is a thermodynamic penalty of about 3% associated with replacing hot secondary air with cold primary air.

The above dramatic benefits all result from the changes to the combustion process and are solely the result of the modifications in the mixing characteristics of the fuel jet caused by the jet precession. The elucidation of these changes is the motivation for the present study.

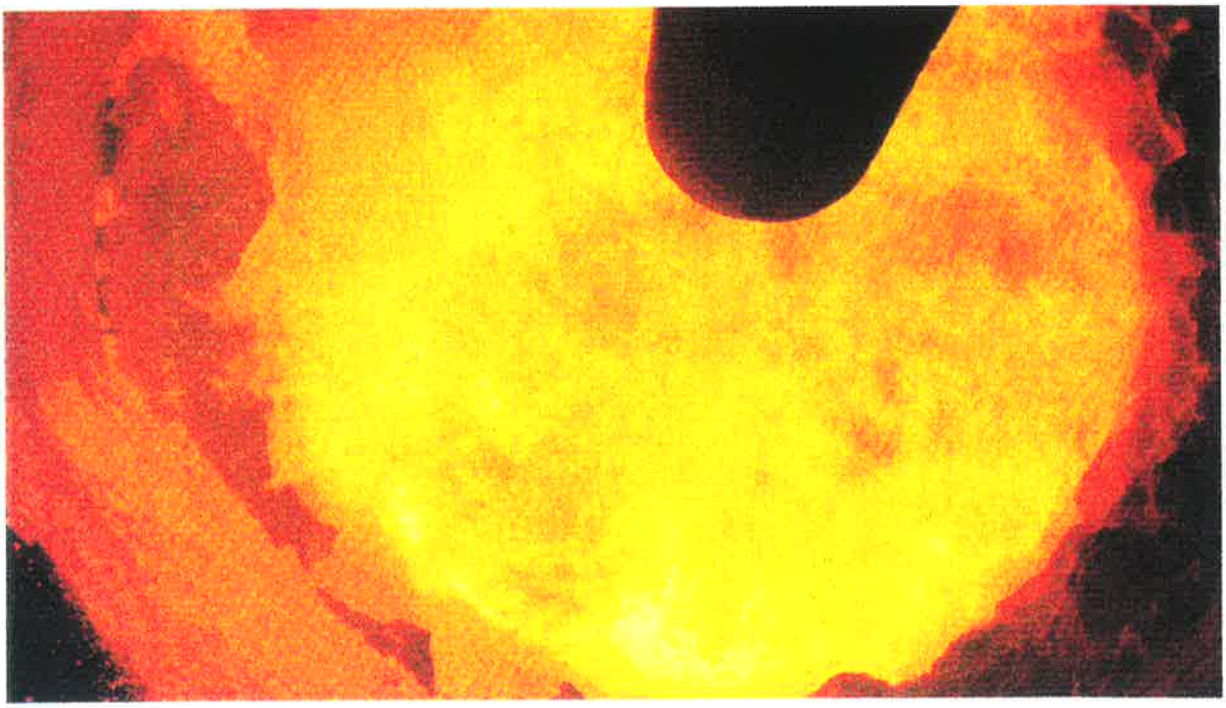

Figure 1.1 The flame produced by a FPJ gas burner in a 100MW nominal capacity rotary cement kiln. Kiln No. 8, Geelong Cement, Australia. NOx reductions of 50% and fuel savings of 5% were achieved (Rapson *et al.*, 1995).

1.4. Mixing in Precessing Jet Flames

Precession is the term used to describe the motion of a jet about an axis other than its own. The term was originally applied to the orbital motion of planets. In the case of the FPJ nozzle the emerging jet is directed at an angle to the nozzle axis and precesses about the nozzle axis (Figure 1.2). The precessional motion is characterised by a dimensionless *Strouhal number of precession* relating the precessional frequency of the jet to the jet velocity and geometric nozzle size. Details of the FPJ nozzle, the flow within it and various definitions of the Strouhal number are presented Section 2.1.

Large-scale trials have been performed in a 2MW controlled test furnace at the International Flame Research Foundation, The Netherlands (Nathan *et al.*, 1992). A 50% reduction in NO_x emissions relative to an optimised air-swirled burner was measured across a wide range of excess air ratios. Suction probe measurements revealed that the reduction in NO_x emissions were associated with an increase in flame volume and a reduction in peak flame temperature of about 150°C relative to the optimised swirl flame with an equivalent throughput. Large-scale flow structures within the main body of the FPJ flame were identified through laser sheet visualisation based on the Mie scattering technique. Quantitative analysis of the visualisation images enabled determination of the mixed fluid conserved scalar field, which shows the presence of unmixed fuel and ambient fluid on the nozzle axis well downstream from the burner. Large-scale structures were clearly identified in this work and deduced to be important in the observed reduction in NO_x emissions. However, no quantitative information is available about the size of the structures, their role in the combustion process, or their relationship to the precession of the emerging jet (ie. how they are formed). This is one of the areas to be addressed in the present thesis.

Whilst the efficacy of the FPJ nozzle has been proven in practise, it produces a flow field which is extraordinarily difficult to study at the fundamental level. Primarily this is because it is "continuously unstable', and it is this very instability which appears to be the source of the efficacy. The continuous instability manifests itself in several forms, the most apparent of which is the precession of the emergent jet. As a step toward dissecting the naturally occurring precessing jet flow into its component features, a fundamental investigation of the effects of precession on a jet has been undertaken by mechanically rotating about its axis a nozzle from which an inclined, simple round jet emerges with its exit on the axis of the rotating nozzle. Unlike the FPJ, the jet which emerges from the mechanical precessing jet (MPJ) nozzle has well defined conditions at its origin that can be varied independently (Figure 1.2): viz, the exit diameter (d), velocity (u) and angle (θ), and the precessional frequency (f_p). This flexibility allows the controlled study of the separate and combined effects of these parameters.

Measurements of the cold flow mixing characteristics of a MPJ nozzle whose emergent jet is inclined at an angle of 45° from the axis of rotation (Schneider *et al.*, 1997a and 1997b) have highlighted the significance of a dimensionless *Strouhal number of precession* based on the mean exit conditions, $St_d = f_p\ d\ /\ u$. When the nozzle is rotated slowly, at a low Strouhal number ($St_d < 0.001$), the path of the jet deviates indiscernibly from the direction at which it leaves the nozzle ($\theta = 45°$) and the local jet structures resemble those in a fully pulsed jet (Bremhorst and Hollis, 1990). As the frequency is increased, strong local pressure fields are established and the jet ultimately assumes a helical path with a diameter which is an order of magnitude greater than d. In this high Strouhal number flow regime ($St_d > 0.01$), the mixing takes place on the scale of the helix diameter and the original jet completely loses its identity within some ten diameters from the nozzle exit (Schneider *et al.*, 1997b). It is considered that the Strouhal number flow regimes for the MPJ parallel those of the FPJ as the Strouhal numbers which provoke precession are the same order of magnitude in each case. Jet precession in the (MPJ nozzle) high Strouhal number regime results in an increased rate of decay of the mean velocity by an order of magnitude, relative to that in a non-precessing jet in the first 10 nozzle diameters, as indicated above. This is consistent with the increased rate at which the jet spreads, and with the finding that the Reynolds stresses are also an order of magnitude less than those in the simple turbulent jet.

Species emissions, flame shape and radiant fractions have been measured for flames of methane issuing from an unconfined MPJ (Nathan *et al.*, 1996). The different types of mixing for the MPJ associated with different regimes of St_d, correspond to quite different radiant fractions and species emissions. The low St_d flames ($St_d < 0.005$) are short and blue and the high St_d flames ($St_d > 0.015$) are broader and orange and have lower NO_x emission indices. It was found that the global features of the flames from the FPJ are closely mirrored by those from the MPJ when St_d is high. Both nozzles show an increase of about 15% in the radiant fraction and a reduction of about 25% in the NO_x emissions relative to a conventional turbulent jet diffusion flame.

To summarise the broad differences between the fluid mechanics of the precessing jet, precession of a jet causes large-scale entrainment, an order of magnitude greater than the exiting jet diameter, to occur. The jet then loses its identity within ten exit diameters from the nozzle (Schneider *et al.*, 1997a and 1997b). The existence of large-scale structures is also evident in the 2MW FPJ flame investigated at the IFRF. However the relationship between the helical motions of the exiting precessing jet and the large structures found in the FPJ flow and flame is presently unknown. With large scale mixing being a dominant feature of the precessing flow one can speculate that fine scale mixing is suppressed as the initial jet momentum has been shifted to larger flow scales, which , while they promote engulfment, do not strain the fluid sufficiently to generate the fine-scale turbulence. This postulate is yet to be fully quantified, although it is supported by frequency spectra measurements (Nathan *et al.*, 1997).

It is clear that changes in mixing due to precession are responsible for increased flame stability, reduced NO_x emissions and increased sooting tendencies. Lower in-flame temperatures have also been measured relative to a swirl flame (Nathan *et al.*, 1992) and calculated from measured changes in radiant fraction from open flames relative to turbulent jet diffusion flames (Nathan *et al.*, 1996). In particular, changes in the large-scale organisation can be expected to be important factors in the increased flame stability of precessing flames, following the arguments of Pitts (1988 and 1990). The location of the initial reaction zone and the details of the local mixing environment, in the region prior to initial combustion, could suggest the applicability of the stabilisation models for turbulent jet diffusion flames to the FPJ flame. Significant departures from the key findings of Schefer *et al.* (1994a) are not expected since both flames are diffusion flames of methane. It is considered likely that the local fine scale mixing and velocity fields provide a flammable environment which is suitable for sustained combustion.

The decrease in the NO_x emissions which result from high St_d mixing has previously been related to changes in the residence time and temperature of the gases in the flame (Nathan *et al.*, 1996). However the global residence time was calculated from time averaged flame volume and throughputs so that the accuracy of these measurements is limited. A reduction in global flame strain has also been shown to be important in prompting soot formation and hence increasing the radiant fraction (Newbold *et al.*, 1997) but a quantitative measure of differences in strain was not obtained. Both these gaps in knowledge are addressed in the present work also. Furthermore the applicability of the flamelet model requires consideration, because the decrease in NO_x emissions might also be explained by changes in the fine scale mixing resulting from precession.

Several fundamental differences exist between the flows produced by naturally occurring fluidic precession and that produced by the mechanically forced precession. The existence of a reverse flow on the centre-line of the MPJ found by Schneider *et al.* (1997b) is not found in the FPJ flow (Section 3.3). Likewise the existence of discrete vortex puffs found by

Schneider (1996) for the MPJ flow can also be questioned in the FPJ flow (Section 3.2).

The present thesis discusses two principle hypotheses. These are examined by new experimental data and by reference to existing experimental data and existing combustion models. The hypotheses are:

- *That the effect of precession of a jet is to enhance large-scale engulfment of ambient fluid and to suppress fine-scale mixing between the jet and ambient fluid streams.*

This shift in energy from fine-scale to large-scale turbulence coincides with a reduction in local strain in both the non-reacting flow and flames. It is argued that this is the fundamental difference in the mixing and is responsible for increased emissivity and reduced NO_x emissions in gas flames; and

- *That the physical mechanisms discussed here which have been proposed for simple jet flame stabilisation, other than those which include the existence of a premixed flame zone, are inappropriate for the fluidic precessing jet diffusion flame.*

That is reaction occurs in regions where the fluid has been premixed by fluid motions upstream from the flame front, to a jet concentration range which is within the flammability limits and where local velocities do not exceed the flame speed.

Assessments are also made of:

- *the validity of models developed to predict NO_x emissions from simple jet flames when applied to the fluidic precessing jet flame; and*
- *the applicability of models developed for soot formation in simple jet flames applied to soot formation in the fluidic precessing jet flame.*

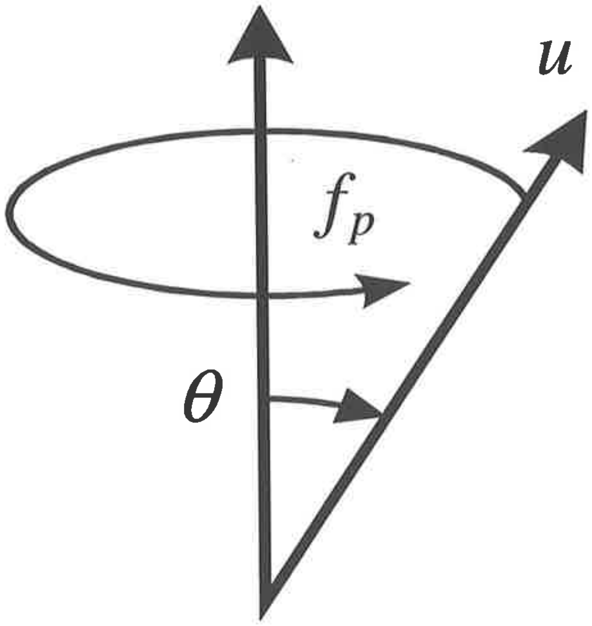

Figure 1.2 The motion of a vector inclined relative to the axis of rotation: termed "precession". Here θ is the angle between the emerging jet of velocity u, and the nozzle axis, while f_p is the precessional frequency.

1.5. Thesis Outline

Detailed descriptions of the FPJ nozzle configuration, of the flow field within it and of the experimental apparatus and techniques used in the studies are presented in Chapter 2. Three cold flow techniques are described in that chapter: flow visualisation, particle image velocimetry and mixture field measurement. Two techniques are used to investigate the reacting flows are also described: visible flame observations and laser induced fluorescence of an intermediate reaction specie to image the reaction zone.

The non-reacting mixing field produced by the FPJ nozzle is compared with that of a simple turbulent jet in Chapter 3. Results from flow visualisation and measurements of the velocity field and of the jet fluid concentration field are presented. This work supports the hypothesis that the effect of precession of a jet is to enhance large-scale engulfment of ambient fluid and to suppress fine-scale mixing between the jet and ambient streams.

Chapter 4 presents the results of experiments conducted on FPJ flames. Qualitative and quantitative data is obtained from processed images of the visible light emitted from the flame. Jet fluid concentration measurements and reaction zone imaging are also used to support the hypothesis that the FPJ flame is stabilised by the existence of a premixed zone.

Changes to flame chemistry by changes to the mixing of a jet by precession are further investigated in Chapter 5. Global trends in NO_x emissions and soot formation in precessing jet flames are compared with published empirical relations and models which have been derived to describe simple turbulent jet diffusion flames. In Chapter 6 the work is summarised and major conclusions are drawn.

Chapter 2

2. Experimental Apparatus and Techniques

2.1. Experimental Jet Nozzles

The FPJ nozzle has been described in detail by Nathan (1988) and by Nathan *et al.* (1998). It utilises a naturally occurring fluid dynamic phenomenon to produce mixing, which is of a scale much larger than the diameter of the nozzle, in the region immediately down stream from the nozzle. Precession is the term used to describe the gyroscopic like motion of a jet about an axis other than its own, as described in Section 1.5. In its simplest form the axi-symmetric fluidic nozzle consists of a cylindrical chamber with a small orifice at its inlet and a lip at its exit (Figure 2.1). The large sudden expansion at the inlet into the chamber typically has a diameter ratio of 5:1 or more (Nathan *et al.*, 1998). This results in a jet which reattaches asymmetrically to the inside wall of the chamber. As the attached jet approaches the exit lip, interaction with the lip causes it to separate and to be deflected across the nozzle axis at an angle of about 60° by a transverse pressure field in the exit plane. Within the chamber an azimuthal pressure gradient is established which causes the point of reattachment of the initial jet, and consequently of the whole flow field, to move azimuthally in a continuously unstable, quasi-periodic manner.

Hill *et al.* (1992) and Nathan *et al.* (1998) showed that this nozzle chamber configuration could produce two distinct flow modes, the asymmetric PJ mode, described above, and a more symmetric "axial jet" mode. Typically the flow is found to switch intermittently between the two modes. An optimum geometry has been identified that ensures maximum occurrence of the PJ mode (effective 100% of the time for $\mathrm{Re}_{d_1} \geq 20{,}000$) over the widest possible range of flow rates. The optimal geometry includes a centre-body within the nozzle chamber (Figure 2.2).

All nozzle configurations investigated here conform to the optimum geometric proportions found by Hill *et al.* (1992) to yield a maximum stability of the PJ flow mode. The geometric proportions of the nozzles used in the present experiments are close to the ideal geometric proportions (refer to Figure 2.2),

$$\frac{d_1}{D} = 0.20 \qquad \frac{d_2}{D} = 0.88 \qquad \frac{L}{D} = 2.75$$

$$\frac{L_c}{D} = 2.30 \qquad \frac{d_c}{D} = 0.71 \qquad \frac{w_c}{D} = 0.20$$

For all experiments performed in this thesis, flow rates are kept above a critical Reynolds number, $\mathrm{Re}_{d_1} \geq 20\,000$, based on the upstream orifice diameter, d_1, to ensure stability of the precessing flow mode. For ease of identification, the nozzles are characterised in the text by the chamber diameter, *D*.

The precessional motion for the ideal geometric configuration is characterised by a Strouhal number, St_h, (Nathan, 1988) defined as

$$St_h = \frac{f_p h}{u_{d_1}} \approx 5 \times 10^{-3},$$

values: see pg 25

where f_p is the frequency of the precessional motion, $h = (D - d_1)\,/\,2$ is the step height at the sudden expansion and u_{d_1} is the velocity at the upstream throat. Hill *et al.* (1995) have since investigated jet flows down stream from abrupt expansions in a variety of geometric configurations. They have shown that the precessional motion is better characterised by a new definition of Strouhal number,

$$St_M = \frac{f_p \sqrt{\rho} D^2}{\sqrt{M}} \approx 0.08,$$

where *M* is the momentum of the jet flow entering the chamber. The Strouhal number so defined was shown to be universal for the range of jet arrangements studied by Hill *et al.* (1995). The above equations allow the determination of the frequency of the precessional motion for the variety of cases presented in this study.

Sections 3.2 and 3.4 describe an investigation of the effect of fluid mechanical precession on the cold-flow mixing field of a jet issuing from circular cross-section orifii. The simple jet used for the comparison is the jet issuing from the identical upstream throat of the FPJ nozzle but with the chamber section and exit lip removed (Figure 2.2). To facilitate an unbiased comparison of the flows produced with, and without, the chamber attached the origin of the axes has been defined as the centre of the upstream throat. Thus the exit plane of the FPJ nozzle is located at $x = L$ ($L = 16d$). All of the nozzles investigated in this study are geometrically similar, with an axi-symmetric jet orifice at the upstream throat. The upstream throat of the FPJ has a sharp knife-edge lip, formed by a 45° bevel facing in the downstream direction. In those studies, where both the jet and the FPJ mixing fields are investigated, experimental and flow conditions have been approximately matched based on throat conditions.

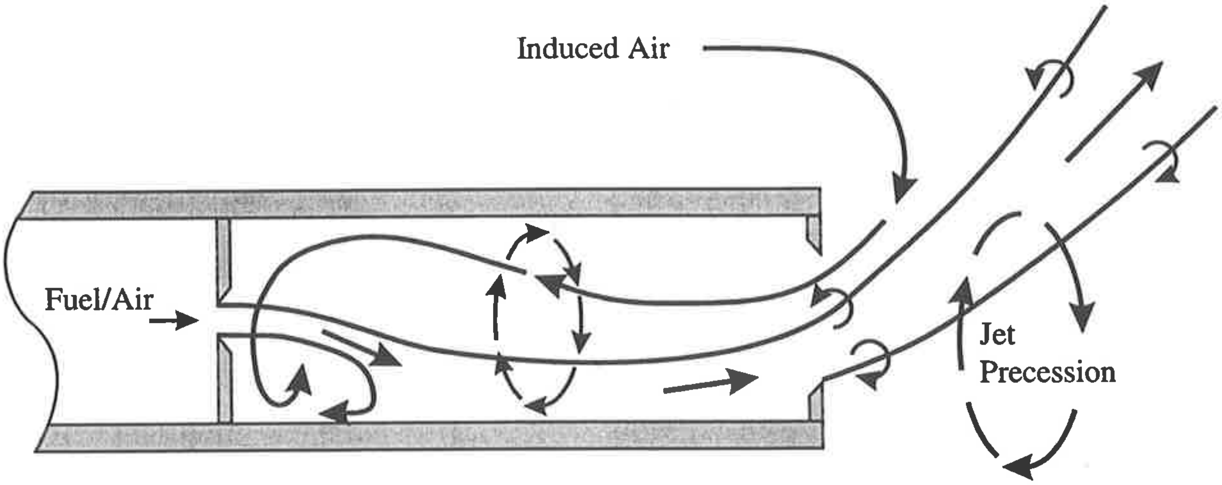

Figure 2.1 A schematic of the FPJ nozzle that illustrates the dominant features of the precessing flow field. The FPJ in its simplest form has axi-symmetric nozzle geometry consisting of a cylindrical chamber with a small orifice at its inlet and a lip at its exit. The flow field is shown with the solid lines representing a simplified description of the instantaneous streamlines and the precessing (rotating) flow, and the dashed lines indicating the azimuthal precessing motion.

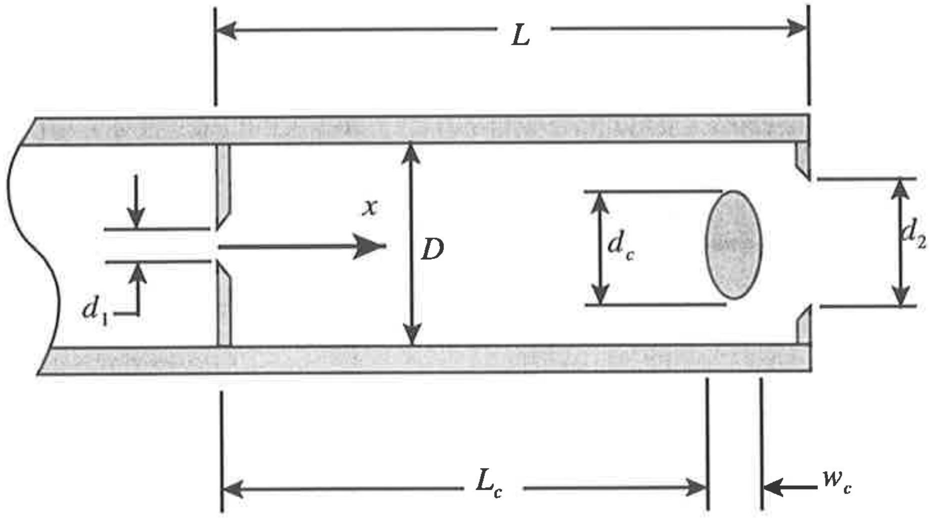

Figure 2.2 A schematic diagram of a FPJ nozzle configuration that incorporates a centre-body. The schematic shows the geometric terminology as defined by Hill (1992).

2.2. Non-Reacting Flow Techniques

2.2.1. Flow Visualisation

Planar visualisation of the flow field produced by both precessing jet and simple turbulent jet nozzles has been undertaken in a water tank facility (Newbold *et al.*, 1996). The experimental arrangement used for planar laser induced fluorescence, PLIF, studies is shown in Figure 2.3. Image sequences from digitised video frames are presented and discussed in Section 3.2.

The FPJ nozzle selected for this facility has a chamber diameter D = 44.0mm. The simple jet is produced by removing the nozzle chamber, which incorporates both the centre body and exit lip, so that the flow issues directly from the inlet orifice, d_1 = 7.3mm, into the quiescent tank.

Reynolds number similarity conditions require that the characteristic velocities in water are approximately one fifteenth of those in air because of the differences in viscosity and density between the fluids. Correspondingly, the Strouhal number relation defined above (Nathan, 1988) suggests the frequency of the precessional motion should be reduced by an order of magnitude in water relative to air. Visualisation experiments are therefore more easily performed in water where the precessional motion is sufficiently slow to be captured on standard video equipment yet still adequate temporal resolution of each precessional cycle.

Experimental Apparatus and Technique

Experiments have been performed in a perspex walled laboratory water tank facility of 750mm×750mm square section and 1500mm height. An overflow weir with a thin knife edged lip maintains a constant water level in the tank. The nozzle is suspended from an externally supported frame and is directed vertically downwards. The exit plane of the nozzle is 800mm below the surface of the water.

A planar laser induced fluorescence (PLIF) technique has been employed. The nozzle fluid is marked with a dilute solution of Rhodamine 6G and the tank fluid is initially filled with filtered water. The dilute Rhodamine solution is fed from a 200*l* supply tank, via a centrifugal pump and the flow is metered by a rotameter (Fisher and Porter 1-27-G-10 tube with GNSVT64 float) before passing out through the jet nozzle into the quiescent tank water.

A 1mm thick light sheet from a 5W Ar-ion laser (Spectra Physics), operating in multi-line mode, illuminates an axial-radial (x-r) plane passing through the centre line of the nozzle. The Rhodamine 6G solution absorbs strongly at the blue and green laser wave lengths and subsequently fluoresces in the yellow (Berlman, 1971). The fluorescent yield is linearly proportional to local dye concentration for the present experimental arrangement.

Temporal sequences of the flow visualisation images have been recorded on tape by a video camera (Panasonic WV–KS152) with zoom lens (Sony 12.5-75mm *f*/1.8). The fluid motion is effectively frozen by the short exposure times (1/1000s-1/4000s). The precessional frequency is $f_p \approx$ 1Hz, sufficiently slow for the framing rate of the camera (25 frames per second) to capture multiple images during each precessional cycle. The blue-green light scattered from air bubbles and particulate matter suspended in the water is blocked from the image by the use of a yellow, high pass, optical filter mounted in front of the camera lens. The sequences are stored on VHS (PAL) videotape.

Images have been digitised by a video frame grabber on a Macintosh 600AV computer with full frame resolution of 752×576pixels or half frame resolution of 376×288pixels and with 256 (8-bit) grey scales. The images are stored as standard Targa 2.0 grey scale graphics files.

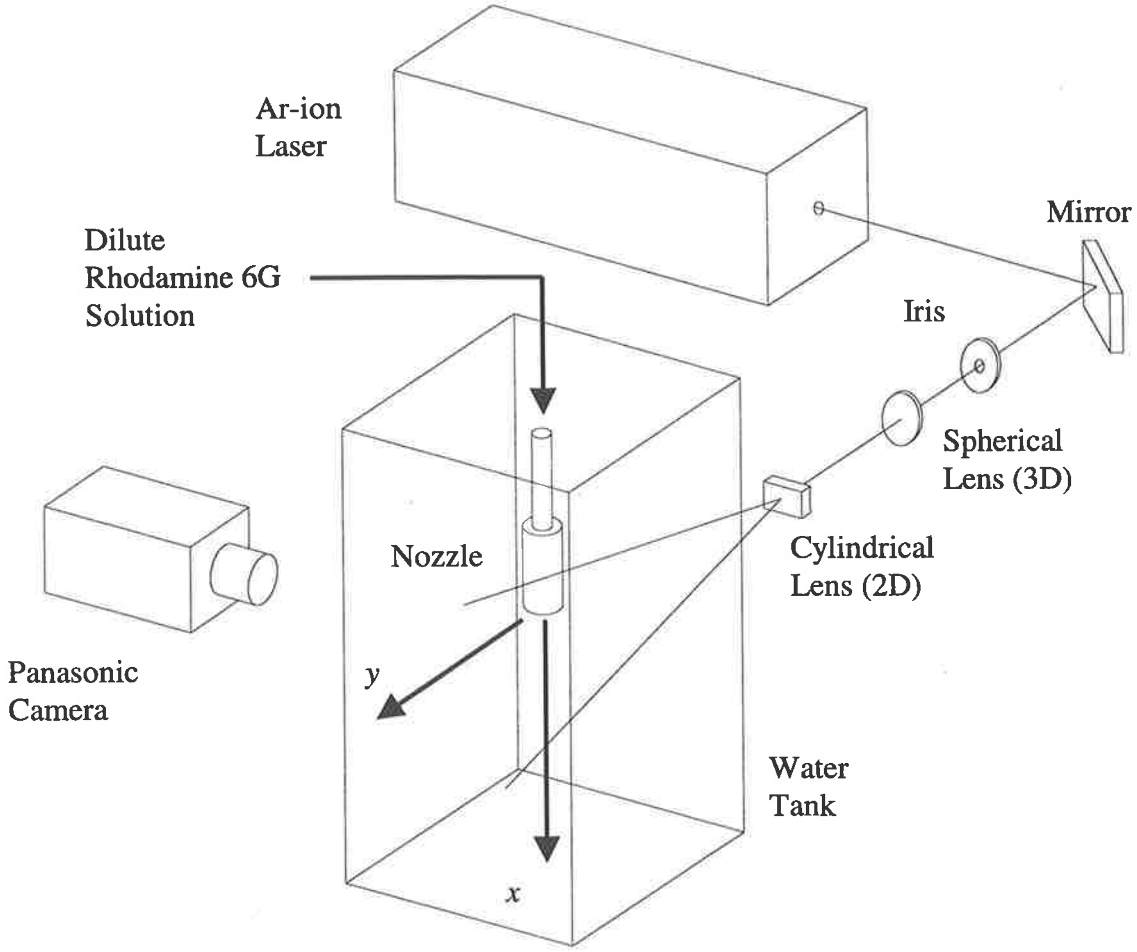

Figure 2.3 The optical experimental arrangement used for planar laser-induced fluorescence (PLIF) experiments in the water tank facility for flow visualisation.

2.2.2. Particle Image Velocimetry

Particle Image Velocimetry (PIV) has been undertaken in a water tank facility (Newbold *et al.*, 1995). The experimental arrangement is shown in Figure 2.4. PIV image and vector maps are presented in Section 3.3. Support for the hypotheses from the cold flow investigations has been principally obtained from jet concentration measurements (Section 2.2.3) so that detailed velocity measurements have not been required. Further, significant out-of-plane motions exist in this region, so that measurement using this technique is not straightforward. The purpose of the present PIV measurements is to quantify the range of typical velocities which exist in the region of flow between the nozzle exit and the flame front in the context of the large-scale motions. Detailed resolution of the wider range of vectors which exist in a given image have not been required, but the data has not been resolved to a level required to test the hypotheses

PIV is a well-developed method for determining the two-dimensional velocity field in a predominantly planar flow (Adrian, 1991). The technique yields a large number of simultaneous velocity vectors. The flow field is seeded with small tracer particles which are assumed to follow the flow faithfully. Multiple exposures of the particles mark the fluid motion at successive time instants. Interrogation of the images enables the relative particle displacements in a small image window (Δx) to be determined during a small time interval (Δt) between the successive particle exposures. The ratio ($\Delta x/\Delta t$) defines its mean velocity of the particles within the sub-window. The advantage of PIV lies in its ability to provide multiple spatial measurements simultaneously and so to visualise organised motions in a turbulent flow, despite it having relatively poor spatial resolution when compared to LDA and hot wire techniques.

Experimental Apparatus and Technique

PIV experiments have been performed with the same D = 44.0mm FPJ nozzle in the laboratory water tank facility as that described in Section 2.2.1. The water passing through the nozzle is seeded with tracer particles. The tracer particles are small polystyrene beads (0.50-1.00mm) of almost neutral buoyancy (specific gravity = 1.05). Agui and Jiménez (1987) have considered the dynamics of tracer particles, and derived equations for the degree to which particle motion is damped by drag forces. Applying the analysis to the current configuration, the tracers are estimated to have a 1.2% velocity lag when subjected to the 1Hz fluctuation typical of the present precessional frequency.

For flow visualisation the 514nm (green) beam from an Ar-ion laser is expanded by a combination of lenses into a 5mm thick light sheet passing through the nozzle axis. It illuminates the region of interest of the flow downstream from the nozzle exit. The continuous beam is chopped by an acousto-optic modulator (Isomet 1201-E) to produce a train of short light pulses. The pulse width is set at 5ms, sufficient to freeze the motion of the particles throughout the flow field. A large decay in flow velocity is evident as the flow moves through the imaged region. Hence there is no suitable pulse separation that can produce well-separated particle images for both the highest velocity region, near to the nozzle exit, and the low velocity regions at the downstream edges of the imaged region. However a pulse separation of 40ms was found to provide a good compromise.

The flow field immediately downstream from the nozzle is imaged using a CCD digital camera system (Photometrics Star-1). The system consists of a low noise slow scanning CCD camera chip, having a 576×384pixel array with 12-bit grey scale digitisation. This is well matched to the weak light intensity produced by the cw laser light source. In the present system multiple pulses are recorded on each image and an autocorrelation technique is used to analyse velocity vectors. Images are downloaded from the camera through an IEEE-GPIB interface to a 486 PC for storage and PIV image post processing. The data is stored as a non-specific binary data file type with 576×384pixel 16-bit image file format.

Image Analysis

Image analysis methodology is based on the digital crosscorrelation PIV code of Sutalo *et al.* (1993 and 1994). The purpose written PIV code used here has been written to perform an autocorrelation analysis. Each image contains many traces of multiple exposure tracer particle images. An image is divided into sets of 32×32pixel interrogation sub-windows for processing. The physical dimensions of the interrogation window are 16mm×16mm, substantially larger than the typical active length of a hot-wire or of an LDA probe volume. Ideally each sub-window should contain many traces with the same linear and angular displacements between successive particle images. A two-dimensional autocorrelation (making use of Pascal routines from Press *et al.*, 1986) is performed to determine the mean displacement of the particles in each sub-window. Increased resolution of the mean particle displacement to sub-pixel accuracy is achieved by a parabolic fit (making use of another Pascal routine from Press *et al.*, 1986) to the gaussian peak of the autocorrelation result following Willet and Gharib (1991) and Sutalo *et al.* (1993 and 1994). The displacements are used to calculate the mean velocity vectors from the pixel spatial scaling and the delay between the light pulses. The maximum determinable velocity here is u_{max} = 0.2m/s, ↕ ? set by the window size in relation to the pulse separation. The minimum velocity u_{min} = 0.28m/s is set by the spatial resolution of the camera and its capacity to distinguish the closest individual particle images.

Interrogation windows are located with 50% overlap to increase the number of vectors per image and to provide a more gradual transition between neighbouring sub-windows. In the present case an image contains 35×23pixel interrogation sub-windows. Random motions, large velocity gradients across the sub-window and out-of-plane motions produce spurious displacement results from the autocorrelation analysis. Directional ambiguity, inherent in the autocorrelation method, is resolved intuitively from the relation between neighbouring trace directions in the image. Spurious vectors are removed manually, with reference to the traces in the sub-window.

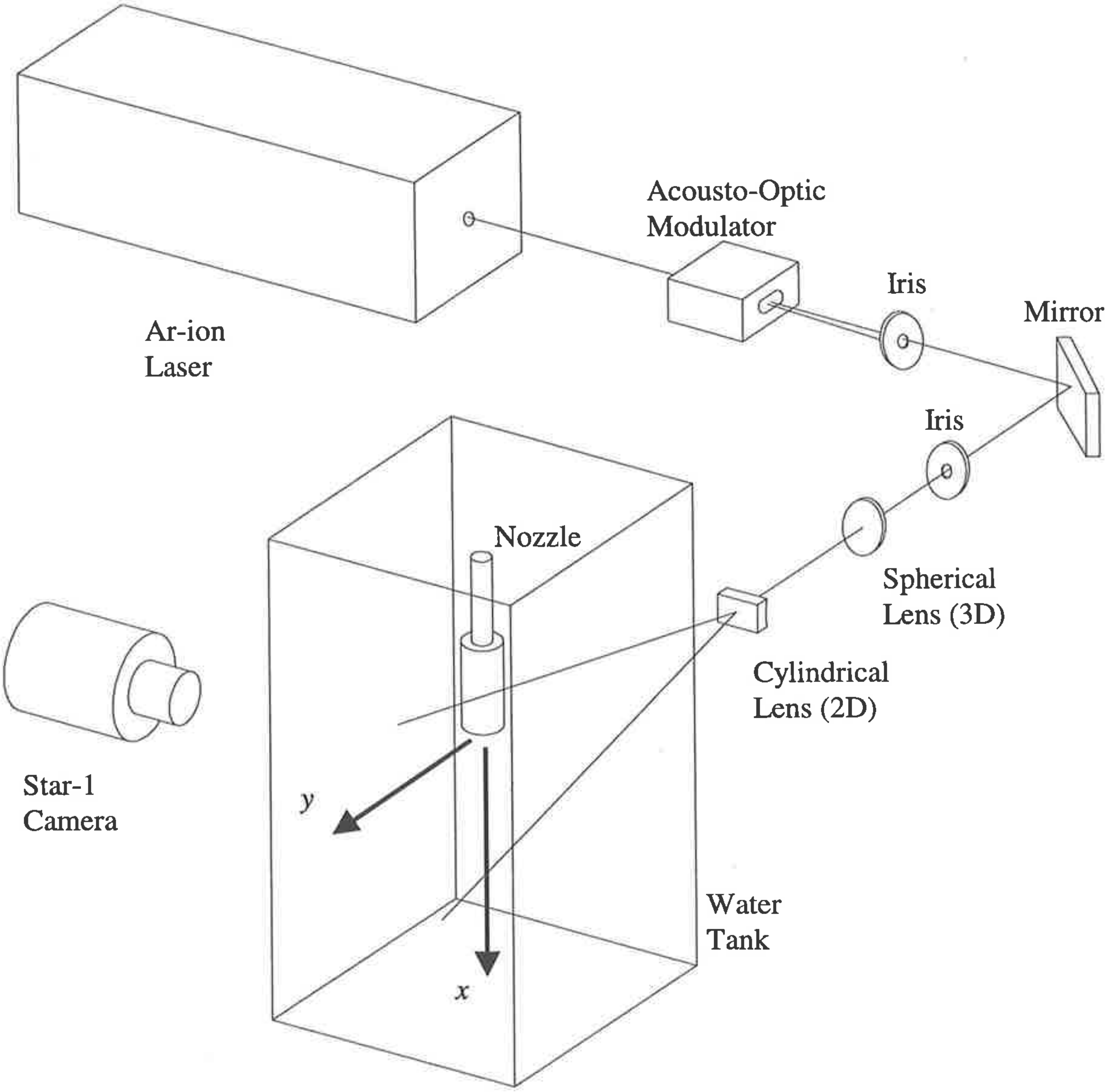

Figure 2.4 The optical experimental arrangement used to perform the particle image velocimetry (PIV) experiments in the water tank facility.

2.2.3. Planar Mie Scattering Conserved Scalar Jet Concentration Measurement

The extent of molecular mixing in a turbulent flow can be quantified by a dynamically conserved passive scalar quantity. A conserved scalar quantity is one that is advected with the fluid and diffuses relative to the fluid, but which is neither created nor destroyed within the flow and which does not directly affect the flow field (Dahm *et al.*, 1991). Quantitative measurement of the jet concentration has been achieved using the planar Mie scattering technique in air described by Nobes *et al.* (1996a, 1996b and 1997), and Nobes (1997). Planar jet concentration measurements are presented in Section 3.4 for both a simple turbulent jet flow and a FPJ flow.

Experimental Apparatus and Technique

A FPJ nozzle with $D = 13.0$mm has been used in the experiments discussed below. Data is compared with that for a simple jet issuing from an orifice of diameter $d_1 = 2.3$mm. The nozzle is supplied with air from pressure regulated plant and is metered by a rotameter (Fisher and Porter 1/2-27-G-10 tube with GUSVT410 float) with a nominal accuracy of ±2% of the full scale. The air stream is seeded with a high density of olive oil droplets nominally 0.6μm from a TSI spray atomiser placed in-line with and just upstream from the nozzle. These particles has a high Schmidt number (Sc = 38,000) so that the particles will not diffuse relative to the jet fluid stream (Becker *et al.*, 1967). The frequency response of the particles with mean diameter of 0.6μm is approximately 20kHz so that the particles will faithfully follow the turbulent velocity fluctuations of the fluid (Nobes, 1997). The nozzle is mounted on a stand approximately 1m above the laboratory floor and is vented via a 1m×1m overhead exhaust hood under which the coflow velocity is negligible.

The optical arrangement of the experiment is shown in Figure 2.5. A 250μm thick light sheet is produced by a series of lenses and aligned to pass through the centre line of the flow field in the *x-r* plane. The sheet is formed with the 532nm (green) beam from a frequency doubled Nd:Yag laser (Coherent Infinity - 40). The short laser pulse (3-5ns duration) effectively freezes the fluid motion as discussed later. A measure of the power for each laser pulse is made by directly imaging a low power portion of the laser pulse to allow correction for pulse-to-pulse variation in laser intensity.

The intensity of the light scattered from the seeding particles in an elemental volume of the flow field is assumed to be proportional to the local jet fluid concentration and incident laser power. Escoda and Long (1983) have discussed the effects of marker shot noise, bias in the scattering intensity toward larger particles and rescattering of the light sheet from out of plane particles. These effects are unavoidable and contribute to spurious fluctuations in the measured local jet fluid concentration. However they are considered to be small in the present case because the data of Nobes (1997) using the identical experimental facility, shows that the far field jet concentration statistics of a jet issuing from a smooth contraction agree well with the best available published data (Section 3.4).

The flow field is imaged through a narrow band pass filter (10nm centred on 532nm) and 50mm camera lens (Nikon *f*/1.8) by a CCD camera (Photometrics Star-1) as used in the PIV experiments in Section 2.2.2. The camera array consists of 576×384pixels, so that each image contains up to 221,184 distinct point measurements of fluid concentration. The 12-bit digitisation (4096 grey scales) of the CCD enables and a wide range of concentration scales to be resolved accurately, extending the measurements into the far field, however the slow readout which is necessary limits the frame rate to about 10 frames/minute.

The camera exposure and the laser pulse are synchronised by purpose written code (Pascal 7.0) operating on a PC. The laser pulse is triggered from a TTL pulse output via the PC parallel port. The camera is controlled via an interface (IEEE-GPIB), which opens the camera shutter to expose the CCD and subsequently transfers the image data to the PC for storage.

Each experimental run has included the collection of 600 images of the jet concentration field to ensure convergent statistics from long experimental runs. Additional images of the background and of the laser sheet profile are required for image correction.

Spatial and Temporal Resolution Considerations

A true measure of the local concentration requires that the measurement volume be small compared with the smallest concentration scales (Koochesfahani and Dimotakis, 1985 and 1986, Koochesfahani *et al.*, 1986, Dowling and Dimotakis, 1990, and Karasso and Mungal, 1996). If the sampling scales are larger than the smallest mixing scales then the small concentration fluctuations will be smoothed out and the inferred amount of mixing will be over-estimated. Koochesfahani and Dimotakis (1985) have demonstrated that degrading the temporal resolution of their measurement results in an increased probability of finding mixed fluid in the flow.

The relative importance of transportation and molecular diffusion in the mixing fluid streams is characterised by the Schmidt number,

$$Sc = \frac{\nu}{\mathrm{D}}.$$

For mixing between air streams the kinematic viscosity is the same order of magnitude as the diffusivity of the molecular species, D, and so $Sc \approx 1$. Thus scalar gradients can not be sustained across scales smaller than the smallest scale structure in the flow, the Kolmogorov scale (Monin and Yaglom, 1975). This length scale is the smallest disturbance in the velocity field on which viscosity has a dissipating effect. It is defined as

$$\lambda_k = \left(\frac{\varepsilon}{\nu^3}\right)^{-\frac{1}{4}}.$$

The smallest spatial resolution scale required to resolve fluctuations in the concentration field fully can be estimated by the Batchelor length scale (Batchelor, 1959), λ_b, defined by

$$\lambda_b = \left(\frac{\varepsilon}{\nu \mathrm{D}^2}\right)^{-\frac{1}{4}}$$

where ε is the mean energy dissipation rate. This can be reduced to

$$\lambda_b = Sc^{-\frac{1}{2}}\lambda_k.$$

If it is assumed that the Reynolds number, based on the local large-scale variables of the jet flow, is characteristic of the turbulence then ε can be estimated (Monin and Yaglom, 1975). It can be shown that

$$\lambda_k \approx \mathrm{Re}^{-3/4}\, l_x \qquad (1)$$

where l_x is the local length scale of the flow. Dowling and Dimotakis (1990) derive the above relation via an alternative route using dimensional reasoning. They include a *constant of proportionality* in the relation which they determine to be 12.5 from spectra of jet concentration measurements in a free turbulent jet.

The Kolmogorov length scale in the flow field down stream from the FPJ nozzle can be estimated by calculating the scale in a free turbulent jet whose origin is located at the axial plane corresponding to the upstream orifice of the FPJ nozzle. Experimental data show for a simple turbulent jet (Abramovich, 1963) that

$$l_x \propto x$$

as a consequence of the constant jet spreading angle in the far field, and that

$$u_{cl} \propto x^{-1}$$

with self-similarity present in the radial profiles of axial velocity in the far field. Consequently

$$\mathrm{Re}_x = \mathrm{Re}_{x=0} = const$$

and then the Kolmogorov length-scale follows a linear dependence on the axial distance from the nozzle

$$\lambda_k \propto x.$$

Calculations of λ_k using Equation (1) are presented in Figure 2.6 for the simple jet case discussed in Section 3.4. Here an air jet issues from a d = 2.3mm nozzle with Re_d = 20,000 and spreads with a constant 12° half angle, so that $l_x = 0.44x$. The magnitude of λ_k at the exit plane of the FPJ nozzle can be estimated from this calculation for the location $x = L$ ($L = 16d$). The spatial resolution of each measurement, λ_x, is 470µm×470µm and the thickness of the light sheet is $\lambda_z \approx$ 250µm. It can be seen that $\lambda_x > \lambda_k$ for $x \geq 62d$.

For the present case Sc = 38,000, so that the smallest mixing scale, the Batchelor length-scale, $\lambda_b = 0.005\lambda_k$. Consequently the smallest concentration fluctuations will be smoothed out across the measurement volume, $\lambda_x \times \lambda_y \times \lambda_z$, throughout the imaged region, $0 \leq x \leq 120d$.

The temporal resolution required to resolve to the Batchelor length-scale, λ_b, defines the Batchelor time-scale

$$\tau_b = \lambda_b / u , \tag{2}$$

This time scale is long for the FPJ flow measurements in Section 3.4 for $x \geq L$ when compared with the 5ns laser pulse duration, so that the temporal resolution is good.

Karasso and Mungal (1996) demonstrate that there is little difference in the mixed fluid distribution in a planar mixing layer (ie. the pdf was largely unchanged and consequently neither will the mean and RMS) when the experimental resolution was degraded, where the measurement volume was increased from two to three orders of magnitude greater than the Batchelor length-scale.

The measurements presented in Section 3.4 cannot be considered to be well resolved, so that some smoothing of the smallest concentration fluctuations across the measurements volume and the inferred amount of mixing will be overestimated to some extent. Nevertheless this technique has been shown to adequately resolve the fluctuations in the concentration of free turbulent jet flows by Becker *et al.* (1967) and Nobes (1997) by correctly measuring fluctuating mixed fluid statistics.

Data Reduction Technique

The marker concentration in the airstream is treated as a conserved scalar quantity. Images are processed by purpose-written Pascal code with a background subtraction to remove the noise floor, with transverse correction to account for variation in laser power variation across the sheet in the image field, with a pulse to pulse laser power correction and reduction to 10-bit quantitization. The intensity of the light scattered by the seeding particles within the measurement volume is assumed to be proportional to the local jet fluid concentration and the incident laser power. The jet concentration, ξ, is determined from the corrected local fluid concentration measurement in each pixel, c_i. The jet concentration is defined as

$$\xi = \frac{c_i - c_\infty}{c_0 - c_\infty} \quad ; \quad 0 \leq \xi \leq 1 .$$

Minimum concentration measurement (c_∞) for pure ambient fluid is measured for each image in a region which is remote from the flow field. For the simple turbulent jet measurements, the maximum concentration (c_0) of the unmixed nozzle fluid for each image can be determined unambiguously from a region in the potential core of the jet flow. Variations in the seeding density with time and the pulse to pulse laser power are therefore accounted for adequately in the image normalisation for the simple turbulent jet experiments.

The absolute values of concentration determined from the images of the PJ flow are less rigorous than are those for the simple jet. While the same corrections for the light sheet have been applied, the absence of a true potential core limits the ability to reference the concentration of pure jet fluid. Following Nathan *et al.* (1992) this local maximum, which exists adjacent to the nozzle exit, is assumed to be pure unmixed jet fluid. Strictly the reference should be taken at the origin of the jet exiting the throat at the upstream orifice of the FPJ nozzle, ie. within the nozzle chamber. Practical limitations have prevented this measurement. Recent work by Hill (1998) has shown that for the present geometric configuration the amount of ambient fluid which is drawn into the sub-atmospheric nozzle chamber is small and hence the entrainment within the chamber is comparatively small, and is extremely small with the centre-body configuration. Nevertheless a small induction of ambient fluid into the chamber can occur. Also there are high pressure gradients in the exit plane. Thus while it is likely that sufficient unmixed fluid will leave the nozzle to provide an absolute reference in many images, it is probable that the present reference for determining c_0 will result in the value being slightly overestimated in at least some of the images. While the relative values of jet concentration will be correct in each image, the absolute value may be

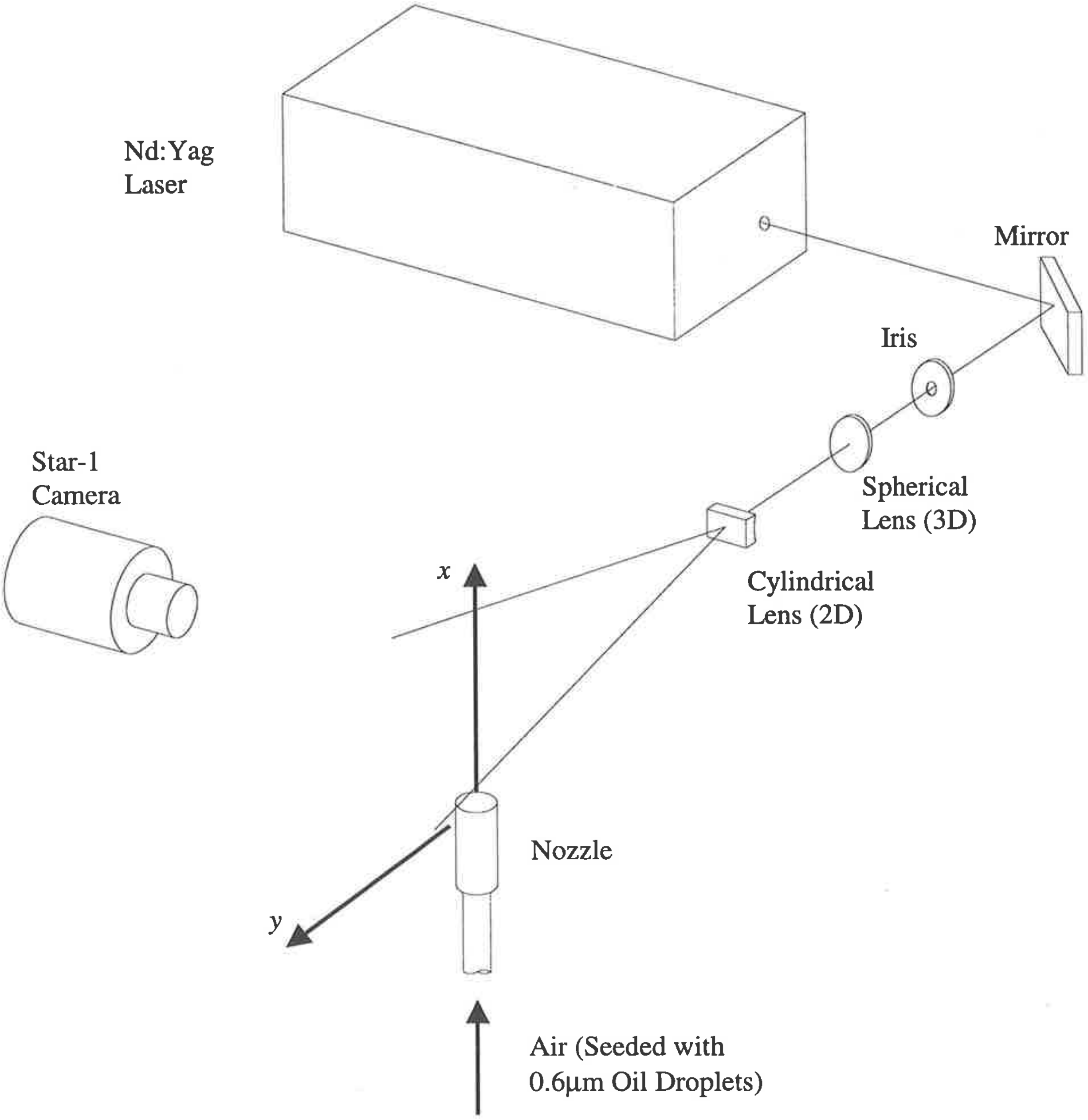

Figure 2.5 The optical experimental arrangement used to perform the planar Mie scattering experiments for jet concentration measurements, using air as the jet and ambient fluids.

slightly high.

Occasional bright spots are observed in the images due to oil spatter which scatters more light than do the aerosol particles. This is the result of oil which collects on the inner wall of the nozzle causing intermittent ejection of droplets which are significantly larger than those produced by the spray atomiser. Their effect on the statistical analysis of the mixing field is satisfactorily eliminated by the removal the two highest pixel values.

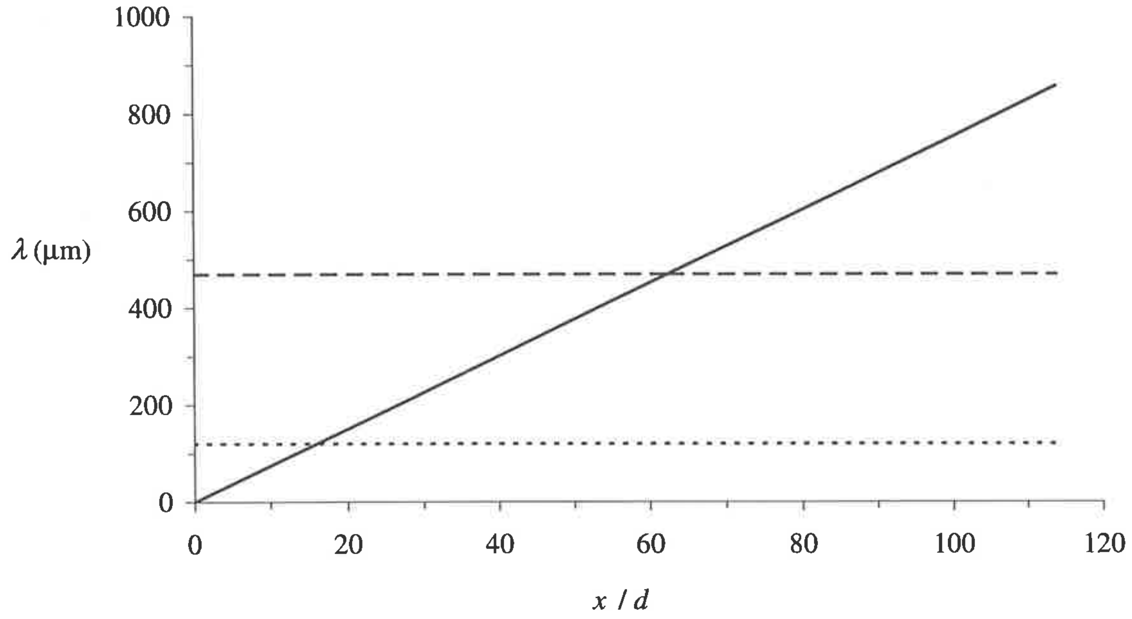

Figure 2.6 Spatial length-scales for the jet concentration measurements in the region imaged for the simple jet flow. Included are the local Kolmogorov length-scale, λ_k (——), the fixed spatial resolution of the camera, λ_x (— —), and Batchelor length-scale at the position corresponding to the FPJ nozzle exit plane, $\lambda_{x=L}$ (- - -). ($Re_d = 20{,}000$)

2.3. Reacting Flow Techniques

2.3.1. Visualisation of the visible flame envelope

Visualisation of the visible flame envelope has been performed to characterise the macroscopic mixing of an unconfined flame produced by the FPJ nozzle (Newbold *et al.*, 1993a, 1993b and 1997a). Photographs and sequences of images from cine film and digitised video are presented in Section 4.2. High speed imaging and subsequent image processing has allowed both qualitative and quantitative information to be obtained (Newbold *et al.*, 1997a).

Experimental Apparatus and Technique

Two geometrically similar nozzles have been used in the study of the flame envelope. The size of the characteristic nozzle dimension, the chamber diameter, is for each nozzle respectively $D = 13.0$mm and $D = 21.0$mm respectively.

The burner has been fired without confinement beneath an exhaust extraction hood and open flue, giving almost quiescent conditions. The nozzle was mounted vertically on a frame with the nozzle tip 700mm above the floor and directly beneath the 1.5m×1.5m hood, the lowest point of which is 3m above the floor. The rig was placed within a 3m×3m×2.5m high open enclosure of heavy duty welding curtains to reduce cross-drafts. Ample ventilation was provided by leaving a gap of 150mm between the curtains and the laboratory floor.

Liquid petroleum gas (LPG) was chosen as the fuel for this study because it gives a highly luminous flame of nearly uniform light intensity. The fuel has a nominal composition of 88% propane (C_3H_8) with the remainder being predominantly propylene (C_3H_6). It has a nominal heating value of 80MJ/m^3. For the purpose of Reynolds number calculations the viscosity has been assumed to be that of propane. The bottled fuel supply was metered through a rotameter (Fisher and Porter 1/2-27-G-10 tube with GUSVT45A float) with a nominal accuracy of ±2%

of the full scale (±3kW). The available supply pressure (300kPa) set the maximum flow rate.

Imaging Systems

A 16mm movie camera (Bolex) was used to record timed movie sequences of a FPJ flame. The maximum framing rate of 64 frames/s was used, corresponding to an exposure time of 1/120s. A zoom lens (Sony 12.5-70mm *f*/11), adjusted to capture the flame at its maximum length, was imaged using colour movie film (Ekta-chrome high-speed film).

Individual long exposure still images of a FPJ flame has been photographed using a 35mm camera with a 50mm lens (Minolta SRT-303) on to colour film (Kodak Gold II 100ASA).

A high-speed digital video (Kodak Ektapro 1000), set to record at 250 frames/s, was also used to record movie sequences for digital image processing. The time interval between successive exposures is only 80ns so that exposures are, for practical purposes, 1/250s. A zoom lens (Sony 12.5-70mm *f*/16) images on a CCD array with 239×192pixels. The array has uniform spectral sensitivity between 550nm (green) and 800nm (red), but falls off sharply to either side of this band, so that the image of a flame is dominated by the yellow-orange radiation from incandescent soot particles. Image data was stored in an 8-bit (256 greyscales) format on a multi-track FM tape drive. The video system was interfaced with a PC to enable images to be retrieved by purpose written code (Pascal 5.0) from tape storage and written to disk as standard Targa 1.0 grey scale graphics files.

Image processing of the digital image sequences has been performed to allow manipulation and interrogation of the flame images for display and analysis purposes by purpose written code (Pascal 5.0) running on a PC.

2.3.2. Reaction Zone Imaging

For visualisation of the reaction zone in the vicinity of the base of the FPJ flame, planar laser induced fluorescence (PLIF) of the hydroxyl (OH) radical has been used, following the work of Alwahabi *et al.* (1996 and 1997). Images of the reaction zone determined from OH fluorescence are presented and discussed in Section 4.3.

OH is a transient free-radical species that is an intermediary molecule in combustion chemistry and exists at high concentrations only in a region near to the flame front. Dyer and Crosley (1982) have demonstrated successfully the planar OH-LIF technique in a laminar premixed (Bunsen) flame and show that OH forms in the luminous flame zone but also extends at lower concentrations well into the burned gas region further down stream. In some cases, slow (1-5ms) three-body recombination reactions may lead to super-equilibrium concentrations of OH near the flame front of turbulent non-premixed jet flames (Seitzman *et al.*, 1990). This persistence, along with locally high mixing rates, can also allow OH to exist at lower concentrations away from the flame zone. Nevertheless the hydroxyl radical proves to be a good marker of the flame zone in non-premixed flames.

Seitzman *et al.* (1990) have imaged the reaction zone in a H_2 non-premixed jet flame where collection is at the same wavelength as excitation. This is only possible in non-sooting flames. Kychakoff *et al.* (1984) has demonstrated that scattering from particles in strongly sooting flames will appear superimposed on the OH signal and that the detection of the fluorescence emission away from the excitation wave-length is then necessary to image the OH field accurately. Versluis *et al.* (1992) show that broad band laser excitation results in interference in the collected image from the fluorescence of hydrocarbons present in the flame.

FPJ flames of propane are dominated by the presence of soot particles. Thus to avoid interference from soot scattering the measurement system employs different excitation and collection frequencies, along with appropriate choices of filters. To excite the OH radical selectively it is necessary to use a narrow band UV laser source.

Experimental Apparatus and Technique

The exhaust system in the laboratory in which the laser experiments were conducted has a maximum continuous heat capacity of 30kW. For this reason, and to minimise background flame noise, the smallest nozzle, with D = 13.0mm, has been used. The nozzle is supplied with LPG fuel from a bottled supply, and metered by a rotameter (Fisher and Porter 1/2-27-G-10 tube with GUSVT410 float), with a nominal accuracy of ±2% of the full scale. For the purpose of Reynolds number calculations the viscosity has been assumed to be that of propane. The nozzle is mounted on a stand approximately 1m above the laboratory floor and fires into the 1m×1m overhead exhaust hood with negligible coflow velocity.

The optical arrangement for the experiment is shown in Figure 2.7. The OH radicals were excited to their first electronic excited state by the output from a tunable OPPO laser (LambdaPhysic ScanMate). The OPPO laser is pumped with the "top hat" 355nm beam from a Nd:YAG laser (Coherent Infinity - 40). The OPO cavity is seeded with a narrow bandwidth laser from a dye oscillator (~0.02 cm^{-1}). This provides tunable laser radiation with good beam quality, narrow bandwidth and short laser pulses (<2nsec). The frequency of the OPO laser is doubled by a BBO crystal to a wavelength of 281.265nm. A Pellin Broca prism is then used to select the desired frequency of UV radiation. This UV beam is subsequently shaped to a 40mm high sheet (0.7mm thick).

In studying the flames, OH radicals were excited to the $A^2\Sigma$ (v=1, j=7) state. The R1(6) rotational transition was chosen because the fractional population of j=6 is less sensitive than other transitions to variation in temperature within the range 800°C-1400°C, typical of open flames. The OH fluorescence emission near 310nm only was selected by an appropriate 10nm band-pass interference filter which rejected the scattered signal from soot particles in the flame.

The OH emission was collected with an UV lens (Nikon 105mm quartz camera lens *f*/4.5) through a broadband UV filter and the narrow band pass UV filter mentioned. The lens is coupled to a gated-intensified CCD camera (Princeton Instruments, ICCD-576). The intensifier is gated to 50ns to eliminate the natural luminescence of the flame in the narrow wavelength band that is imaged. The intensifier is fibre-optically coupled to a cooled CCD array. The camera array consists of 576×384pixels with 12-bit digization on read-out. Timing of the camera, intensifier and the laser are controlled by the camera controller. Images are transferred directly form the camera through a SCSI interface board for storage by a PC.

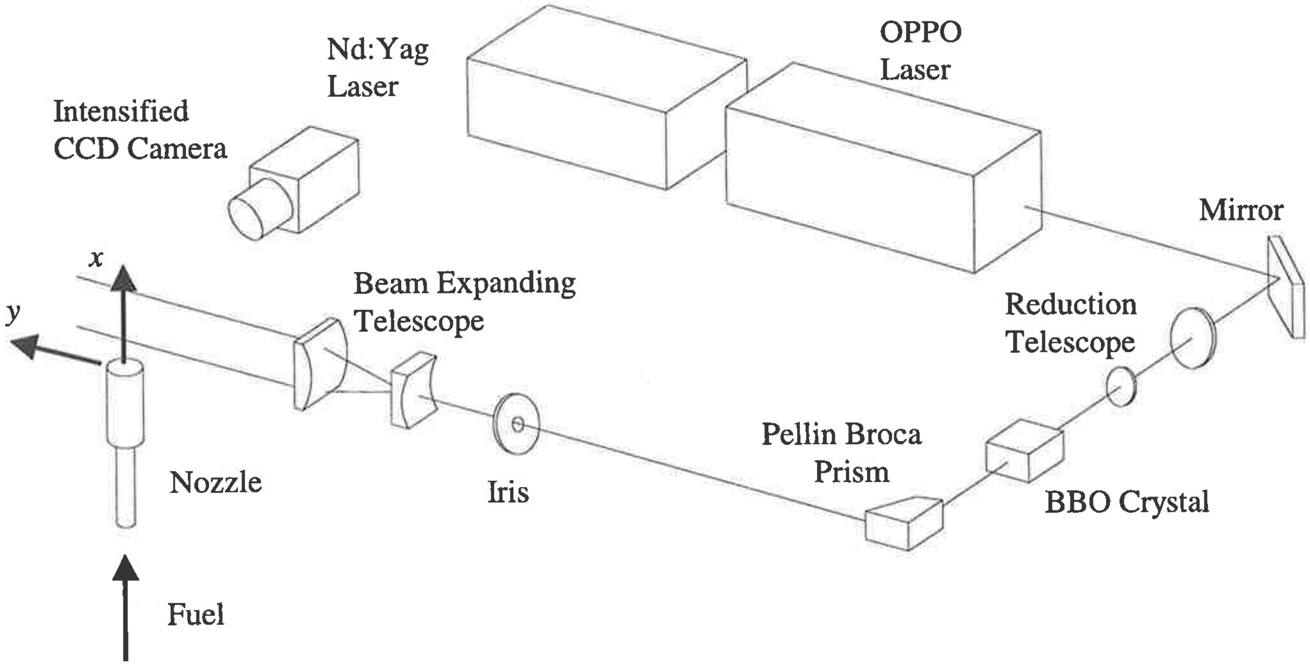

Figure 2.7 The optical experimental arrangement used to perform planar laser induced fluorescence of in-flame OH radicals for reaction zone imaging.

Chapter 3

3. Mixing in Precessing Jet Flows

3.1. Introduction

Qualitative and quantitative experimental data from investigations of the effect of precession of a simple turbulent jet flow on its mode of mixing with its surrounding ambient fluid are documented and assessed below. The simple jet is generated from a circular cross-section orifice. Precession of this jet results from a fluid mechanical instability which find practical application in the fluidic precessing jet (FPJ) nozzle, resulting from the addition of the chamber section downstream from the jet throat (Section 2.1). FPJ flows are investigated for nozzles that have geometry that maximises the reliability of precession (Hill *et al.*, 1992) and are geometrically similar to the commercial burner configuration (Rapson *et al.*, 1995). Changes to the jet mixing in non-reacting flows have been determined in the region downstream from the nozzle by flow visualisation in water (Section 2.2.1), particle image velocimetry in water (Section 2.2.2) and jet concentration measurements in air (Section 2.2.3). These techniques are used to resolve large-scale dynamic motions (Section 3.2), instantaneous velocity measurements (Section 3.3) and jet concentration statistics, macroscopic length-scales and the scalar mixing rate (Section 3.4) that characterises changes in mixing by jet precession.

3.2. Flow Visualisation

3.2.1. Experimental Arrangement

Planar flow visualisation has been performed in water to assess qualitatively the gross flow motions in the simple jet flow and the FPJ flow. By using water as the working fluid the motion of the precessing jet emerging from the nozzle chamber is sufficiently slow for it to be possible to collect multiple images during each precessional cycle at the framing rate of standard video equipment.

The particular FPJ nozzle studied is characterised by a chamber diameter $D = 44\text{mm}$. The flow field is compared with the jet issuing from the circular upstream throat of the FPJ nozzle, which is an orifice of diameter $d = 7.3\text{mm}$, but with the chamber section and exit lip removed. This choice enables an investigation of the effect of precession, which is generated solely by the addition of the chamber, on the mixing with an ambient fluid stream and its comparison with that of the simple jet. The Reynolds numbers investigated are chosen to be in the range, $\text{Re}_{d_1} > 20{,}000$, based on flow conditions at the upstream throat of the chamber. This has been chosen to be sufficiently high to ensure reliable precession (Hill *et al.*, 1992).

The flow visualisation experiments have been conducted in the water tank facility described in Section 2.2.1. The technique permits visualisation of a thin two-dimensional slice through the jet flow. A camera images a 275×210mm region of the flow that is illuminated by a light sheet passing through the jet axis. Images are recorded at 25 frames per second, corresponding to a time interval of 40ms between successive images. This framing rate is not sufficiently fast to capture dynamic events in the simple jet flow. The experiment is allowed to run for a short time (≈30s) prior to collecting images to ensure uniform dye intensity and the elimination of air bubbles from the jet stream. During the experimental run the dye accumulates in the tank so that after approximately two minutes of operation sufficient contamination of the externally recirculated tank fluid (a secondary flow pattern) occurs to cause confusion between jet and ambient fluid streams. At this point the experiment must be terminated so that the tank can be flushed and refilled.

3.2.2. Visualisation of a Simple Jet Flow

A single image of the simple jet flow issuing from an orifice of diameter $d = 7.3\text{mm}$ with mean velocity of $u_o = 5.0\,\text{m/s}$ and with $\text{Re}_d = 37{,}000$ is presented in Figure 3.1 for the region $0 \le x \le 27d$. The jet nozzle is located at the top of the image. Reflected light from the nozzle itself is eliminated by optical filtering, which permits only the frequency of the fluorescence from the dye marking the jet stream to pass to the camera. The light sheet is significantly broader than the imaged area to provide relatively uniform brightness across the image. Nevertheless the sheet is brightest in the centre of the image and the intensity falls away at the top and the bottom of the image. The brightness and contrast in the images presented are adjusted to highlight the jet flow. No correction is made for intensity variations in the light sheet so that the darkest and the lightest regions present in the images do not necessarily correspond to "pure" ambient and "pure" jet fluid respectively, but good qualitative images are obtained.

The simple jet issuing from the orifice spreads symmetrically on average, and at a narrow angle as it mixes with the quiescent ambient fluid. The jet and ambient fluid streams mix along a convoluted surface at the edge of the jet so that the instantaneous structure is not symmetric. Protrusions of jet fluid and intrusions of ambient fluid are apparent along this interface region.

A sequence of 14 cropped images of the simple jet flow is presented in Figure 3.2 for the region $0 \le x \le 27d$, of which Figure 3.1 is the first. The framing rate is insufficient for fluid to be tracked from one picture to the next and so images in this sequence are only weakly correlated and dynamic motions can not be discerned. The shutter speed is also too slow to freeze the flow completely. Nevertheless some features are clearly apparent. Structure is evident in the instantaneous jet, which appears to follow a meandering path in several images, possibly associated with an asymmetric jet mode. This is most evident at $t = 0.40\text{s}$ and

$t = 0.48$s where the jet follows a "sinusoidal" path along the jet axis. Despite the unstable nature of any instantaneous structure these images are not significantly dissimilar from each other and they do demonstrate that such sinuous motions are generally present in the flows issuing from the circular orifice.

While the present data is not qualitative in an absolute sense, it is possible to obtain some quantitative information based on normalisation along a transverse data set. Note that quantitative jet concentration measurements are presented in Section 3.4. The dye fluoresces with an intensity that is linearly proportional to the local dye concentration and the local laser power, which is constant during the duration of the experiment but varies across the sheet. The intensity of the fluorescence at a point can then be related to the local jet concentration. The average "jet concentration" field has been generated from 50 individual digitised images. No correction is made for intensity variations in the light sheet, caused by its divergence from the right to the left in the field of view. A background has been subtracted from the average and each row of the image is normalised relative to the local value on the jet centre-line. Thus the only significant assumption based in the normalisation is that the spreading of the light sheet is small, which is reasonable for the present purposes. From the limited data set it is then possible to determine the concentration half-width of the jet flow approximately, which is the width of the flow where the radial concentration is 50% of the local centre-line value. Figure 3.3 shows the 50% contour of the "normalised jet concentration". Symmetric spread of the jet is evident with a constant half-angle of 5.5°, which can be compared with the value of 6.5° obtained by more accurate measurements in Section 3.4, and with 6° obtained by Becker *et al.* (1967) as being characteristic of a simple jet flow issuing from a nozzle with a smooth contraction.

The instantaneous images of the flow can be compared with photographic images recorded by Dimotakis *et al.* (1983) that were obtained using a similar arrangement for simple jets with $500 \le \mathrm{Re}_d \le 10{,}000$. Their experimental arrangement and choice of flow conditions more adequately resolve detail present in the fine-scale concentration field. Their results show a highly convoluted jet and ambient fluid interface associated with large-scale vortical structures, so it is evident that ambient fluid is engulfed across the flow to the jet axis.

The present experimental arrangement is not able to resolve the fine-scale structure of the flow. This is a consequence of the high Schmidt number ($Sc \approx 1000$), which corresponds to a Batchelor length-scale, λ_b, and temporal scale, τ_b, that is several orders of magnitude less than the spatial and temporal resolution of the present experimental technique (Section 2.2.3). The poor spatial and temporal resolution acts to smooth the mixing field. Nevertheless, the images presented here can be compared directly with the case where the jet is precessing, which is investigated in Section 3.2.3 for the FPJ flow with a similar experimental arrangement and flow conditions.

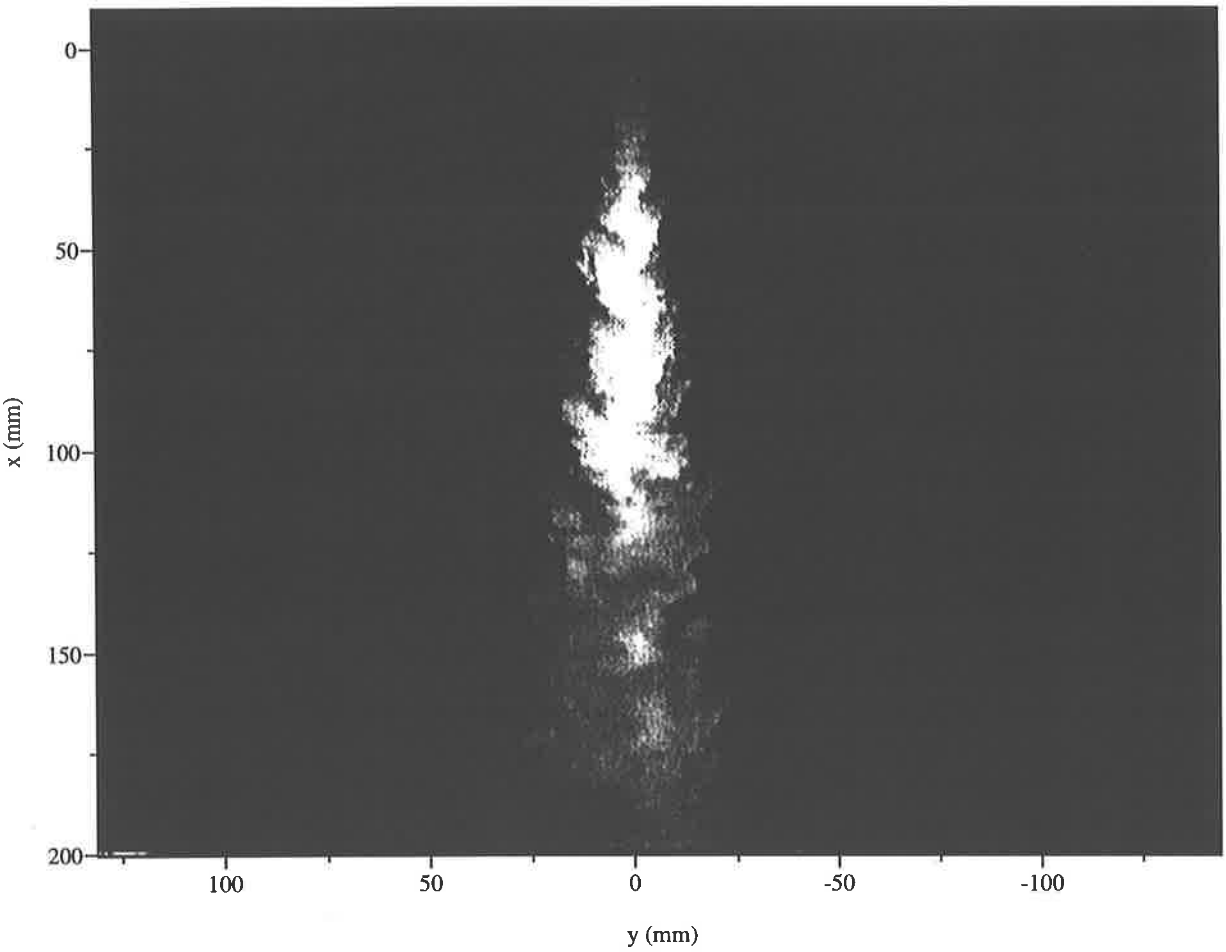

Figure 3.1 Planar flow visualisation image of the simple jet flow. The jet fluid stream is seeded with a fluorescent dye solution. The image field corresponds to the region $0 \le x \le 27d$ and $-18d \le y \le 20d$. ($d = 7.3\text{mm}$, $\text{Re}_d = 37{,}000$, Exposure = 1/2000s, Aperture = *f*/1.8, Working fluid = water)

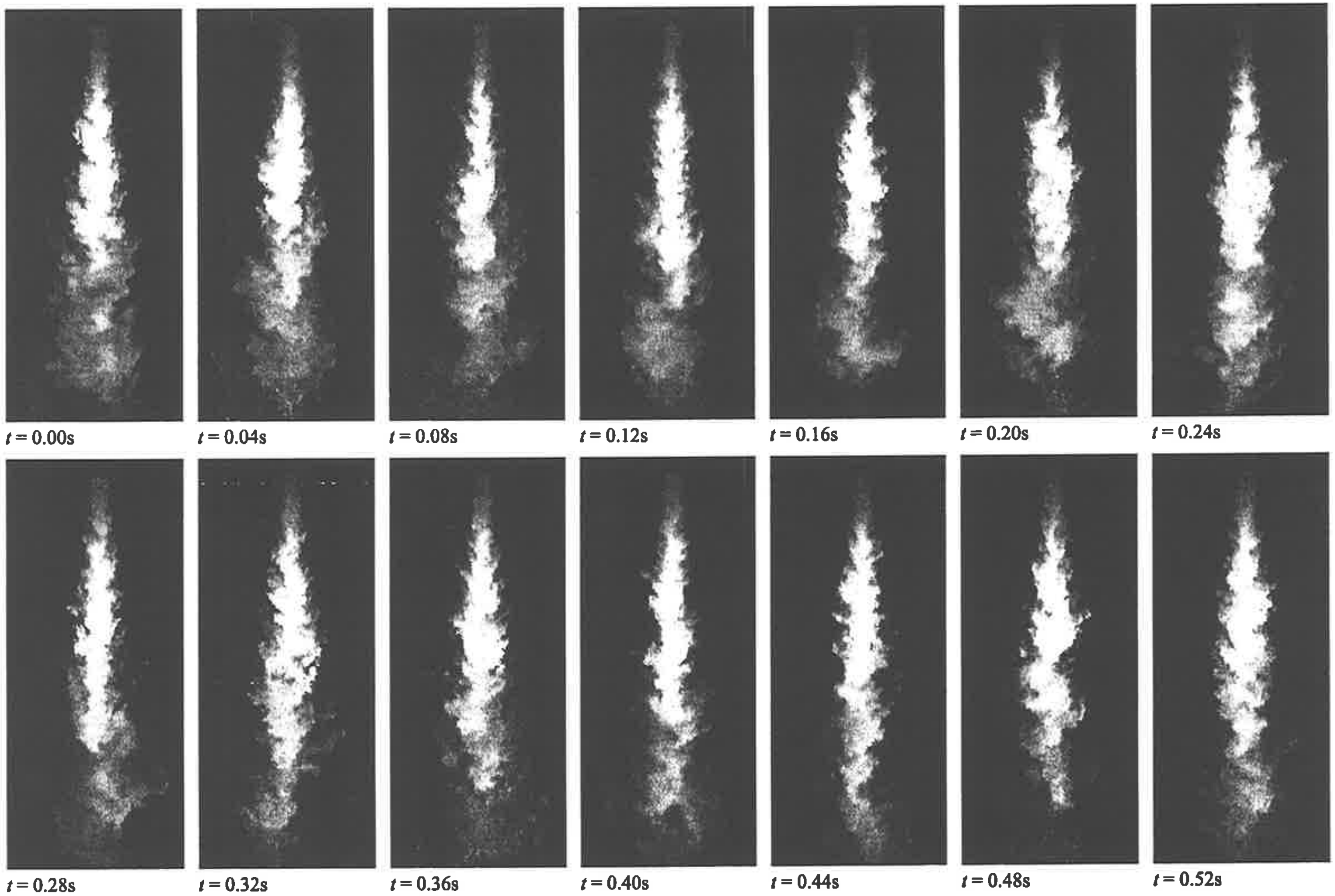

$t = 0.00$s $t = 0.04$s $t = 0.08$s $t = 0.12$s $t = 0.16$s $t = 0.20$s $t = 0.24$s

$t = 0.28$s $t = 0.32$s $t = 0.36$s $t = 0.40$s $t = 0.44$s $t = 0.48$s $t = 0.52$s

Figure 3.2 Planar flow visualisation image sequence of the simple jet flow for which Figure 3.1 is the first image. The image field corresponds to the region $0 \le x \le 27d$ and $-6d \le y \le 6d$, and the sequence spans the time period $0 \le t \le 52\text{ms}$. (Experimental arrangement as for Figure 3.1, Framing rate = 25 frames per second)

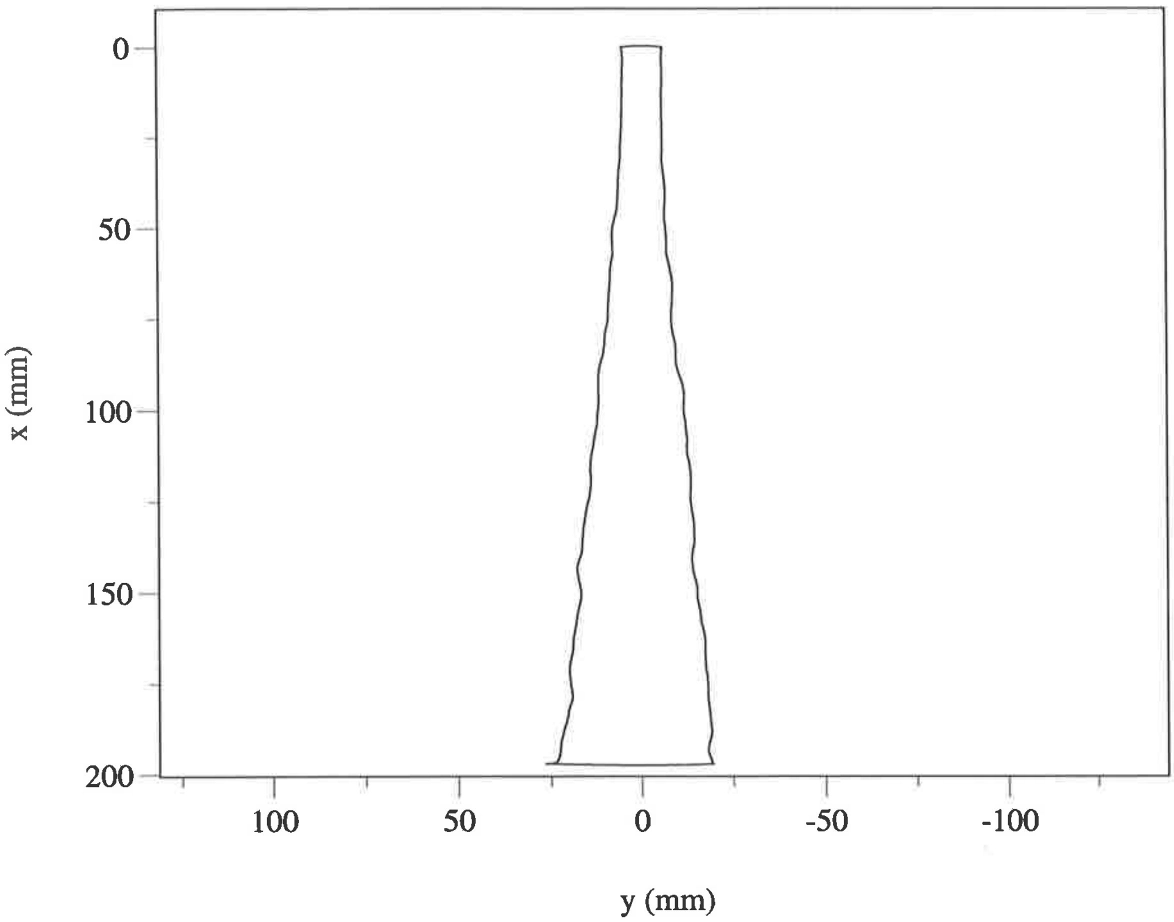

Figure 3.3 Concentration half-width contour of the simple jet flow. This data has been calculated by normalisation along each row, which assumes that the intensity variations due to divergence of the beam are negligible. (Experimental condition as for Figure 3.1)

3.2.3. Visualisation of a Precessing Jet Flow

The flow visualisation image shown in Figure 3.4 illustrates the FPJ operating at $\mathrm{Re}_{d_1} = 37{,}000$. The field of view is $0 \le (x - L) \le 27d_1$. This image is directly comparable to the image presented in Figure 3.1 for the simple jet, since both were obtained with the same experimental arrangement and flow conditions. The length of the chamber section is $L \approx 16d_1$, so that $0 \le (x - L) \le 11d_1$ here is overlapped by $16d \le x \le 27d$ in Figure 3.1. The FPJ nozzle tip is visible at the top of the image because the jet fluid within the perspex nozzle chamber fluoresces.

In contrast to the images of the simple jet this image of the FPJ flow shows a much more highly convoluted interface between the jet and ambient fluid streams extending far downstream. The images presented here represent a two-dimensional slice through a complex three-dimensional flow field. Sharp concentration gradients exist near to the nozzle between islands of jet fluid and ambient, or near ambient fluid. It is evident that the slice illuminated by the light sheet cuts through the emerging jet as it is deflected sharply away from the jet axis at that instant.

A sequence of 15 cropped images of the FPJ flow is presented in Figure 3.5 of which Figure 3.4 is the first. This sequence spans $0 \le t \le 0.56s$ for the region $0 \le (x - L) \le 17d_1$. This figure shows approximately one full precessional cycle. A calculation based on the St_h relation of Section 2.1 shows that the precessional motion has a characteristic frequency of $f_p \approx 1.4\mathrm{Hz}$. Hill (1998) has demonstrated the validity of this Strouhal number relation for nozzles with the current geometric proportions. The mean duration of a precessional cycle is then predicted to be 0.70s, which is consistent with the present sequence.

The series illustrates the gross flow motions in a typical cycle of jet precession. At $t = 0\mathrm{s}$ the instantaneous emerging jet is directed out of the imaging plane. For $0.04 < t < 0.16\mathrm{s}$ the emerging jet is directed to the right side at an angle of approximately 45° to the jet axis. At

$0.20 < t < 0.32\text{s}$ the jet is again directed out of the imaging plane as it leaves the nozzle, and during $0.32 < t < 0.48\text{s}$ the jet is directed to the left. As the visualisation does not capture the out-of-plane motion of the jet, the imaging technique represents the precession as a side-to-side (flip-flop) motion.

It is important to note that large dark pockets in the flow demonstrate that there is considerable ambient fluid, or near-ambient fluid, drawn to the jet axis close to the exit of the FPJ nozzle. This "ambient" fluid is entrained deeply into the flow by large-scale motions. Attention is directed to a typical puff structure at $t = 0.20\text{s}$ in Figure 3.5. This structure is of a scale larger than the emerging jet and is apparent for a considerable time span, $0.20 \le t \le 0.40\text{s}$, during which the ambient fluid maintains a good contrast with the mixed fluid present in the structure. The mixing process appears to be dominated by the engulfment of ambient fluid. This can be seen more clearly in the far field of the image where fluid near the ambient concentration is still present.

A second sequence of 15 cropped images spanning $0 \le t \le 0.56s$ is presented for the FPJ with $\text{Re}_{d_1} = 61{,}500$ in Figure 3.6 for the region $0 \le (x - L) \le 25d_1$. The sequence spans slightly greater than one full precessional cycle, which is consistent with a characteristic precession frequency of $f_p \approx 2.3\text{Hz}$ at this throughput determined from a calculation that is again based on St_h.

This sequence is notable due to the presence of a roller structure indicated at $t = 0.24\text{s}$. Relatively small changes in both the position and shape of this flow feature are observed from one image to the next for $0.24 \le t \le 0.48\text{s}$ and low axial/radial velocities can be inferred. The presence of larger structures with low velocity suggests that the flow is characterised by a lower bulk mean strain rate than with the simple jet. Lower strain rate is also consistent with the observation that unmixed ambient fluid persists much further down-stream than occurs in a simple jet, presumably due to the lower intensity of the fine-scale mixing.

Figure 3.7 shows the 50% contour of the normalised jet concentration for three cases of the FPJ flow with $\text{Re}_{d_1} = 37{,}000$, $\text{Re}_{d_1} = 49{,}000$ and $\text{Re}_{d_1} = 61{,}500$. These contours have been determined following the same image processing scheme used in Section 3.2.2 to determine the approximate concentration half-width of the simple jet flow. Again, no correction is made for intensity variations in the light sheet. These contours show that the mean flow is similar for each case and that the spreading half-angle of the FPJ flow is typically 45°. It is apparent that the small data sets do not produce smooth averages, so that the contours only show the broad difference in spread angle of the FPJ flow cases. The slightly different spread in the three flows suggests that the Reynolds number only has a weak effect on the spreading angle of the FPJ flow.

Fundamental differences in the characteristics of the turbulent structure of the FPJ flow and the simple jet are also evident by viewing the "fossil" turbulence at the conclusion of an experimental run. Since the water tank is closed (other than at the overflow weir), the turbulence energy dissipates very quickly after the flow to the jet nozzle is switched off, and within a minute or so diffusion processes tend to dominate. Any structure in the fluid which can be seen after this point, is referred to here as fossil turbulence. There is no structure evident in the fossil turbulence generated by the simple jet. The fluid is well mixed and of a roughly uniform concentration. By contrast the fossil turbulence left by the FPJ flow is non-uniform and structure is clearly evident in it. Its appearance is of fluid "layers" of different concentrations which are "folded". This is further evidence that the scale at which the energy of turbulence is concentrated is shifted away from the finer scales evident in the simple jet into the larger scales which dominate the precessing jet.

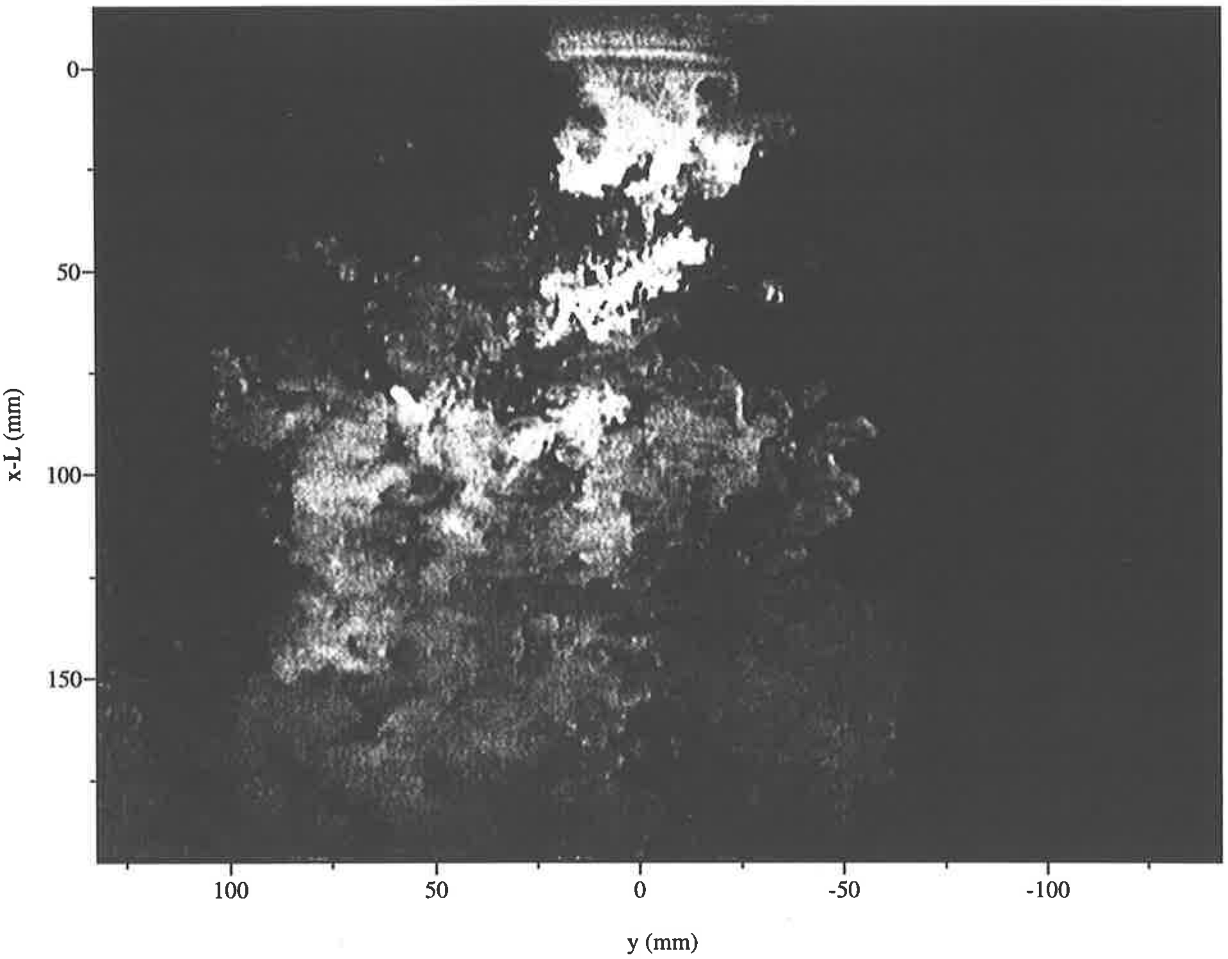

Figure 3.4 Planar flow visualisation image of the FPJ flow. The image field corresponds to the region $0 \leq (x-L) \leq 27d_1$ and $-18d_1 \leq y \leq 20d_1$. ($d_1 = 7.3\text{mm}$, $D = 44\text{mm}$, $\text{Re}_{d_1} = 37{,}000$, Exposure = 1/2000s, Aperture = *f*/1.8)

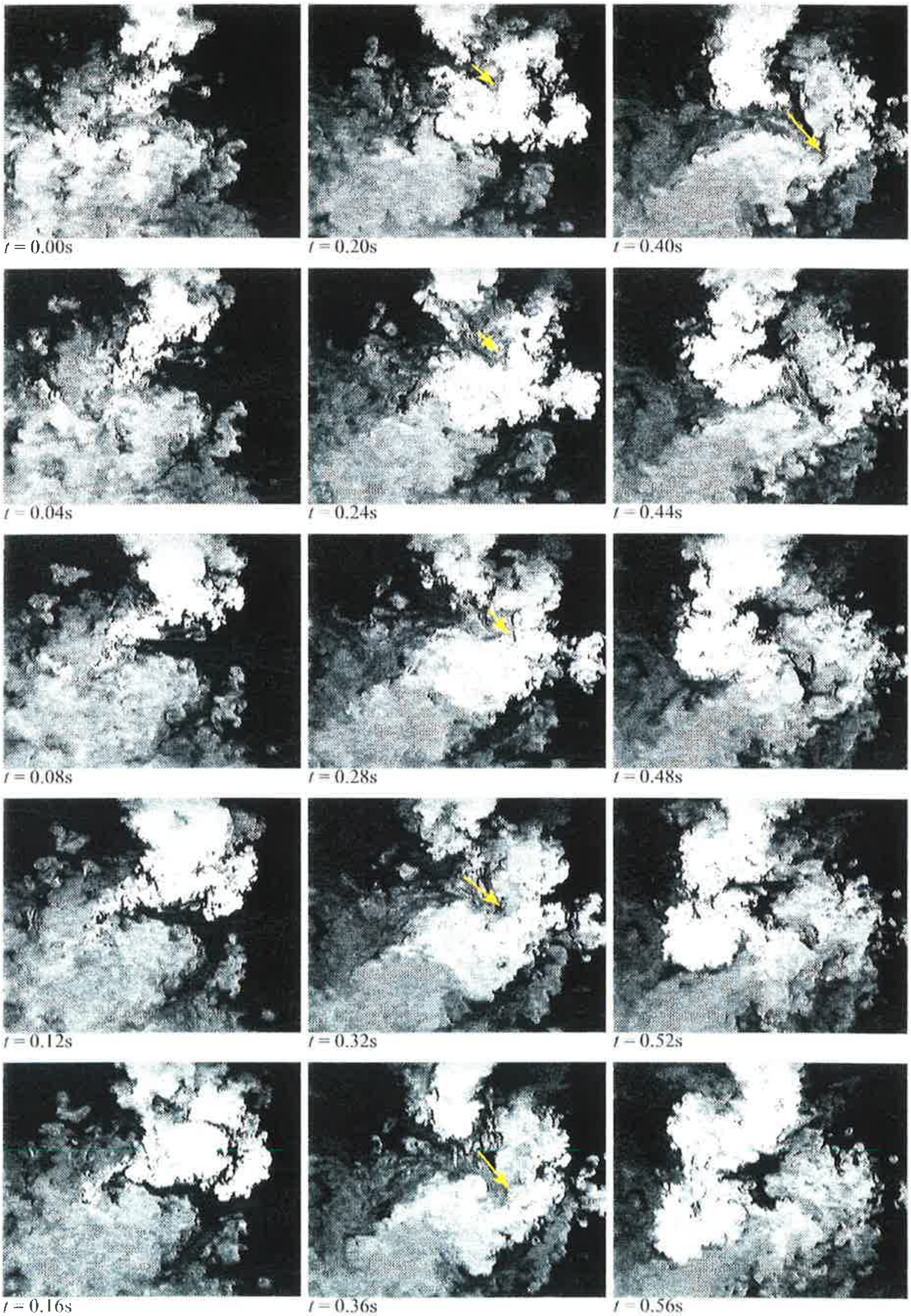

$t = 0.00$s $t = 0.20$s $t = 0.40$s

$t = 0.04$s $t = 0.24$s $t = 0.44$s

$t = 0.08$s $t = 0.28$s $t = 0.48$s

$t = 0.12$s $t = 0.32$s $t = 0.52$s

$t = 0.16$s $t = 0.36$s $t = 0.56$s

Figure 3.5 Planar flow visualisation image sequence of the FPJ flow for which Figure 3.4 is the first image. The image field corresponds to the region $0 \le (x - L) \le 20d_1$ and $-12.5d_1 \le y \le 12.5d_1$, and the sequence spans the time period $0 \le t \le 56\text{ms}$. (Experimental arrangement as for Figure 3.3, Framing rate = 25 frames per second)

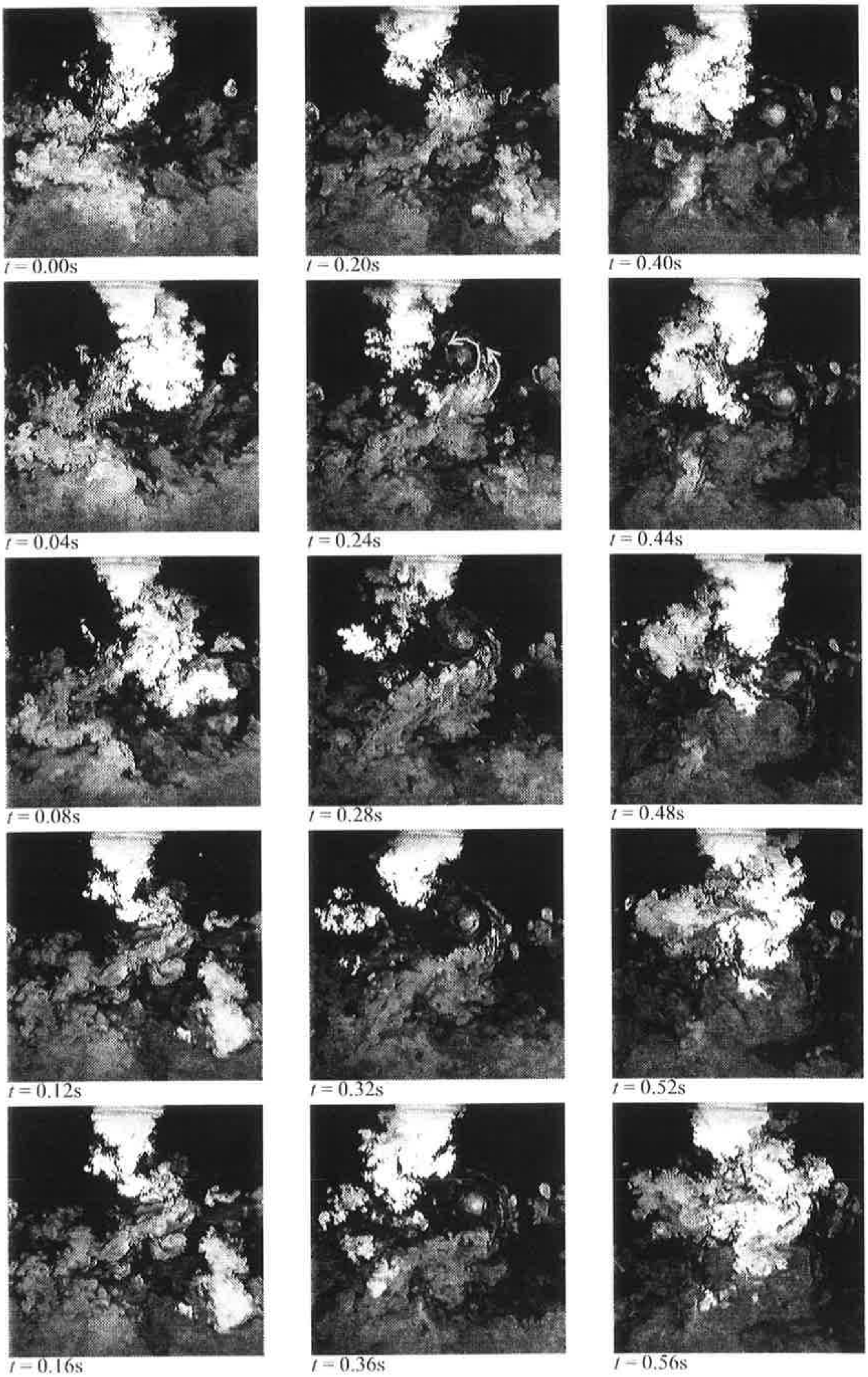

$t = 0.00$s

$t = 0.04$s

$t = 0.08$s

$t = 0.12$s

$t = 0.16$s

$t = 0.20$s

$t = 0.24$s

$t = 0.28$s

$t = 0.32$s

$t = 0.36$s

$t = 0.40$s

$t = 0.44$s

$t = 0.48$s

$t = 0.52$s

$t = 0.56$s

Figure 3.6 Planar flow visualisation image sequence of the FPJ flow. The image field corresponds to the region $0 \le (x - L) \le 25d_1$ and $-12.5d_1 \le y \le 12.5d_1$, and the sequence spans the time period $0 \le t \le 56$ms. ($d_1 = 7.3$mm, $D = 44$mm, $\mathrm{Re}_{d_1} = 61{,}500$, Framing rate = 25 frame per second, Exposure = 1/2000s; Aperture = $f/1.8$;)

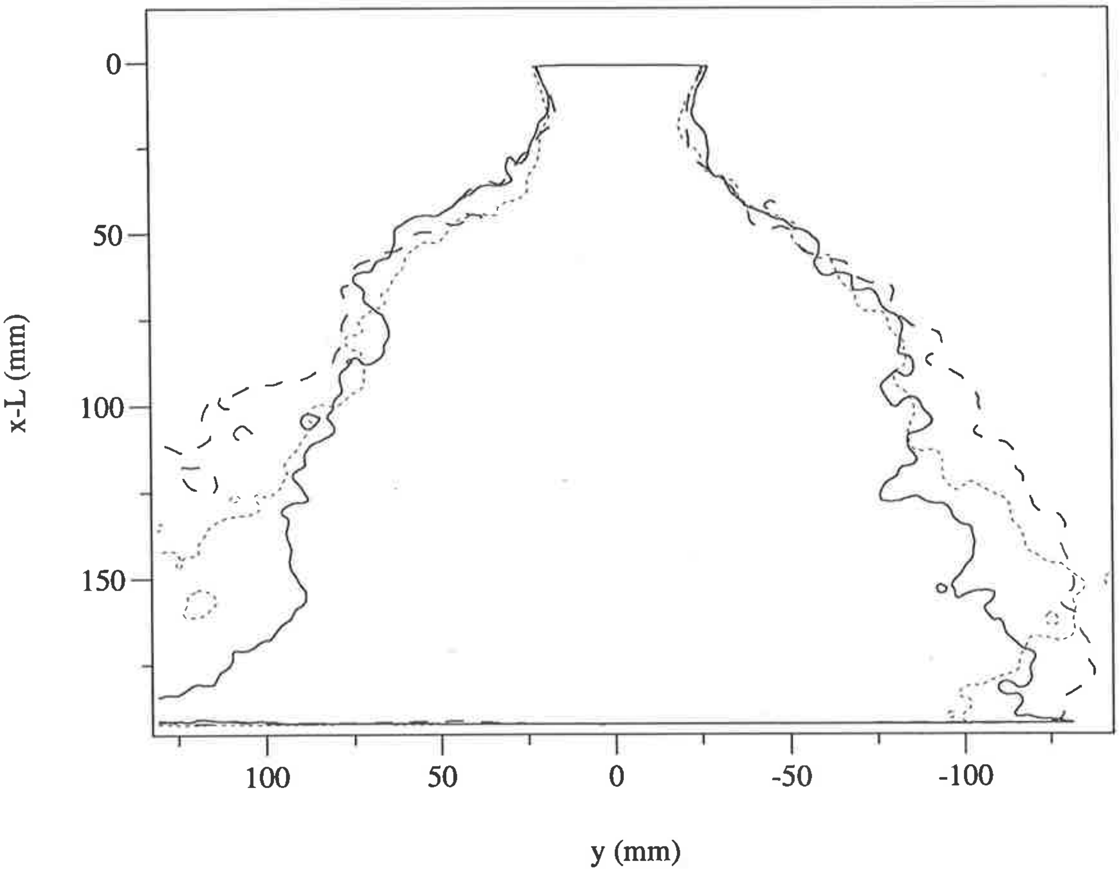

Figure 3.7 Concentration half-width contour for the FPJ flows. (Experimental conditions as for Figure 3.4, —— $\mathrm{Re}_{d_1} = 37{,}000$, – – $\mathrm{Re}_{d_1} = 49{,}200$ and - - $\mathrm{Re}_{d_1} = 61{,}500$)

3.3. Velocity Measurements in a Precessing Jet Flow

3.3.1. Experimental Arrangement

Velocity measurements have been performed in flow generated by the FPJ nozzle to assess the broad features of the velocity field associated with the large-scale motions illustrated in Section 3.2 and to visualise bulk flow motions. Full resolution of the wide range of velocity vectors present in the flow at any instant is not attempted. The measurements reported here relate to the FPJ nozzle of diameter D = 44mm and only one set of flow conditions which were similar to those used in the flow visualisation shown in Figure 3.3. The mean velocity through the upstream orifice, of diameter d_1 = 7.3mm, is $u_{d_1} = 5.0\,\mathrm{m/s}$ and the Reynolds number is $\mathrm{Re}_{d_1} = 37{,}000$.

Velocity measurements have been conducted using the particle image velocimetry (PIV) technique in water as described in Section 2.2.2. The technique permits planar velocity measurements in a 5mm thick slice through the flow, when the dominant velocity component is planar. The camera images a 325×215mm region of the flow, $0 \leq (x - L) \leq 29d_1$. Illumination is provided by a cw laser whose beam is chopped to provide a double pulsed light sheet passing through the jet axis, with a time interval of 40ms between successive pulses. The facility is allowed to run for about 30s prior to image collection to eliminate unsteady effects introduced by non-uniform particle seeding and air bubbles in the supply lines.

3.3.2. Velocity Measurements in a Precessing Jet Flow

Two representative unprocessed images of the FPJ flow seeded with particles and exposed with the double pulsed laser sheet are shown Figures 3.8. These images were recorded with the nozzle directed vertically downward into the tank. The emerging jet at the nozzle exit, directed to the left and right in Figure 3.8(a) and (b) respectively, is visible in the two images. The exit angle of the jet relative to the nozzle axis is about 45° - 60° in each case, broadly consistent with the visualisation study shown in Section 3.2.3. The abrupt change in the magnitude and direction of the particles at $(x - L) \approx 50$mm~~mm~~ indicates that the emerging jet moves out of the illuminated plane along a helical type of path which is not immediately evident from the flow visualisation.

The rate of spread of the jet fluid decreases with down-stream distance so that in practice most of the particle traces are contained within a 45° half-angle cone. The jet fluid is seeded with a very high particle concentration to produce a sufficient particle density to allow PIV analysis in the regions downstream. Near to the nozzle exit the 5ms light pulse duration is not short enough to truly "freeze" the motion of all the tracer particles in the exiting jet. Good particle trains are produced at locations quite close to the nozzle, demonstrating a reasonable choice of pulse spacing. Note that this implies a dramatic reduction in the magnitude of the exit velocity relative to that at the jet throat, since the distance that a particle moving at the throat velocity would travel in this time interval is $\Delta x = u_0 \Delta t = 200$mm.

Considerable reduction in particle concentration with distance from the nozzle is evident as the flow spreads and unseeded ambient fluid is entrained. Particles in regions of lowest velocity have not moved sufficiently between illumination pulses to produce distinct particle image traces. Hence the data set is not able to resolve the entire range of velocities present in the imaged region. Nevertheless there is sufficient data to quantify broad features of the flow, with sufficient resolution to address the hypothesis of this work.

In Figure 3.9(a) the instantaneous direction of the emerging jet is out of the illumination plane and slightly to the right. Clusters of higher particle density downstream from the nozzle and to the left of the jet axis (x = 50mm, y = -50mm) mark the reappearance of the jet in the illumination plane. Particles are fairly evenly distributed throughout the flow field, with the distribution of particle concentrations better suited for PIV processing than that in Figure 3.8.

The image in Figure 3.9(a) has been processed using autocorrelation PIV, as described in Section 2.2.2 and the resulting vectors are presented in Figure 3.9(b). There are a significant number of locations at which the PIV analysis fails to produce a good velocity vector. Generally this can be attributed to a low number of particles in the interrogation window, the low velocities present at these locations, or the high out-of-plane velocity component especially near to the nozzle. Nevertheless the analysis demonstrates that within the region close to the nozzle the magnitude of the velocity has decayed by two orders of magnitude from that of the jet throat. This would correspond to the flame stabilisation region in a reacting flow.

A notable feature of the flow imaged in Figure 3.9 is the existence of a well-defined eddy-like motion on the right edge of the image at (x = 100mm, y = 150mm). This structure might be similar to the structure that was identified in the flow visualisation in Figure 3.5. It is apparent that it induces a flow toward the jet axis along the upstream side of the eddy. This would appear to be ambient fluid being engulfed by the jet flow.

Nearly all the vectors determined by the PIV technique in Figure 3.9(b) are directed generally downstream (downward) but have a small but significant radial velocity component. Whilst the velocity vectors show random motions, a dominant axial motion is evident throughout the imaged region. Schneider *et al.* (1997a and 1997b) conducted velocity measurements by laser doppler velocimetry in the near nozzle region of cold precessing jet flows from a mechanical precessing jet (MPJ) nozzle. These measurements have shown that jet precession results in an initial spreading with half-angles of about 45°, in the generation of coherent motions over the entire scale of the motion transcribed by the precessing jet, and in an initial decay of mean jet velocity which is an order of magnitude greater than that in a simple jet. The initial region of the MPJ flow can be related to the FPJ flow by relating the exit diameter of the MPJ nozzle to the jet emerging from the FPJ nozzle by using the notion of an equivalent exit diameter (Nathan, 1988, and Nathan and Luxton, 1991c). This also allows the jet exit velocity to be estimated. The equivalent exit diameter is based on the velocity half-width of the simple free jet, calculated at the axial location corresponding to the exit plane of the FPJ nozzle. The equivalent exit diameter of the D = 44mm FPJ nozzle is then about d = 23mm so the equivalent bulk mean exit velocity is $u_0 \approx 0.5$m/s. While the exit velocity is not well resolved by the PIV technique, the estimates are broadly consistent with the measurements. Further rapid decay in vector magnitudes immediately downstream occurs with the FPJ flow as with the MPJ flow. Although there is directional ambiguity in an autocorrelation PIV technique, the present technique minimises the ambiguity by considering the direction of nearby vectors. No trends in the present data suggest any reverse flow along the geometric jet axis. This is markedly different from the measurements in the MPJ flow (Schneider *et al.*, 1997b) where a substantial reverse flow region was measured.

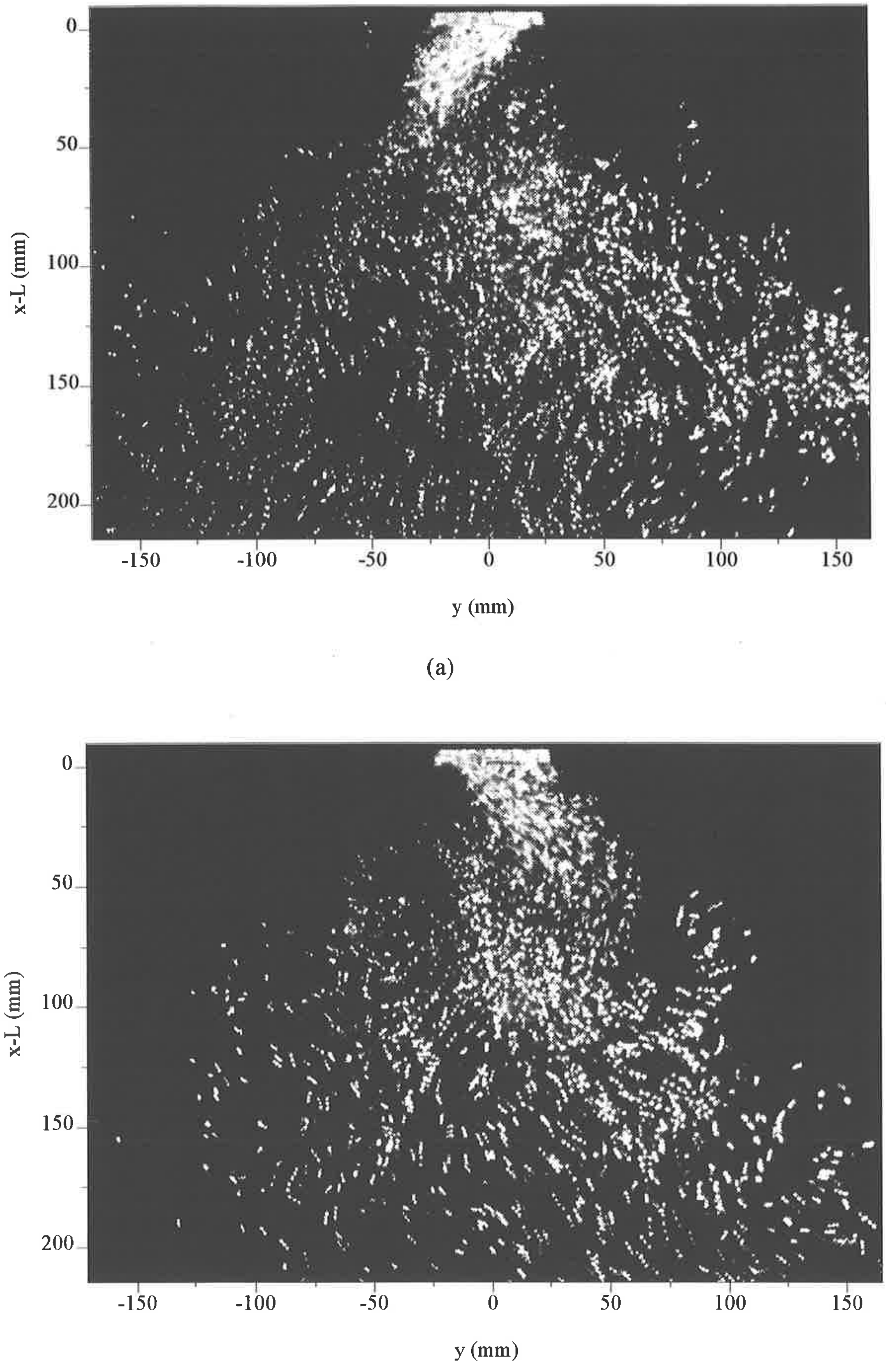

(a)

(b)

Figure 3.8 Raw images of the FPJ flow generated by a pulsed laser sheet used for the PIV measurements. (Experimental conditions as for Figure 3.3; Pulse duration = 5ms; Pulse spacing = 40ms; Aperture = *f*/1.8)

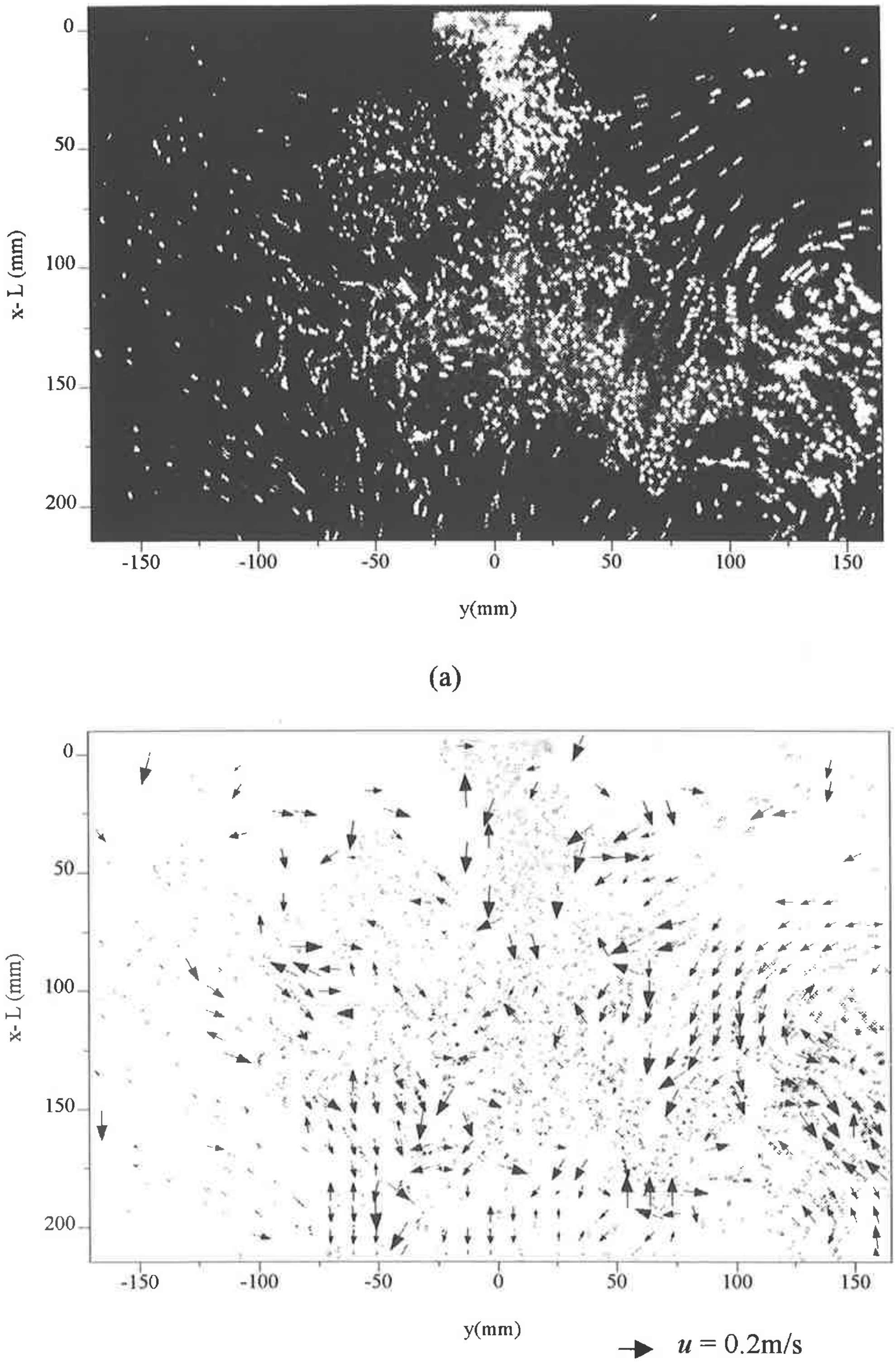

(a)

(b)

Figure 3.9 (a) Raw image of the FPJ flow generated by a double pulse laser sheet and (b) the vector map produced from the correlation analysis. (Experimental conditions as for Figure 3.3; Pulse duration = 5ms; Pulse spacing = 40ms; Aperture = *f*/1.8)

3.4. Scalar Mixing Field of a Precessing Jet Flow

3.4.1. Experimental Arrangement

In this section a detailed statistical comparison is made between the scalar mixing field of the simple jet flow and that from the FPJ flow by means of planar jet concentration measurements. The comparison is based on the determination of instantaneous, mean and fluctuating jet concentration fields, the intermittency, mixed fluid distributions, the macroscopic mixing length-scale and the scalar mixing rate.

The flow generated by the D = 13mm FPJ nozzle is compared with the simple turbulent jet flow issuing from an orifice of diameter d = 2.3mm. The simple jet can be configured to issue from the circular upstream throat of the FPJ nozzle be removing the chamber section of the FPJ nozzle. The experimental and flow conditions have been approximately matched based on the jet throat conditions, with a Reynolds number of $\mathrm{Re}_{d_1} = 20{,}500$ for the FPJ flow, based on the upstream throat variables, and Re_d = 22,300 for the simple jet flow. This choice enables an investigation of the effect of precession generated solely by the addition of the chamber section on the scalar mixing field of the simple jet.

The scalar mixing field has been determined for each of the simple jet and FPJ cases from the same experimental measurement technique. The instantaneous jet concentration field, ξ, has been determined using the planar Mie scattering technique described in Section 2.2.3. A digital camera images a 270×180mm area of the flow that is illuminated by a light sheet passing through the jet axis, with each pixel having a spatial resolution of 0.47×0.47×0.25mm. Statistical analysis of the jet concentration data has been performed from a set of 600 instantaneous images. A definition of those statistical quantities appears in the relevant sections that follow.

3.4.2. Concentration Measurements in a Simple Jet

The scalar mixing field has been determined for the simple jet issuing through an orifice of diameter d = 2.3mm with Re_d = 22,300. The scalar mixing field is characterised by instantaneous, mean and fluctuating jet concentration measurements, which are compared with similar published statistical data. These include the centre-line decay of the mean jet concentration, $\overline{\xi}$, the concentration half-width of the jet, $d_{½}$, radial profiles of $\overline{\xi}$ and the RMS concentration fluctuation, ξ_{RMS}, and centre-line concentration fluctuation intensity, $\xi_{RMS}/\overline{\xi}$, also termed the unmixedness, in the measurement range of $0 \leq x \leq 110d$. Becker *et al.* (1967) have determined each of these statistical quantities for the jet issuing from a nozzle with a smooth contraction, and therefore represents a suitable database with which to compare results for the present jet. Reference is also made to other publications, which represent a current review of jet concentration statistics or provide more rigorously determined data where appropriate, so that comparison is indirectly made with an extensive set of published data for the case of the jet issuing from a nozzle with a smooth contraction.

Three representative instantaneous images of the jet concentration field are shown in Figure 3.10. The good spatial and temporal resolution throughout all but the potential core region is also clearly evident. A local maximum in the potential core, determined from a 3×1pixel average, has been chosen to provide a reference for the concentration of pure jet fluid $\xi = 1$ in each instantaneous image. Point values corresponding to each pixel in the image plane are displayed Figure 3.10 using a colour map for the range $0 \leq \xi \leq 0.5$. Concentrations for the range $\xi > 0.5$ are shown in black. It is apparent that there is very rapid mixing between the jet and ambient fluid streams. Only a small region with $\xi > 0.5$ is associated with the potential core and with some of the fluid immediately downstream from the potential core.

The mean jet concentration field, defined as

$$\bar{\xi} = \frac{1}{N}\sum_{1}^{N}\xi,$$

has been determined for the simple jet from the set of instantaneous images. A graph of the radial profiles of $\bar{\xi}$ at cross-sections $x = 20d$, $40d$, $60d$, $80d$ and $100d$ is presented in Figure 3.11. The distribution shows the progressive decay in centre-line jet concentration due to dilution as the simple jet spreads widely with increasing axial distance downstream from the nozzle. The symmetry of the data about the jet axis demonstrates that the jet axis and the camera are well aligned in the image plane, and that the effects of light attenuation by the flow are small.

Figure 3.12 shows a graph of $\bar{\xi}$ along the centre-line of the simple jet, which shows $\bar{\xi}$ is inversely proportional to the distance from the nozzle, x. The relationship for the mean centre-line decay is then derived by linear regression to be

$$\frac{1}{\bar{\xi}} = 0.449(x - x_0)/d$$

where $x_0 = 4.5d$ is the location of the virtual origin. The linearity is further evidence of a well aligned sheet.

The scalar mixing results for the simple jet case are compared with air/air jet concentration data from Becker *et al.* (1967), issuing from a nozzle with a smooth contraction. Their results for $\bar{\xi}$ also follow a linear relationship, but their constant of proportionality is 0.195, which shows that the constant of the present jet issuing from an orifice is 0.449 and thus has a more rapid decay. Pitts (1991) presents a review of results from many scalar mixing studies of jets and reports a wide range, between 0.196 and 0.312, for the constant of proportionality. It was noted that measurement uncertainties might contribute to the reported variations, namely coflow, buoyancy effects and the effect of initial flow conditions. The data cited in Pitts (1991) study was obtained from nozzles with smooth jet contractions and not orifii. That the difference between the present data and that of Becker *et al.* (1967) is not simply experimental error is demonstrated by Nobes (1997), who, using the identical experimental apparatus and technique, obtained agreement with Becker *et al.* (1967) for a jet generated by a smooth contraction nozzle. The higher mean centre-line decay of concentration from the present jet in comparison to Becker *et al.* (1967) is therefore quite acceptable, and is consistent with there being genuine differences in the flow. Further support for this conclusion is found in the greater rate of jet spread, discussed below.

The concentration half-width, $d_{½}$, is used to provide a quantitative measure of the width of the jet, where $d_{½} = d_{\xi = 0.5}$. Figure 3.13 shows a graph of $d_{½}$ as a function of axial distance. The graph shows the constant half-width of the jet, with a relationship derived by linear regression to be

$$d_{½} = 0.230(x - x_0^*).$$

where $x_0^* = 4.0d$ is the location of the half-width virtual origin. The jet spread half-angle is then 6.6°, slightly greater than Becker *et al.* (1967) who show a jet spread half-angle of 6.0°, consistent with increased centre-line decay, mentioned earlier.

The RMS jet concentration fluctuation, ξ_{RMS}, has been determined for the simple jet from the set of instantaneous images as

$$\xi_{RMS} = \left(\frac{1}{N}\sum_1^N \left(\xi - \overline{\xi}\right)^2\right)^{\frac{1}{2}}.$$

Graphs of the radial profiles of $\overline{\xi}$ and ξ_{RMS} are presented in Figure 3.14 and Figure 3.15 respectively. These radial profiles are presented as a normalised form of the radial $\overline{\xi}$ results that were presented in Figure 3.11. Here $\overline{\xi}$ and ξ_{RMS} are normalised with the local centre-line values and the radius, r, using the parameter $r/(x - x_0^*)$, where x_0^* is the half-width virtual origin which has been determined above. Results from Becker *et al.* (1967) using this normalisation are also presented in these graphs for comparison.

It is apparent that self-similarity in the mean is obtained by $x \approx 20d$. The different nature of the similarity curve when compared with the data from Becker *et al.* (1967) is consistent with the slightly wider spread of the present jet. Self-similarity in ξ_{RMS} is not reached until much farther downstream, at $x \approx 80d$. This represents a difference in the distance required for higher order moments of the jet concentration to reach self-similarity than has been determined by other researches.

The graph of the unmixedness, $\xi_{rms}/\overline{\xi}$, on the jet centre-line is presented in Figure 3.16. In the region close to the nozzle, $0 \leq x \leq 3d$, the low initial values of unmixedness are associated with pure jet fluid and hence negligible concentration fluctuation that is associated with the potential core of the jet. The data shows a rapid increase in unmixedness to a peak or "hump" at $x = 10d$, deduced to be associated with the break-up of the potential core and the passage of large-scale coherent structures in their formative region as discussed by Nobes (1997). An asymptotic value of $\xi_{RMS} = 0.30\overline{\xi}$ is obtained for $x \geq 80d$. In the asymptotic region, both the mean and RMS jet concentrations show self-similar behaviour. Becker *et al.* (1967) found an asymptotic unmixedness value of $\xi_{RMS} = 0.22\overline{\xi}$ for the jet from a nozzle with a smooth contraction. The review paper by Pitts (1991) reports asymptotic unmixedness values of $0.18\overline{\xi} \leq \xi_{RMS} \leq 0.37\overline{\xi}$, although the most rigorously determined asymptotic value for the unmixedness for a jet nozzle with a smooth contraction and top-hat velocity profile is considered to be $\xi_{RMS} = 0.23\overline{\xi}$. It should be noted that the higher value of the centre-line unmixedness determined for the present jet relative to the simple jet from a smooth contraction cannot be attributed to poor spatial resolution since poor spatial resolution has been shown by Dowling and Dimotakis (1990) to result in an under-estimation of fluctuations. While misalignment of the sheet would result in a increase in the measured unmixedness, since unmixedness increases with radial distance from the jet centre-line this is not believed to occur here. Any misalignment would also result in reduced spread of the jet being measured and loss of self-similarity which is not found. While the present results are well within the range of published results the higher unmixedness, higher centre-line decay and greater spread are consistent with genuine differences in the flow compared with that studied by Becker *et al.* (1967), suggesting that the effect of the orifice on the turbulent structure at the nozzle exit propagates into the far field. That is, the character of fully-developed turbulent flow in the jet produced by an orifice plate is fundamentally different from that produced by a smooth contraction. That this finding is genuine, and not an artefact of the measurement technique, is supported by the experimental data of Nobes *et al.* (1996a) who used the identical experimental apparatus used in the present experiments, but measured the jet flow produced by a nozzle with a smooth contraction. The asymptotic value of centre-line unmixedness determined by that investigation is $\xi_{RMS} = 0.23\overline{\xi}$, identical to the value recommended by Pitts (1991). Additional support for this finding is also presented later in the more detailed statistical analysis later in this chapter.

The present jet generated by an orifice plate has been well characterised and shown to possess symmetry in the mean jet concentration, constant centre-line concentration decay and half-width spread, self-similarity in the mean concentration field for $x \geq 20d$ and in the RMS concentration field for $x \geq 80d$, and to have an asymptotic value of the unmixedness in the far field. The spread, decay rate and far field unmixedness are all higher than those generated by the jet issuing from a smooth contraction. These characteristics demonstrate that the jet produced from an orifice is different from that issuing from a nozzle with a smooth contraction but possesses the trends and features found by previous researchers. The next section demonstrates that the effect of precession is to change further the character of the scalar mixing field.

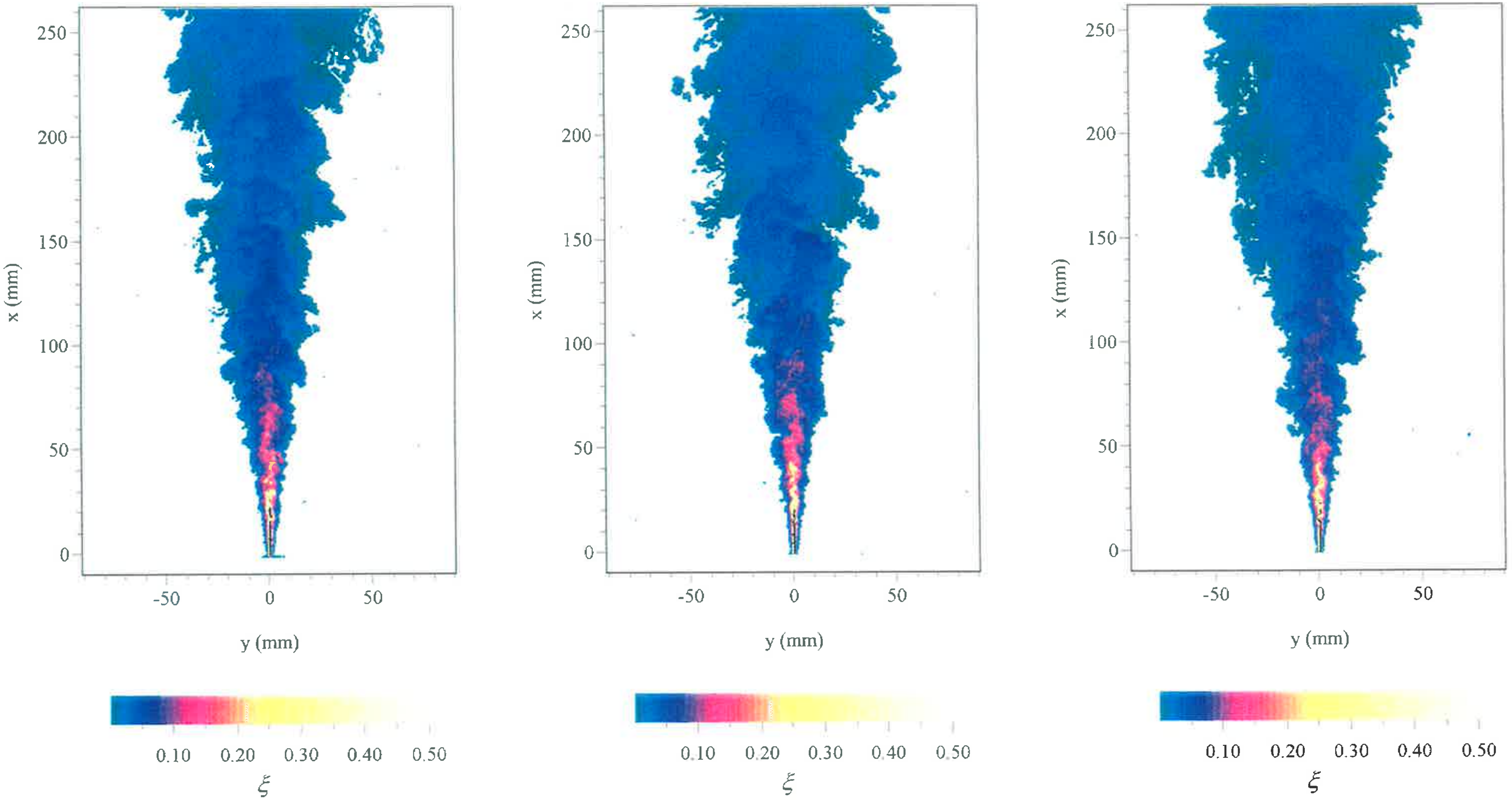

(a) (b) (c)

Figure 3.10 Instantaneous false colour images of jet concentration, ξ, for the simple jet flow. Black is used for $\xi > 0.5$. ($d = 2.3$ mm jet orifice, $\mathrm{Re}_d = 22{,}300$, Working fluid = air)

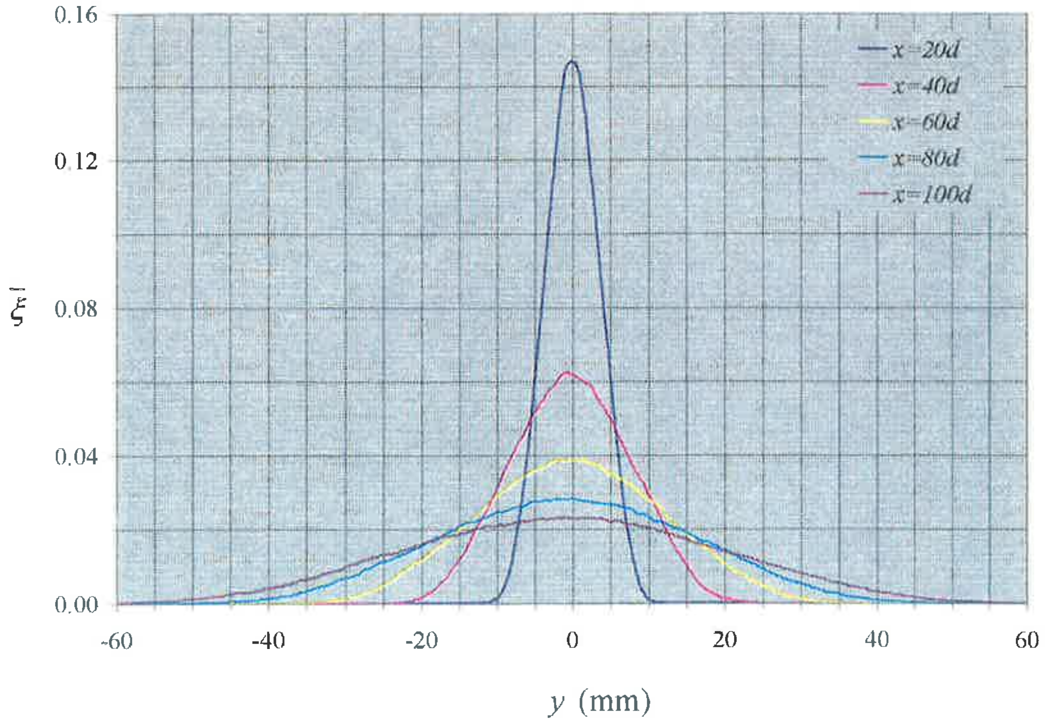

Figure 3.11 Distributions of the radial mean jet concentration, $\bar{\xi}$, for the simple jet flow. (Experimental conditions as for Figure 3.10)

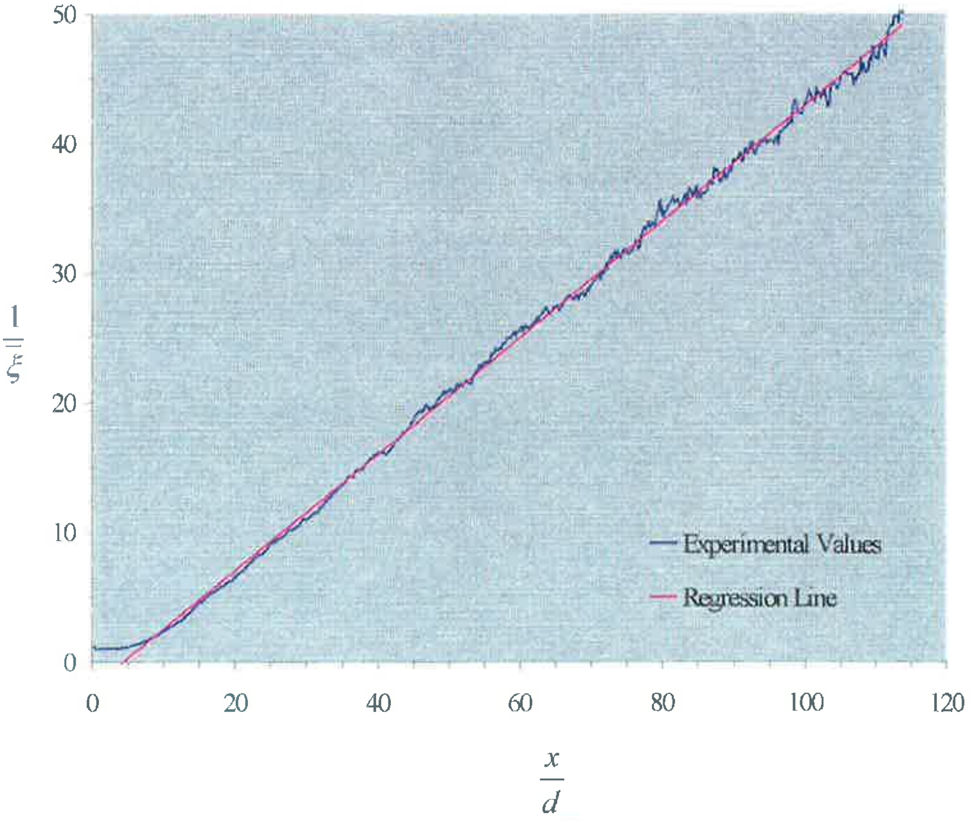

Figure 3.12 The mean jet concentration, $\bar{\xi}$, on the jet axis for the simple jet flow. A regression line is included showing the inverse relation between $\bar{\xi}$ and the axial distance from the nozzle, x. (Experimental conditions as for Figure 3.10)

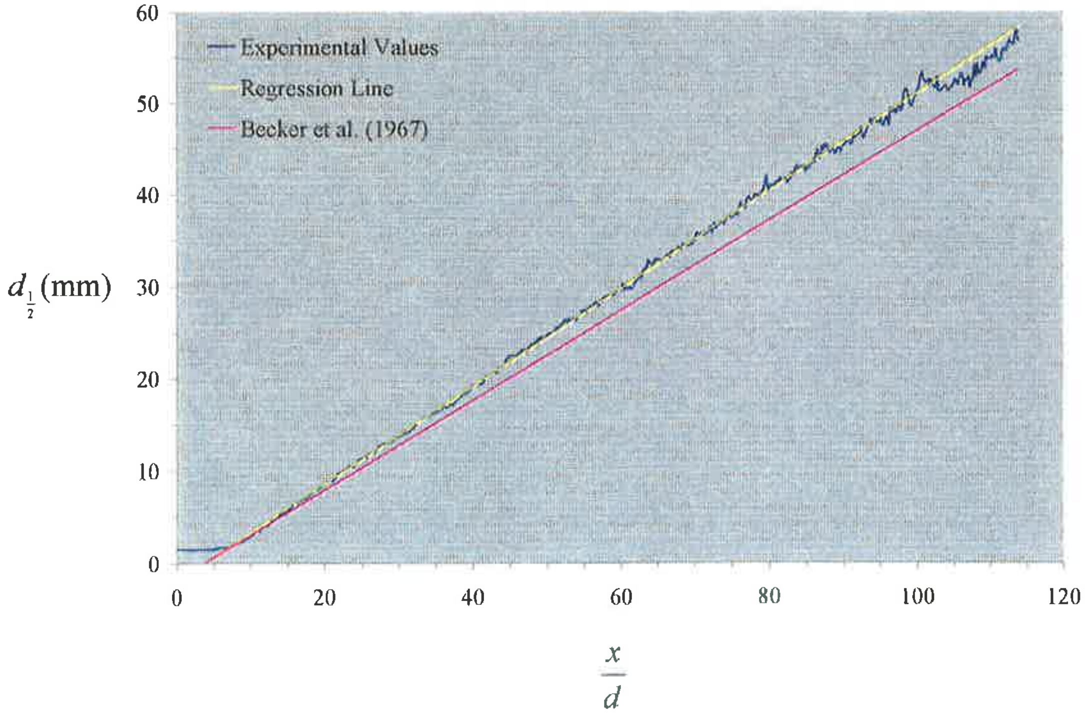

Figure 3.13 The concentration half-width, $d_{\frac{1}{2}}$, for the simple jet flow. (Experimental conditions as for Figure 3.10)

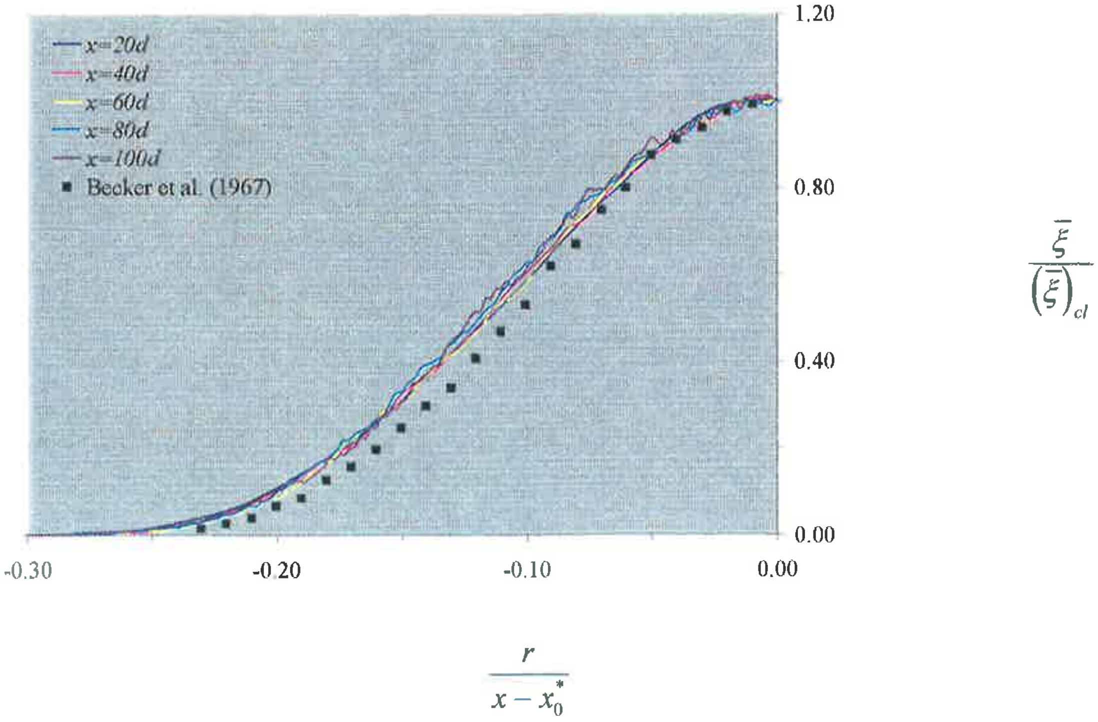

Figure 3.14 Normalised radial profiles of the mean jet concentration, $\bar{\xi}$, for the simple jet flow. (Experimental conditions as for Figure 3.10)

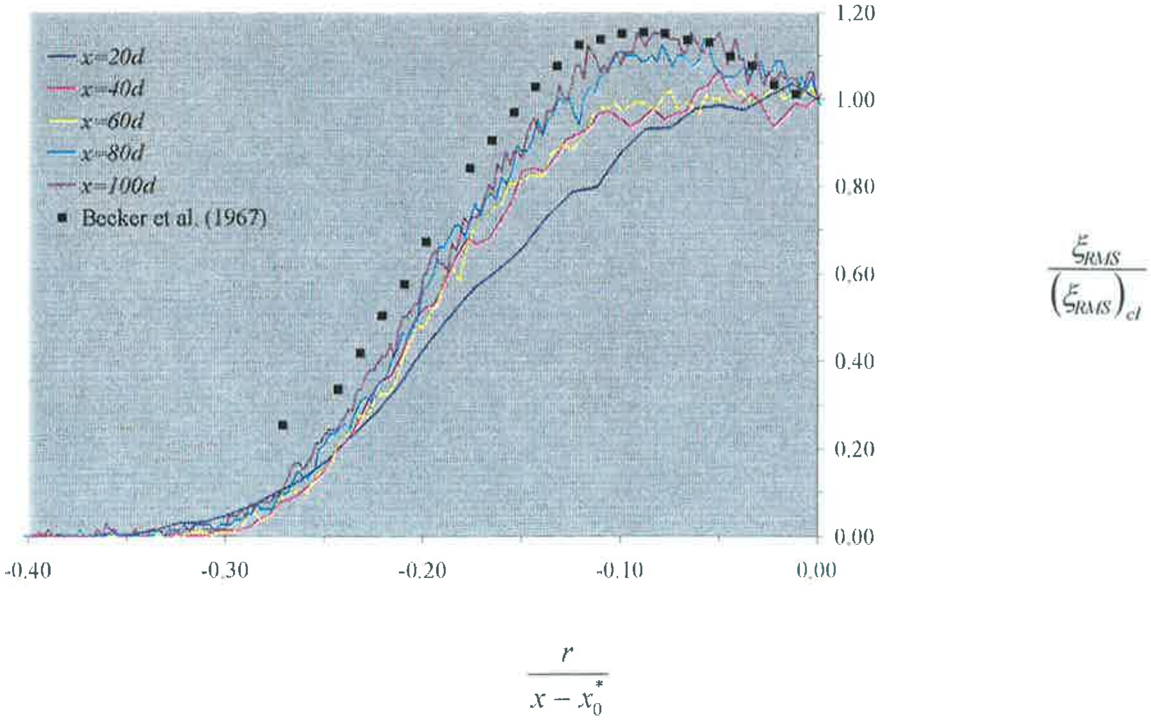

Figure 3.15 Normalised radial profiles of RMS jet concentration fluctuation, ξ_{RMS}, for the simple jet flow. (Experimental conditions as for Figure 3.10)

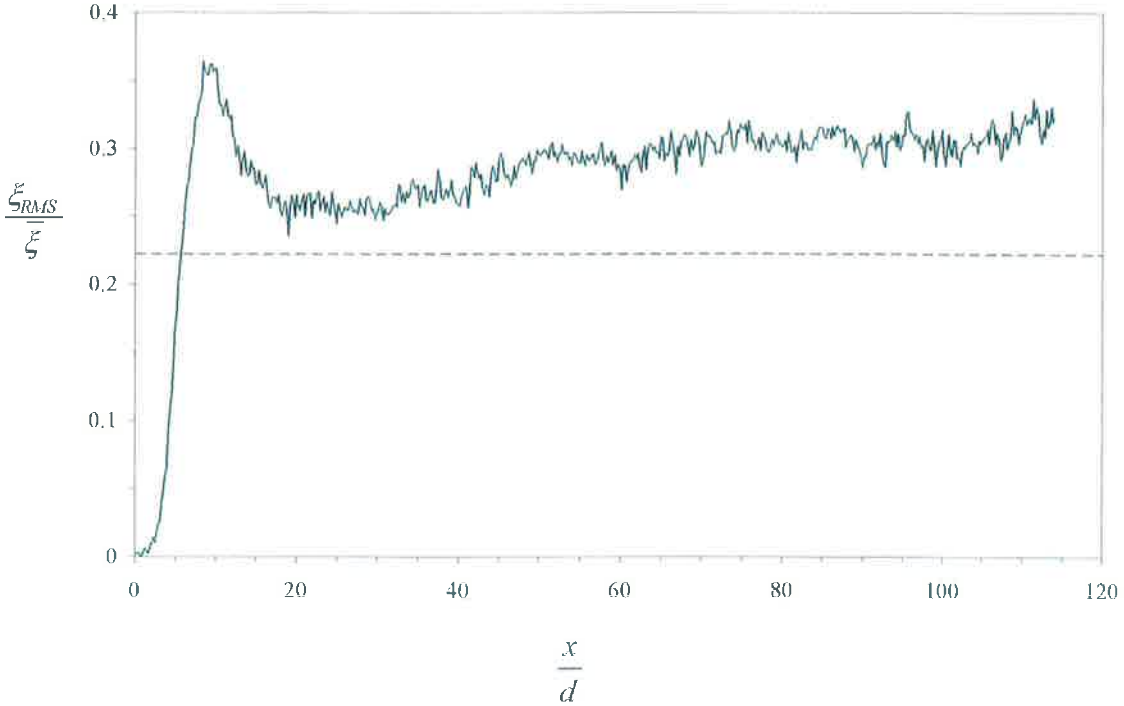

Figure 3.16 Intensity of the jet concentration fluctuations, $\xi_{rms}/\bar{\xi}$, on the jet axis for the simple jet flow. A reference value of $\xi_{rms} = 0.22\bar{\xi}$ is shown from the data of Becker *et al.* (1967). (Experimental conditions as for Figure 3.10)

3.4.3. Concentration Measurements in a Fluidic Precessing Jet

The scalar mixing field has been determined for the FPJ nozzle of characteristic chamber diameter, D = 13mm. The Reynolds number is characterised by the flow variables through the upstream throat of the nozzle d_1 = 2.3mm, with $\mathrm{Re}_{d_1} = 20{,}500$. Mean and RMS jet concentration data are compared with results from the simple jet obtained using an identical technique and apparatus, and similar flow conditions to those that have been presented for the simple jet in Section 3.4.2. Measurements include the centre-line $\overline{\xi}$, $d_{½}$ and $\xi_{RMS}/\overline{\xi}$, and radial profiles of $\overline{\xi}$ and ξ_{RMS}, in the range $0 \leq (x - L) \leq 110$d, where the length of the FPJ chamber section downstream of the jet throat is $L = 16d$.

Three representative images of the instantaneous jet concentration, ξ, in the FPJ flow are presented in Figure 3.17. The absolute values of concentration in these images are considered to be reasonable, although they are at present open to some question due to problems in determining an absolute reference for "pure" fluid from the potential core (Section 2.2.3). The scaling approach followed is similar to that used for the simple jet. A local maximum near to the exit from the chamber, determined from a 3×3pixel average, has been nominated to represent pure jet fluid in each instantaneous image. One possible error in this assumption arises because previous work with related, but different, configurations of FPJ nozzle showed that some ambient fluid is drawn into the chamber (Nathan and Luxton, 1991b). However more recent work by Hill (1998), has shown that for the present FPJ nozzle configuration, which includes a centre body (Figure 2.2), the amount of ambient fluid that is drawn into the present (sub-atmospheric) nozzle chamber is extremely small. This suggests that the effect of dilution within the nozzle chamber is not significant. Another possible source of error in the reference is that the jet emerging from the FPJ nozzle may not always be directly within the plane of the light sheet, so that the maximum concentration may represent fluid for which some mixing with ambient fluid has already taken place outside the chamber. Hence the existence of a 3×3pixel location to use a reference for fluid representing $\xi = 1.0$ is not assured. Despite this apparent limitation, many of the key findings are based on normalised jet concentration, and thus do not require an absolute reference.

In the instantaneous images of the jet concentration field presented in Figure 3.17 the value of the jet concentration, ξ, at each pixel is shown in false colour for the range $0 \leq \xi \leq 0.5$ with jet concentrations of a higher value coloured black. A significantly greater region containing mixed fluid with jet concentration $\xi > 0.5$ is evident in the region immediately downstream from the FPJ nozzle than was found for the simple jet case (Figure 3.10). The scale of the fluid structures within the FPJ flow is significantly larger than that of the simple jet everywhere. "Peninsulas" and "islands" of jet fluid are found to occur at the edge of the jet flow, associated with ejections of jet fluid and incursions of ambient fluid toward the jet axis.

The radial profiles of $\overline{\xi}$ for cross-sections $(x - L) = 20d$, $40d$, $60d$, $80d$ and $100d$ are plotted in Figure 3.18. The high degree of symmetry demonstrates that the jet axis and the camera are well aligned. The distributions are directly comparable with those for the simple jet case presented in Figure 3.11, noting that the exit plane of the FPJ nozzle is located at $L \approx 20d$. Comparison shows increased spread and yet decreased dilution of the jet fluid downstream from the FPJ nozzle. The wider spread of the FPJ flow is consistent with decreased flow velocity, and consequently lower local strain rates and longer jet fluid residence time, in the imaged region. This suggests scalar mixing of the jet and ambient fluid streams is reduced, resulting in an increase in the mean jet concentration on the centre-line.

The decay rate of centre-line jet concentration, $\overline{\xi}$, of the simple jet flow and the FPJ flow are compared directly in Figure 3.19. The data are presented with a common origin ($x = 0$), corresponding to the location of the jet throat. The throat is upstream from the imaged area for the FPJ case so that data are only measured downstream from the nozzle exit, which is located at $x = L$ ($L = 16d$). The majority of the data is more-or-less linear and shows that $\overline{\xi}$ is roughly inversely proportional to x for both jet flows. The relationship for the mean centre-line decay of the FPJ is derived by linear regression to be

$$\frac{1}{\overline{\xi}} = 0.170(x - L - x_0)/d$$

where $x_0 = -10.4d$ so that the virtual origin is upstream from the exit plane of the FPJ nozzle. It is apparent that precession acts to roughly half the $\overline{\xi}$ decay rate of the jet.

The jet half-widths, $d_{½}$, of the simple jet flow and FPJ flow are compared in Figure 3.20. The FPJ flow has a very wide initial spread, with a half-angle of approximately 40° in the initial region immediately downstream from the nozzle exit. However this angle reduces downstream so that an approximately constant spreading half-angle of 11° is achieved for $(x - L) \geq 60d$. In the region $60d \leq (x - L) \leq 110d$ the linear half-width is described by a relationship derived by linear regression to be

$$d_{½} = 0.364(x - L - x_0^*)$$

where $x_0^* = -46.8d$ is the location of the half-width virtual origin. The asymptotic value of spread of the half-angle of the FPJ flow is 11°, which is nearly double the 6.6° for the comparable simple turbulent jet.

Radial profiles of $\overline{\xi}$ and ξ_{RMS} are presented in Figure 3.21 and Figure 3.22 respectively. The jet concentration is normalised by the local centre-line value and the radial coordinates by the nozzle diameter following the normalisation applied to the simple jet flow in Section 3.4.2. Each profile of $\overline{\xi}$ for $(x - L) \geq 40d$ collapses to a common curve, which shows that the mean jet concentration has achieved good self-similarity in the mean at that station. The transition to linear growth in jet half-width and to self-similarity in the mean jet concentration suggests a transition from a region dominated by the coherent motions associated with the jet precession, immediately downstream from the nozzle, toward a region in which the turbulence is approaching full development. However complete collapse of the radial ξ_{RMS} profiles, indicating genuine self-similarity, is not fully achieved even at the end of the imaged region, $(x - L) = 100d$. By contrast self-similarity for the simple jet flow is achieved in the mean at $x \approx 20d$ (see Figure 3.14) and for the RMS fluctuation at $x \approx 80d$ (see Figure 3.15).

The centre-line unmixedness, $\xi_{RMS}/\bar{\xi}$, is presented in Figure 3.23. The peak at $(x - L) \approx 7d$ is clearly associated with the precessional motion (which appears in the two-dimensional plane as a flip-flop motion) of the jet emerging from the nozzle chamber. The unmixedness has not achieved an asymptotic value within the imaged area, unlike the simple jet case which achieves an asymptotic value at $x \approx 80d$. This result is consistent with the greater absolute distance required to achieve self-similarity in the normalised radial ξ_{RMS} results. The unmixedness value for the FPJ flow is clearly greater than that for the present simple jet case ($\xi_{RMS} > 0.3\bar{\xi}$), and is still rising at the end of the imaged region to reach a value of $\xi_{RMS} \approx 0.47\bar{\xi}$. That an asymptotic state has not been reached further supports the conclusion that the far-field data is not fully developed at $(x - L) = 100d$. That the unmixedness is not converging to the value of the simple jet further suggests that the structure of the fully developed turbulent motions is inherently different from that produced by either the simple jet issuing from an orifice or that from a smooth contraction.

In summary, a comparison of the mean and fluctuating jet concentration measurements of simple jet and FPJ flows shows clear differences in all scalar mixing characteristics. The effect of precession of a jet caused by the addition of a chamber is to increase the spread angle and decrease the mean rate of axial dilution of the jet fluid downstream from the jet origin. Self-similarity of the mean radial jet concentration is achieved for $(x - L) \geq 40d$, however the turbulence field is not yet full established and the RMS radial jet concentration does not achieve self-similarity for $(x - L) \leq 110d$. The asymptotic value of the centre-line unmixedness has not been reached within the range of measurements, but the trends demonstrate that it is significantly higher than that produced by a simple jet flow issuing from a nozzle with an orifice or a smooth contraction. It is clear that the chamber cannot add any net energy to the jet entering the chamber. It is also clear that the chamber dramatically alters the structure of mixing in the near nozzle region. The inference is that the distribution of turbulent energy is shifted away from the fine-scales and into large-scales, without significantly changing the total kinetic energy, and that this different structure propagates through to the far field.

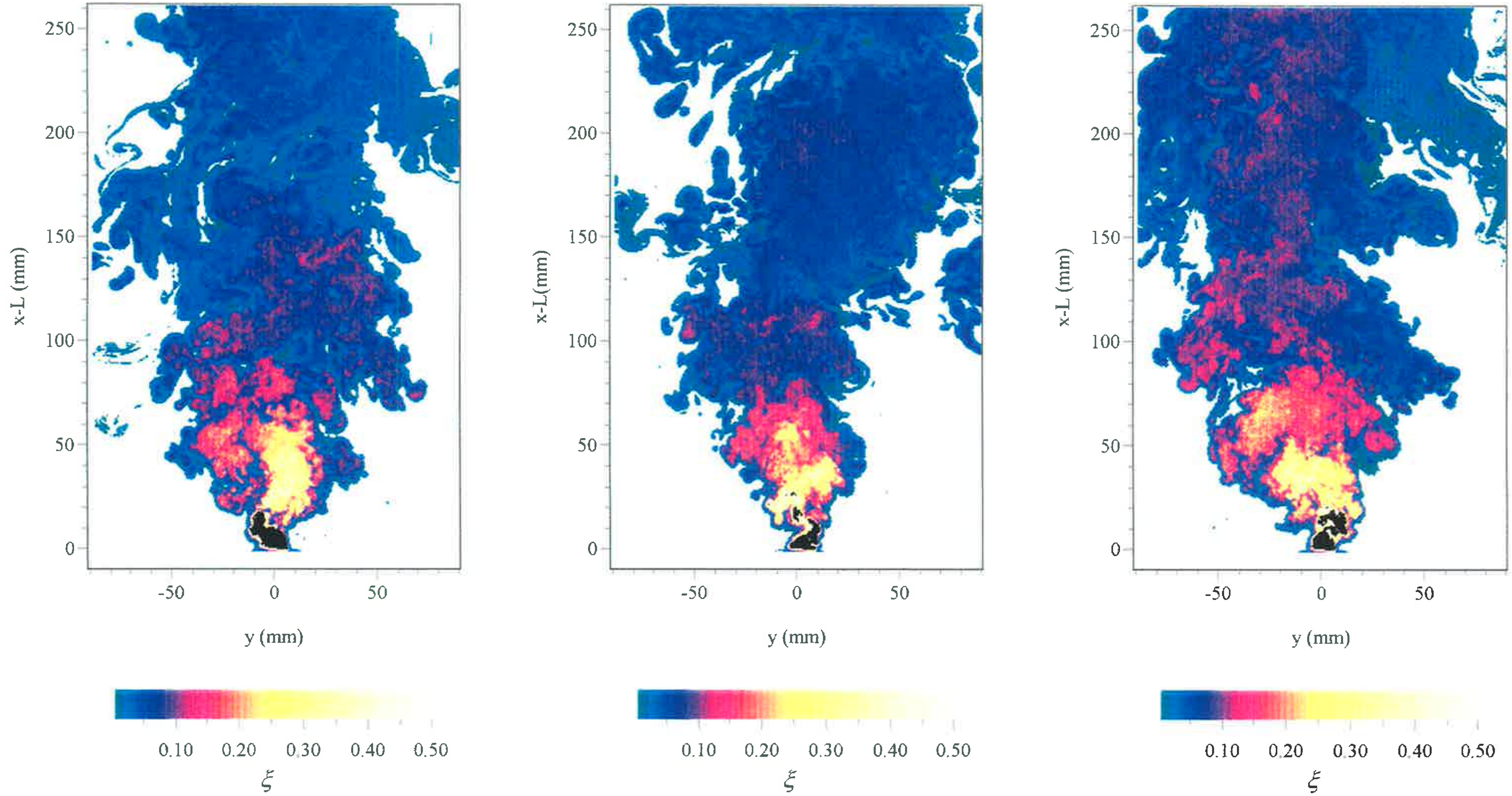

(a) (b) (c)

Figure 3.17 Instantaneous false colour images of jet concentration, ξ, for the FPJ flow. Black is used for $\xi > 0.5$. ($d_1 = 2.3\text{mm}$, $D = 13\text{mm}$, $\mathrm{Re}_{d_1} = 20{,}500$, Working fluid = air)

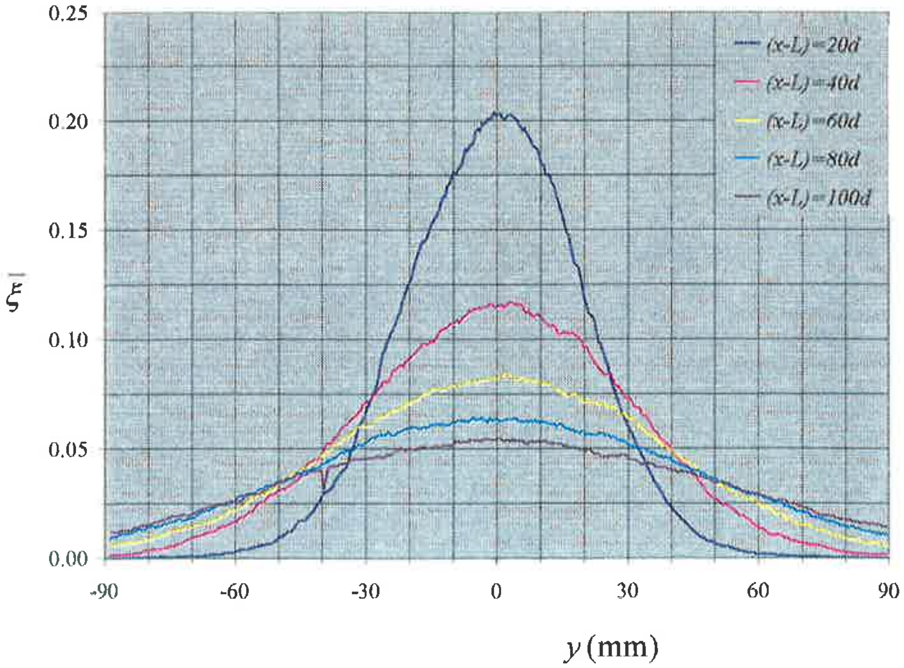

Figure 3.18 Distributions of the radial mean jet concentration, $\bar{\xi}$, for the FPJ flow. (Experimental conditions as for Figure 3.17)

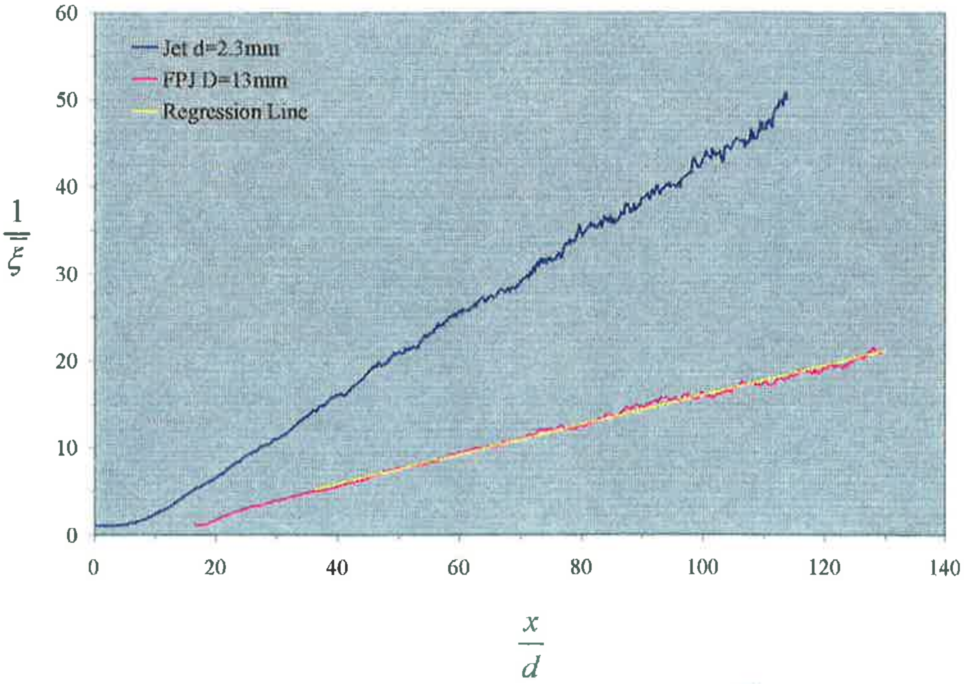

Figure 3.19 The mean jet concentration on the jet axis, $\bar{\xi}$, for the simple jet flow and the FPJ flow. (Experimental conditions as for Figure 3.10 and Figure 3.17 respectively)

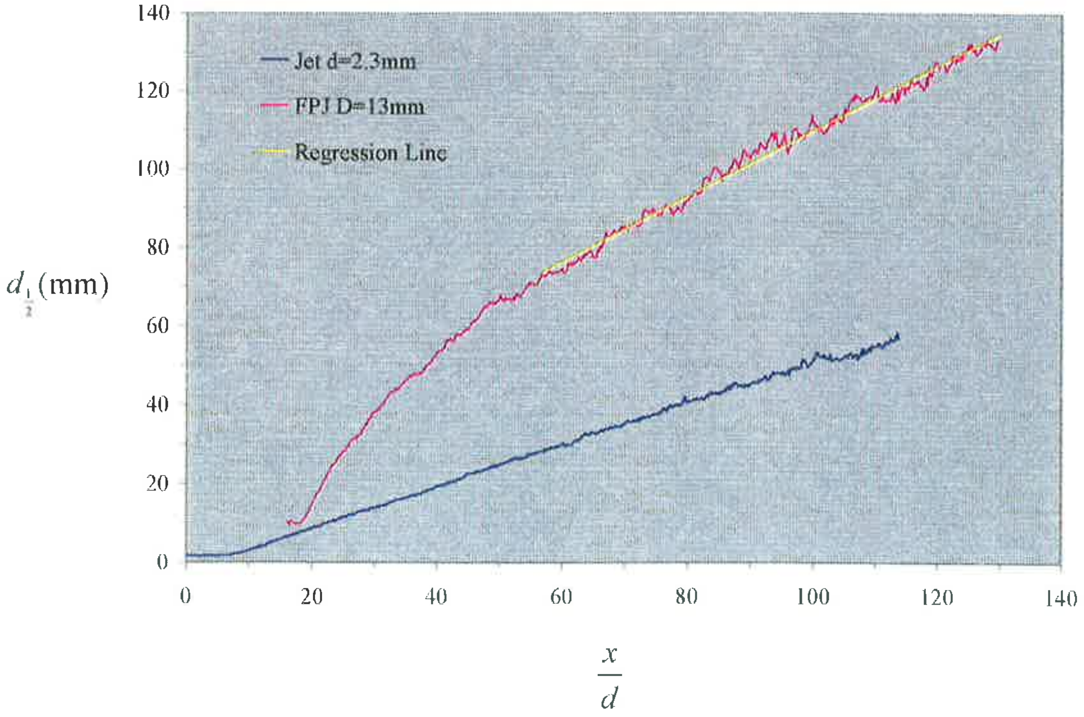

Figure 3.20 The jet concentration half-width, $d_{\frac{1}{2}}$, for the simple jet flow and the FPJ flow. (Experimental conditions as for Figure 3.10 and Figure 3.17)

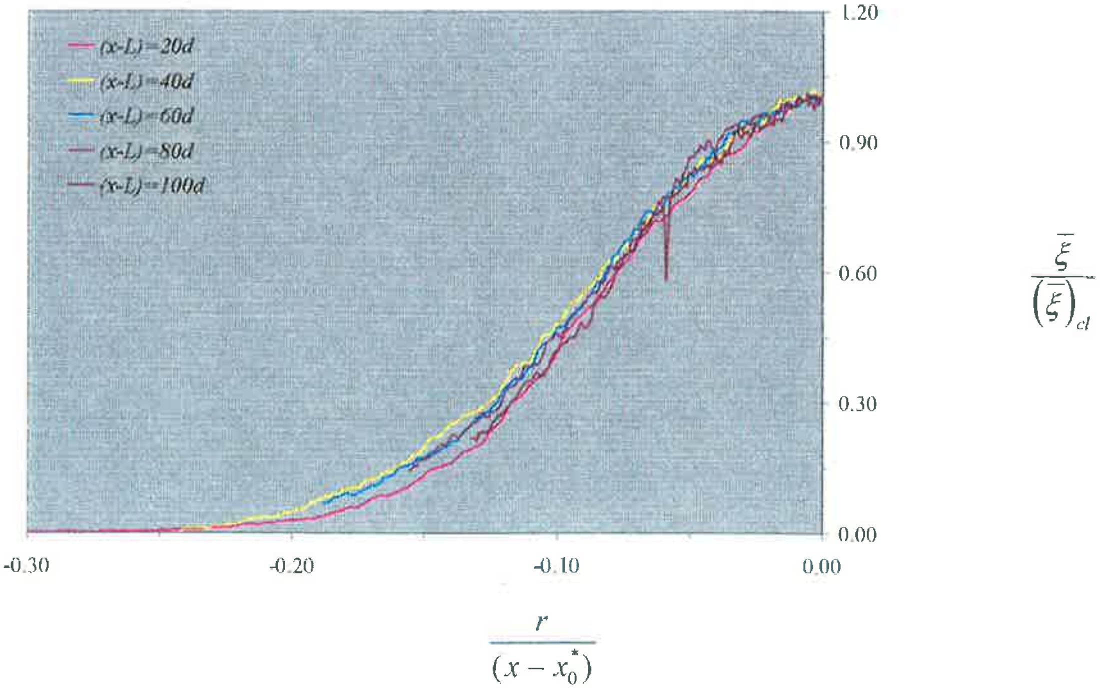

Figure 3.21 Normalised radial profiles of the mean jet concentration, $\bar{\xi}$, for the FPJ flow. (Experimental conditions as for Figure 3.17)

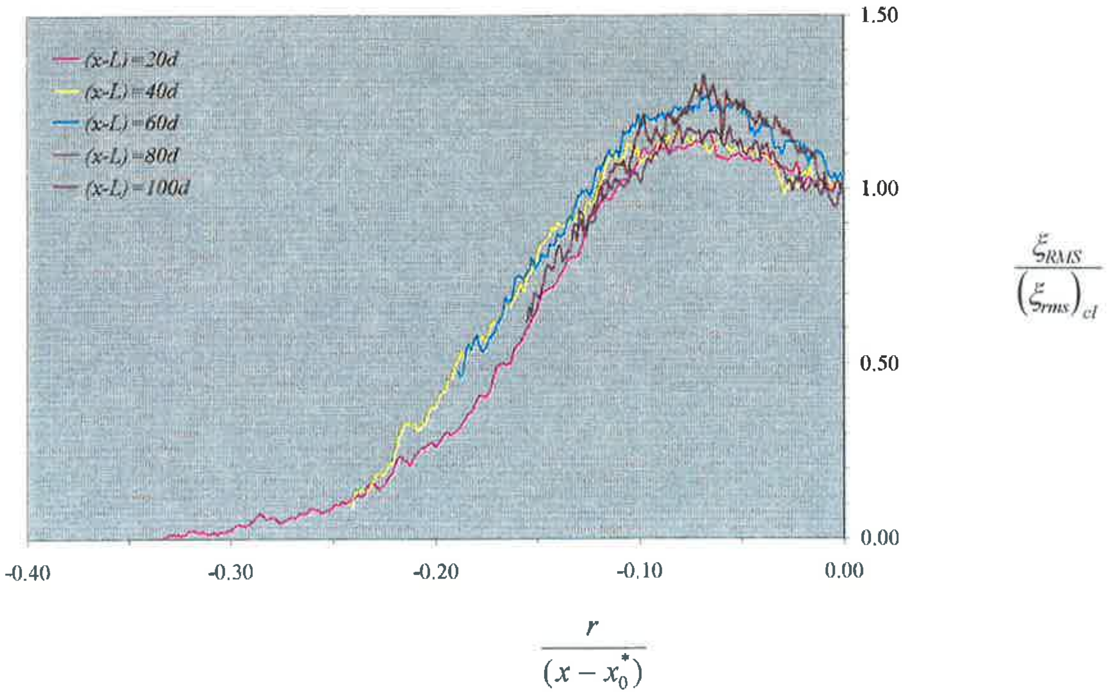

Figure 3.22 Normalised radial profiles of RMS jet concentration fluctuation, ξ_{RMS}, for the FPJ flow. (Experimental conditions as for Figure 3.17)

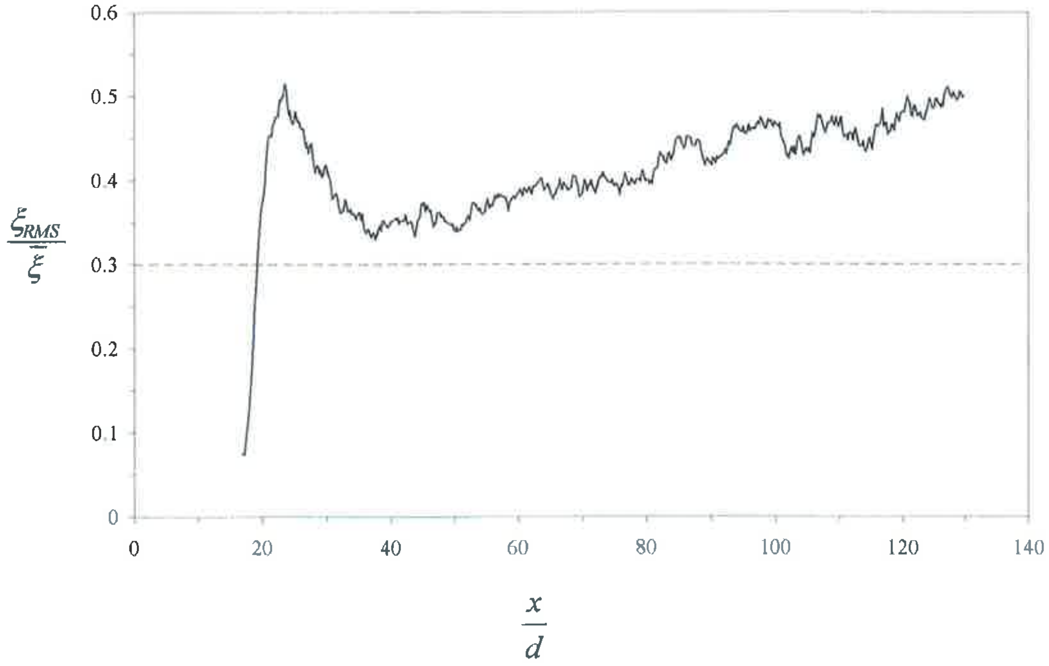

Figure 3.23 Intensity of the jet concentration fluctuations, $\xi_{RMS}/\overline{\xi}$, on the jet axis for the FPJ flow. A reference value of $\xi_{rms} = 0.30\overline{\xi}$ is shown from the simple jet flow data in Figure 3.16. (Experimental conditions as for Figure 3.17)

3.4.4. Intermittency

The entrainment and mixing of ambient fluid in the simple turbulent jet and FPJ flows can also be compared in terms of the centre-line intermittency. The intermittency, I, at a point (x,y) is defined as

$$I = \int_0^\infty \Psi \, dt \qquad \text{where} \qquad \psi = 0 \text{ for } \xi = 0,$$

$$\text{and} \qquad \psi = 1 \text{ for } \xi > 0.$$

The intermittency at a point is the fraction of time that the fluid falls inside the instantaneous boundary between jet fluid and ambient fluid. It is determined from the probability of finding "pure" ambient fluid at that point. Here we associate "pure" ambient fluid with the jet concentration measurement range $0 \le \xi \le 0.005$. Broadening of this arbitrary range helps to compensate for the effects of noise in the measured values of ξ but degrades the resolution of "pure" fluid. The choice of the range defining pure ambient fluid determines the extent to which mixed fluid may be incorrectly regarded as pure ambient fluid. The relative error associated with this choice increases with axial distance as the mixed fluid becomes more diluted. At $(x - L) = 100d$ the mean jet concentration has decayed so that the range chosen for pure ambient fluid corresponds to about $\xi \le 0.25\overline{\xi}$ and $\xi \le 0.10\overline{\xi}$ for the simple jet and FPJ cases respectively. In addition the fluctuating jet concentrations are $\xi_{RMS} \approx 0.3\overline{\xi}$ and $\xi_{RMS} \approx 0.5\overline{\xi}$ for the simple jet and FPJ flows respectively. Thus at the end of the imaged region, I will be overestimated to a small degree for both cases. This resolution error does not effect the key findings of this section. Note also that the measure of I is not influenced significantly by the lack of an absolute reference for pure jet fluid at the exit of the FPJ nozzle, described in Section 3.4.3.

A comparison of I along the centre-line for the jet and FPJ flows is presented in Figure 3.24. The data is again presented with a common origin, corresponding to the location of the jet throat with or without the FPJ chamber attached. The results show that negligible ambient fluid, less than 1%, is entrained to the centre-line of the simple jet. This is in agreement with Dowling and Dimotakis (1990), who show that no ambient fluid is found on the jet axis in the range $20d \leq x \leq 80d$ when using air as the working fluid. In contrast up to 5% ambient fluid is found on the centre-line of the FPJ flow. This result demonstrates that jet precession results in large-scale transport of ambient fluid to the jet axis. However this large-scale engulfment mechanism does not act to mix the ambient and jet fluid streams rapidly at the fine-scales, as demonstrated by the overall decrease in centre-line mean jet concentration decay rate (Figure 3.19). This further demonstrates that the structure of the turbulent mixing process is fundamentally altered by precession.

The presence of ambient fluid, or near ambient concentration fluid, on the jet axis suggests that pockets or layers of mixed fluid that are subjected to a significantly reduced local strain rate, in comparison with that in the simple jet flow, exist in the FPJ flow. It is suggested therefore that the effect of precession of a jet is to decrease fine-scale mixing by reducing the role of local straining within that region of fluid beyond the immediate exit region of the nozzle, generating the jet precession.

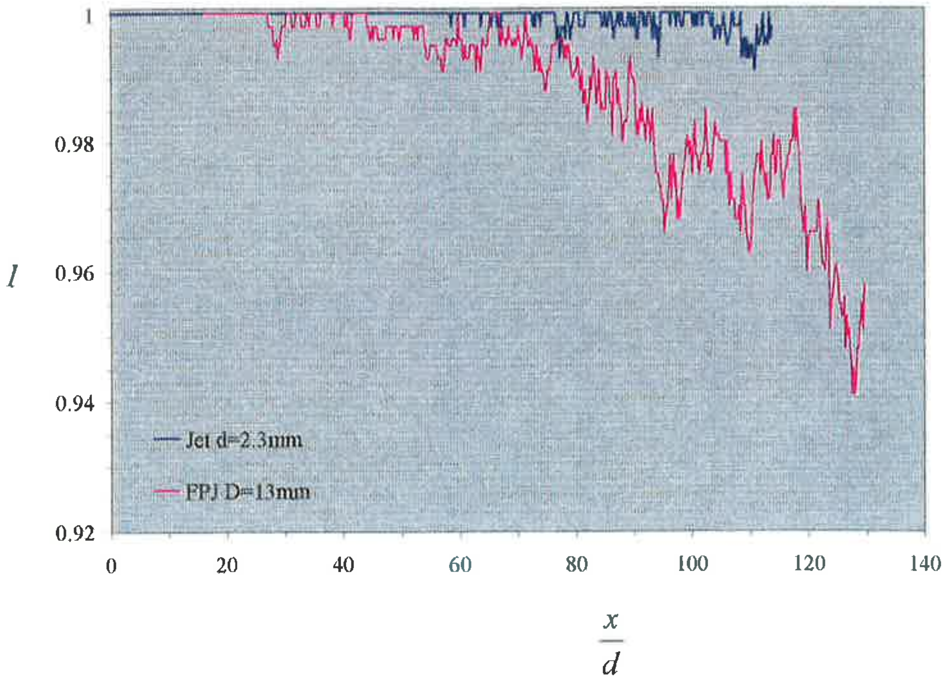

Figure 3.24 Intermittency, I, on the jet axis for the simple jet flow and the FPJ flow. (Experimental conditions as for Figure 3.10 and Figure 3.17)

3.4.5. Mixed Fluid Distributions

The statistical distribution of the jet concentration in a flow can also be assessed by means of the probability density function of the jet concentration, pdf(ξ). The pdf of jet concentration is the fraction of the time that the instantaneous jet fluid concentration at a point falls inside a concentration range $\xi^* \pm \Delta\xi$. Here the pdf is calculated by "binning" the jet concentration measurements into finite subgroups of size $\Delta\xi = 0.005$ (ie. $0 \leq \xi \leq 0.005$, $0.005 \leq \xi \leq 0.015$, ... , $0.995 \leq \xi \leq 1.000$). Each bin then shows the relative distribution of mixed fluid in each jet concentration range. Two specific features that are commonly found in pdfs are a delta function located at either $\xi = 0$ ($0 \leq \xi \leq \Delta\xi$), associated with "pure" ambient fluid, or at $\xi = 1$ ($1 - \Delta\xi \leq \xi \leq \Delta\xi$), associated with "pure" jet fluid. Normalisation of the pdf requires that

$$\int_0^1 \mathrm{pdf}(\xi)\, d\xi = 1.$$

It is apparent that the average jet concentration is then given by

$$\bar{\xi} = \int_0^1 \xi . \mathrm{pdf}(\xi)\, d\xi$$

and the intermittency is given by

$$I = 1 - \int_0^{\Delta\xi} \mathrm{pdf}(\xi)\, d\xi$$

where the integral is the area associated with the lowest concentration bin $0 \leq \xi \leq 0.005$.

In the simple jet case, shown in Figure 3.25, the dominant feature of each pdf measured within the range $0 \leq x \leq 15d$ is the existence of a spike at $\xi = 1$ associated with the potential core of the jet $0 \leq x \leq 3d$ and the region downstream from the potential core. The relatively broad shape in the distributions of the pdf's over the region $0 \leq x \leq 20d$ is most likely to result from the poor spatial resolution. Poor resolution causes spatial averaging and an over-estimation of the amount of mixed fluid, where concentration gradients occur within the region imaged by individual pixels (Dowling and Dimotakis, 1990). The relative spatial resolution increases with growth of the structures and hence with x/d. For $x \geq 40d$ the shape of each pdf tends to a Gaussian-like distribution with negligible ambient fluid. This is consistent with the results of Dowling and Dimotakis (1990) that show pdfs for highly resolved jet concentration measurements in the range $20d \leq x \leq 80d$. Their results show that published pdf shapes display wide variability, which is attributed to the effect of initial conditions.

The FPJ flow data show some similar features to those of the simple jet flow in Figure 3.26, but there are clear quantitative differences. The presence of a less dominant $\xi = 1$ spike and the much broader spread demonstrates that a very much wider range of possible jet concentrations occur near the exit plane of the FPJ nozzle. For $(x - L) \geq 20d$ the maximum value of the pdf in the FPJ flow is typically half that of the simple jet flow, indicating a broader distribution of jet concentrations. The shape of each pdf eventually tends to a Gaussian-like distribution for $(x - L) \geq 20d$, similar in shape to that of the simple jet pdf but with a broader distribution and lower peak.

The average far field, centre-line, $\mathrm{pdf}(\xi/\overline{\xi})$ for both the simple jet and the FPJ cases is shown in Figure 3.27 using normalised coordinates. The choice of $\xi/\overline{\xi}$ as the independent variable removes the effects of downstream decay of $\overline{\xi}$ and also avoids the possible error associated with an inability to determine an absolute reference value of pure jet fluid for the FPJ data, as described in Section 3.4.2. Dowling and Dimotakis (1990) and Schefer *et al.* (1994c) demonstrate that $\xi/\overline{\xi}$ is the proper general similarity variable for jet concentration statistics, and consequently the $\mathrm{pdf}(\xi/\overline{\xi})$ are self-similar when the flow is fully developed.

The average pdf in the "similarity" region is determined from each measurement location on the centre-line for the region $80d \leq (x - L) \leq 100d$. This region corresponds unambiguously to flow in which the $\overline{\xi}$ and ξ_{RMS} achieves self-similarity and a constant unmixedness for the simple jet case. For the FPJ flow the constant spread angle and similarity of the mean suggests the flow is approaching full similarity. The distributions of $\xi/\overline{\xi}$ in this far field region have been compared at each location and found to be self-similar for both the simple jet and FPJ cases, based on a limited number of measurements at each location. Consequently the use of a larger number of measurement locations improves the statistical convergence of the normalised pdf.

At $(x - L) = 100d$ each bin in the pdf corresponds to a resolution of jet concentration of $\xi^* \leq \xi \leq \xi^* + 0.002$ and $\xi^* \leq \xi \leq \xi^* + 0.005$ for the simple jet and FPJ flows respectively. All measurements in the range $0 \leq \xi \leq 0.005$ are treated as $\xi/\overline{\xi} = 0$, so that for the simple jet case in the vicinity of $(x - L) = 100\mathrm{d}$ the ambient fluid bin necessarily slightly over-estimates the ambient fluid contribution to the pdf.

The shape of the average pdf for the simple jet flow is generally symmetric about $\xi = \overline{\xi}$. Negligible ambient fluid is present on the jet centre-line, consistent with the intermittency result presented in Section 3.4.4. These results are in agreement those of Dowling and Dimotakis (1990). By contrast the shape of the average pdf for the FPJ flow shows a significantly broader distribution of jet concentration than the simple jet and is clipped slightly at $\xi/\overline{\xi} = 0$. The existence of the broader peak in the pdf at $\xi = \overline{\xi}$ further indicates that precession acts to reduce the uniformity of the mixed fluid relative to a simple jet. The significant contribution to the pdf at $\xi/\overline{\xi} = 0$ further confirms the existence of pure ambient fluid, or near-ambient concentration fluid, on the jet centre-line.

The above results show that a broader distribution of mixed fluid exists on the centre-line of the FPJ flow than on the simple jet flow centre-line. This is consistent with the observations that the effect of precession of the jet is to increase the unmixedness, shown in Section 3.4.3, and increase intermittency, shown in Section 3.4.4. It is also consistent with a different structure of far field turbulence.

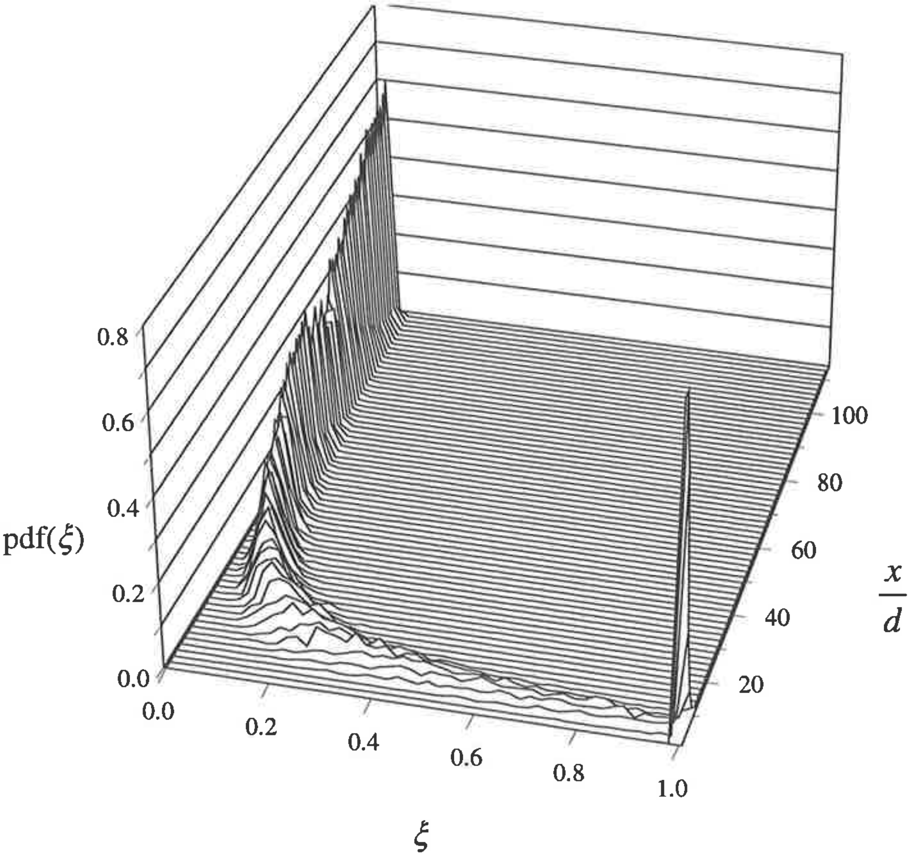

Figure 3.25 Probability distribution functions of the jet concentration, pdf(ξ), on the jet axis for the simple jet flow. (Experimental conditions as for Figure 3.10).

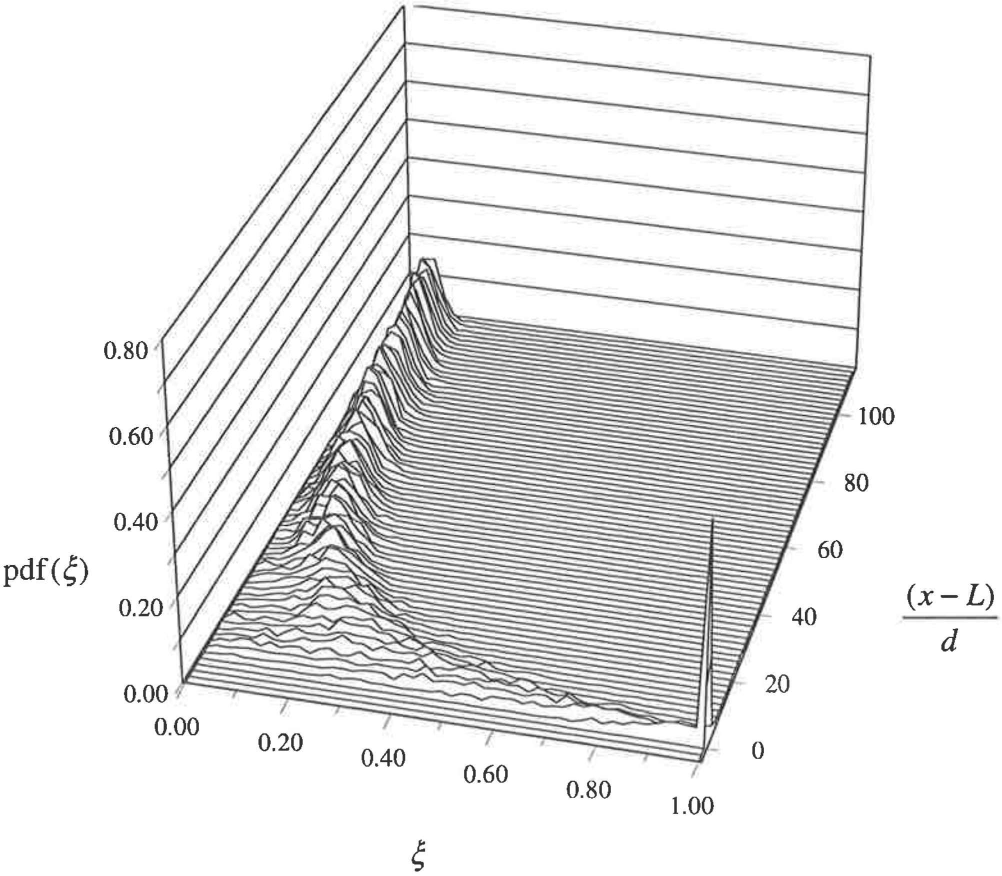

Figure 3.26 Probability distribution functions of the jet concentration, pdf(ξ), on the jet axis for the FPJ flow. (Experimental conditions as for Figure 3.17).

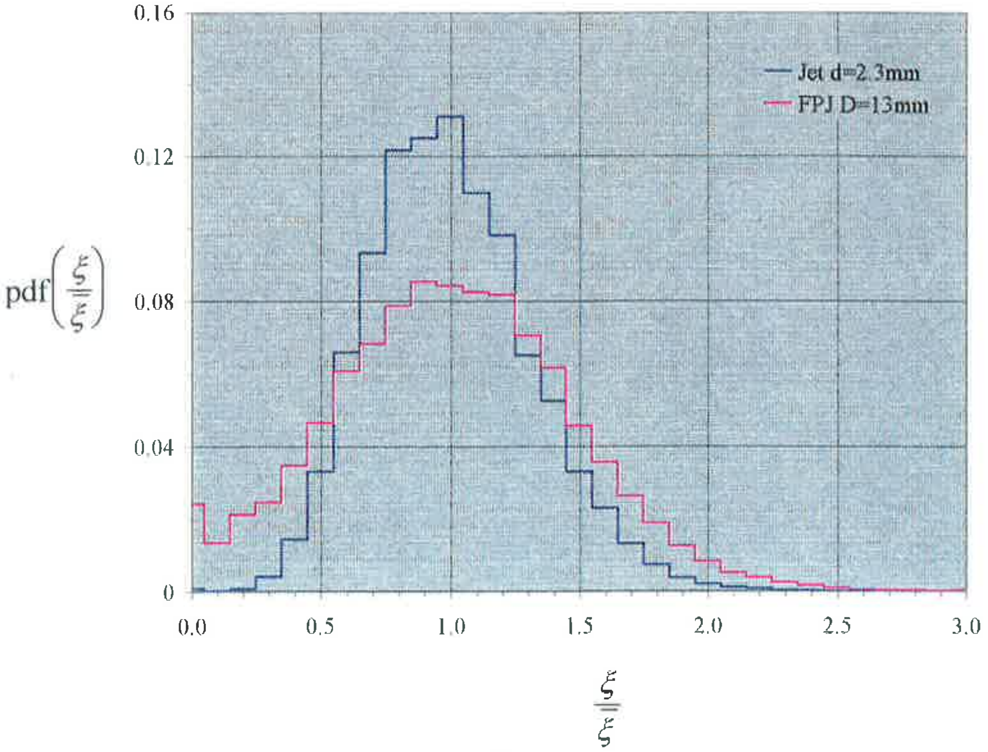

Figure 3.27 The average probability distribution function of the mean jet concentration normalised by the local mean jet concentration, $\mathrm{pdf}(\xi/\overline{\xi})$, on the jet axis, $80d \le (x-L) \le 100d$, for the simple jet flow and the FPJ flow. (Experimental conditions as for Figure 3.10 and Figure 3.17 respectively)

3.4.6. Macroscopic Mixing Length-Scales

A further test of the effect of precession introduced by the addition of the FPJ chamber to the basic orifice, on the mixing characteristics of the simple jet flow is the measurement of the characteristic macroscopic length-scales in each flow. The macroscopic mixing length-scales are derived from the correlation coefficient of the concentration fluctuations. These can be measured in one dimension along the jet centre-line, l_{xx}, or as a two-dimensional spatial macro-scale which can be measured at many locations throughout the flow fields.

The correlation coefficient, R, (Becker *et al.*, 1967) between the concentration fluctuations at the points on the jet axis, (x, y_0) and $(x + \Delta x, y_0)$, which are separated by a distance, Δx, is defined by

$$R = \frac{\overline{\xi'(x) \times \xi'(x + \Delta x)}}{\left(\overline{\xi'(x)^2}\right)^{1/2} \times \left(\overline{\xi'(x + \Delta x)^2}\right)^{1/2}}.$$

$\xi'(i,j) = \xi(i,j) - \overline{\xi(i,j)}$ is the instantaneous fluctuation of the jet concentration about the time averaged mean at a given point, (i, j). The denominator of the R calculation then represents the product of RMS fluctuation of jet concentration at each of the points. The maximum correlation occurs at the origin, where $R = 1$, and R decreases with increasing distance Δx, in both the positive and negative axial directions. A measure of the integral length-scale in the axial direction, l_{xx}, was obtained by Schefer *et al.* (1988) based on the width of the region bounded by the 50% correlation coefficient value, $R = 0.5$. Following their work, the $R = 0.5$ contour is given the notation l_{xx}, noting that this is not an absolute measure of the integral length-scale.

Calculations of l_{xx}, at points along the jet axis in steps of $\delta x = 10$mm ($\delta x \approx 4d$), are plotted for the present simple turbulent jet case in Figure 3.28. These are compared with results from Becker *et al.* (1967) and Nobes (1997). Becker *et al.* (1967) determined l_{xx} from an analysis which made use of single point measurements of the energy spectra of the jet concentration fluctuations. They showed that l_{xx} is linearly proportional to x and follows the relation $l_{xx} = 0.0445x$ for $4d \le x \le 35d$. Nobes (1997) presents results for a $d = 3.0\text{mm}$ jet from a nozzle with a smooth contraction where $l_{xx} = 0.055x$ for $0 \le x \le 80d$. This data was collected using the same experimental apparatus and analysis technique as that used for the present experiments. However, a larger database of 1200 images was collected. The present results show considerable scatter in the measured value of l_{xx}, although the trends follow both Becker *et al.* (1967) and Nobes (1997). It is plausible that the scatter in the present data is a consequence of the limited size of the data set resulting in a lack of statistical convergence. Nevertheless l_{xx} determined from $R = 0.5$ appears, on average, to be a representative measure of the axial integral length-scale. The regression line shows slightly larger l_{xx} for the simple jet from an orifice than for that from a smooth contraction, consistent with the broader spread found for the jet (Section 3.4.5)

Figure 3.29 compares l_{xx} for the simple jet flow with that for the FPJ flow. The data are presented with a common origin ($x = 0$), corresponding to the location of the jet throat, which is upstream from the imaged area for the FPJ case. It is apparent that l_{xx} is consistently greater for the FPJ flow than for the simple jet flow by a factor of 2.0 for the data presented in the region $25d \le (x - L) \le 105d$.

The macro-scale is defined by the 50% contour of the two point spatial correlation coefficient, $R = 0.5$, which can be determined in any direction (Schefer *et al.*, 1988 and Namazian *et al.*, 1992). The two point spatial correlation coefficient, R, is defined by

$$R = \frac{\overline{\xi'(x,y) \times \xi'(x+\Delta x, y+\Delta y)}}{\left(\overline{\xi'(x,y)^2}\right)^{1/2} \times \left(\overline{\xi'(x+\Delta x, y+\Delta y)^2}\right)^{1/2}}.$$

In the analysis a station (x, y) is chosen and the correlation coefficient is determined for a varying displacement (Δx, Δy) from that station to each point within an interrogation sub-window. A sufficiently large sub-window size (approximately 60×60mm) has been used to ensure that the $R = 0.5$ contour is fully resolved at each station.

Figure 3.30 and Figure 3.31 present R contour lines for the simple jet and FPJ flows respectively. Calculation of R for the simple jet and the FPJ flows has been made at numerous locations corresponding to a regular grid spacing of δx = 10mm (≈ 4d) and δy = 10mm (≈ 4d). To improve clarity only a limited number of the contour line sets are shown.

The data presented for the simple turbulent jet are entirely consistent with comparable results presented by Schefer *et al.* (1988) for a nozzle with a smooth contraction. On the jet axis the macro-scale in the present data is symmetrical and approximately equal to the nozzle exit diameter at $(x - L) \approx 8d$ (x = 20mm). Downstream the macro-scale grows linearly in size following Figure 3.28 and the approximate symmetry of the contours suggests that the turbulence at this scale is approximately isotropic on the axis. Off the jet axis, in the mixing layer, the contours are elliptically shaped and aligned perpendicular with the principle line of strain at approximately 45 °. An average aspect ratio of 1.7:1 (major axis : minor axis) is determined from measurements of the macro-scale along an axis diagonal to the flow direction. The elongation of the structures is consistent with the concept of shear generated turbulence and with observations of the ejection of jet fluid from the jet axis by large-scale structures spanning the full-width of the flow (Dimotakis *et al.*, 1983).

In the case of the FPJ, Figure 3.31, a dramatic increase in the macro-scale at any given location is evident throughout the imaged area. On the jet axis the contour is roughly symmetrical, again suggesting a measure of isotropy of the turbulence there. With increasing axial distance from the jet exit the macro-scale is seen to grow linearly, to a size that is double the simple jet macro-scale when scaled from the jet throat. Off-axis the contours are elliptical and again aligned perpendicular to the principal line of strain, however they are not as elongated as the contours in the simple turbulent jet case, with an average aspect ratio of 1.4:1 (major axis : minor axis).

These results demonstrate that macro-scales of turbulent mixing in a FPJ flow are greater than those in the simple jet flow by a factor of two. The reduced elongation of the macro-scale contours in the FPJ flow case is direct evidence that local strain rate is reduced. These observations, taken together with knowledge that the total turbulence energy across all the length-scales must be conserved, suggests that the effect of precession is to enhance large-scale mixing and suppress fine-scale mixing within the area downstream from the immediate nozzle exit.

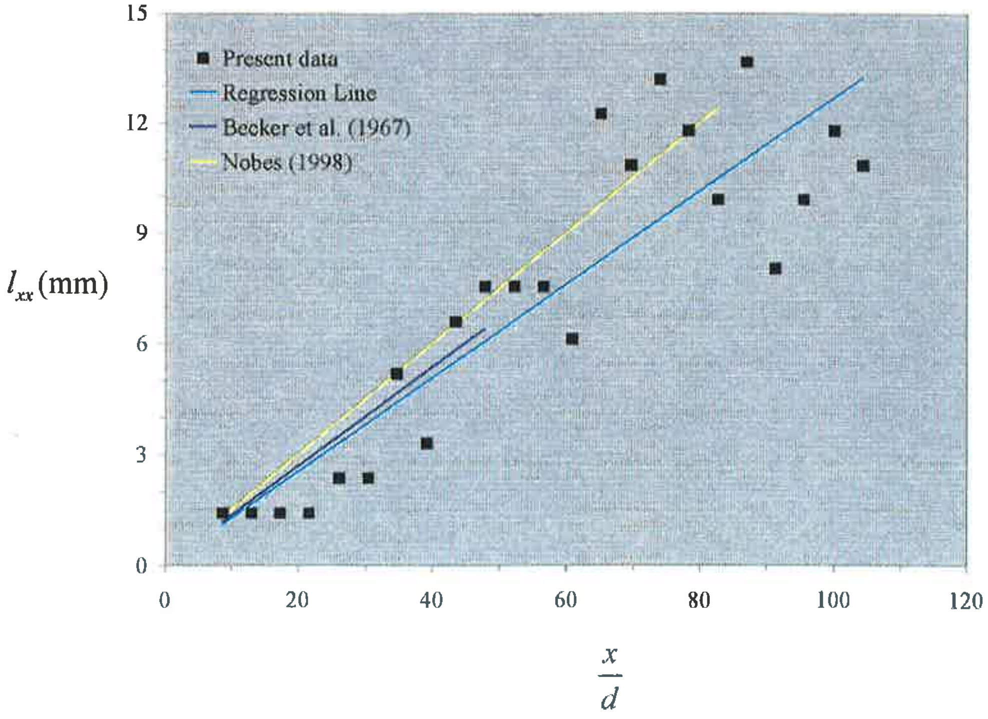

Figure 3.28 The axial integral length-scale of the concentration fluctuations, l_{xx}, on the jet axis for simple jet flows. (Experimental conditions as for Figure 3.10)

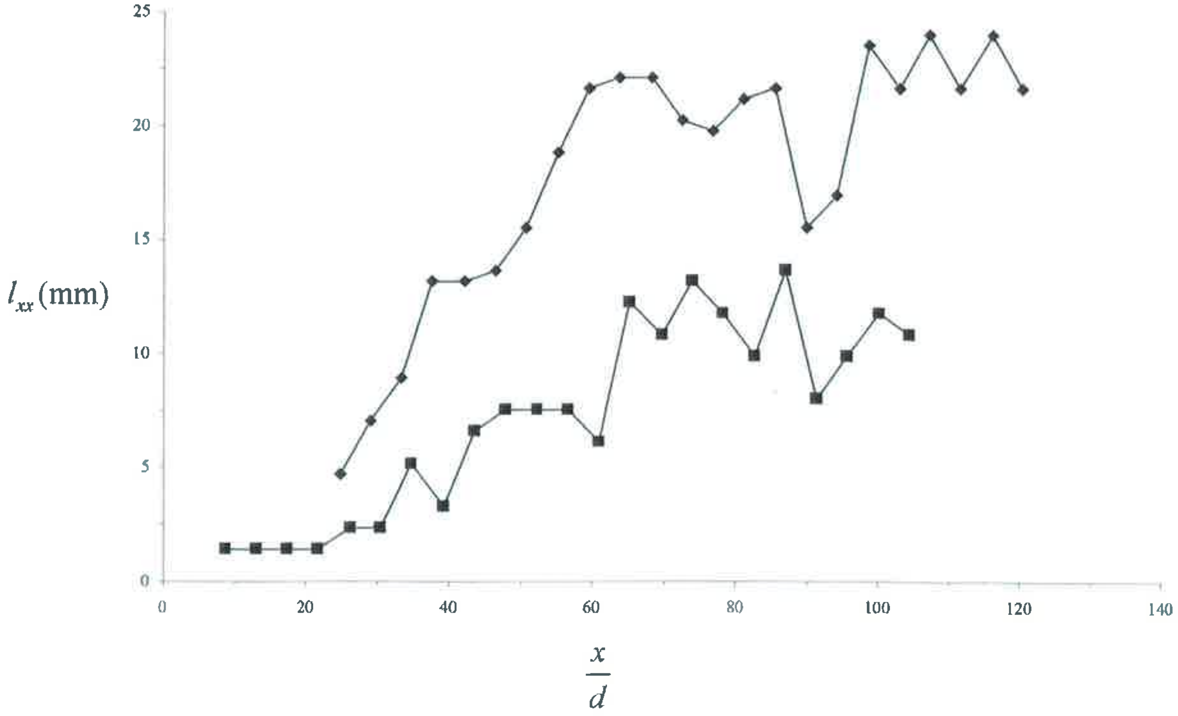

Figure 3.29 The axial integral length-scale of the concentration fluctuations, l_{xx}, for the simple jet flow (■) and the FPJ flow (◆). (Experimental conditions as for Figure 3.10 and Figure 3.17)

UNIVERSITY OF ADELAIDE LIBRARY

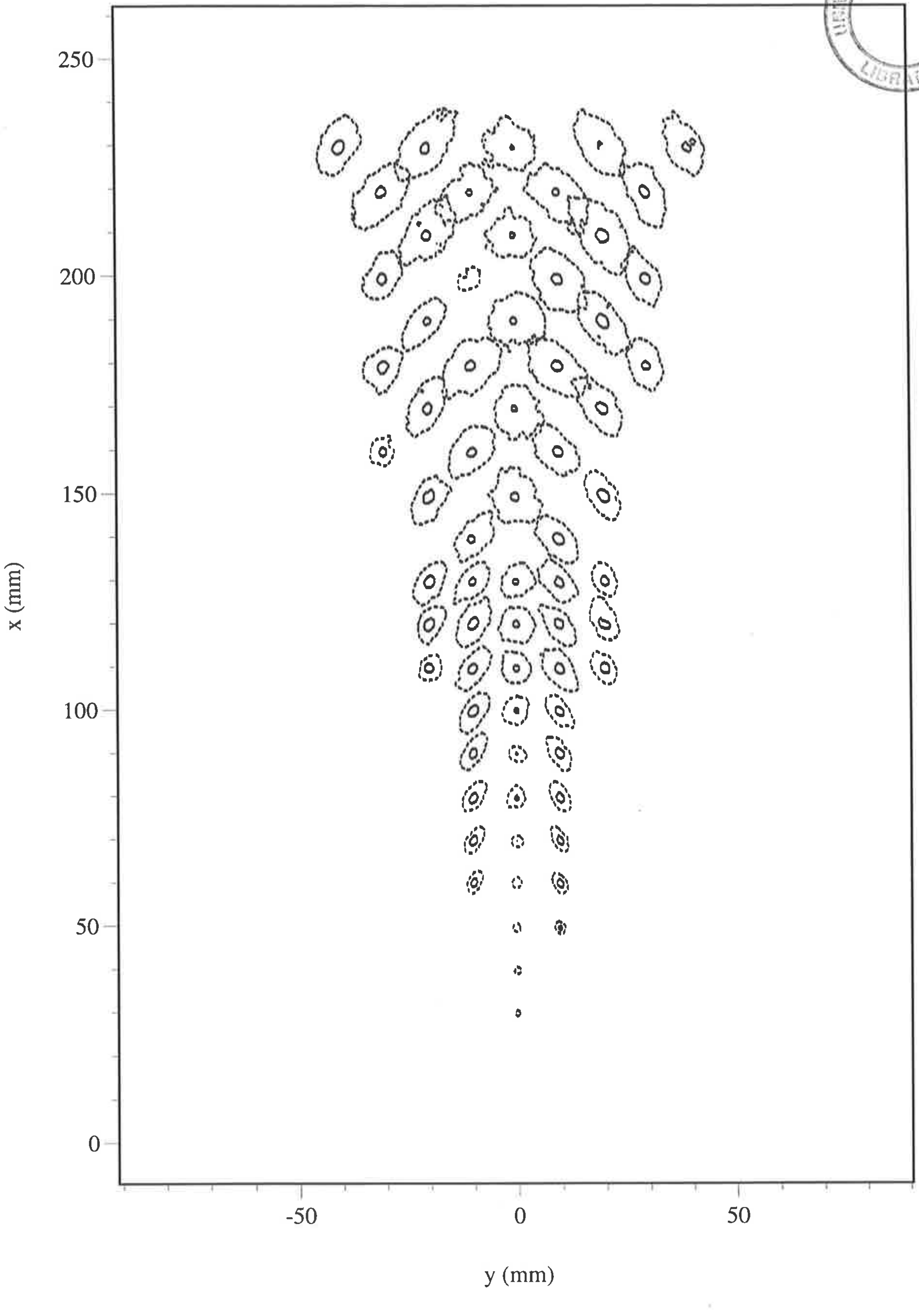

Figure 3.30 A composite image of multiple two-point spatial correlation results, R, for the simple jet flow (– – – $R_{11} = 0.50$; ——— $R_{11} = 0.75$). A limited number of contour line sets are presented for clarity. (Experimental conditions as for Figure 3.10)

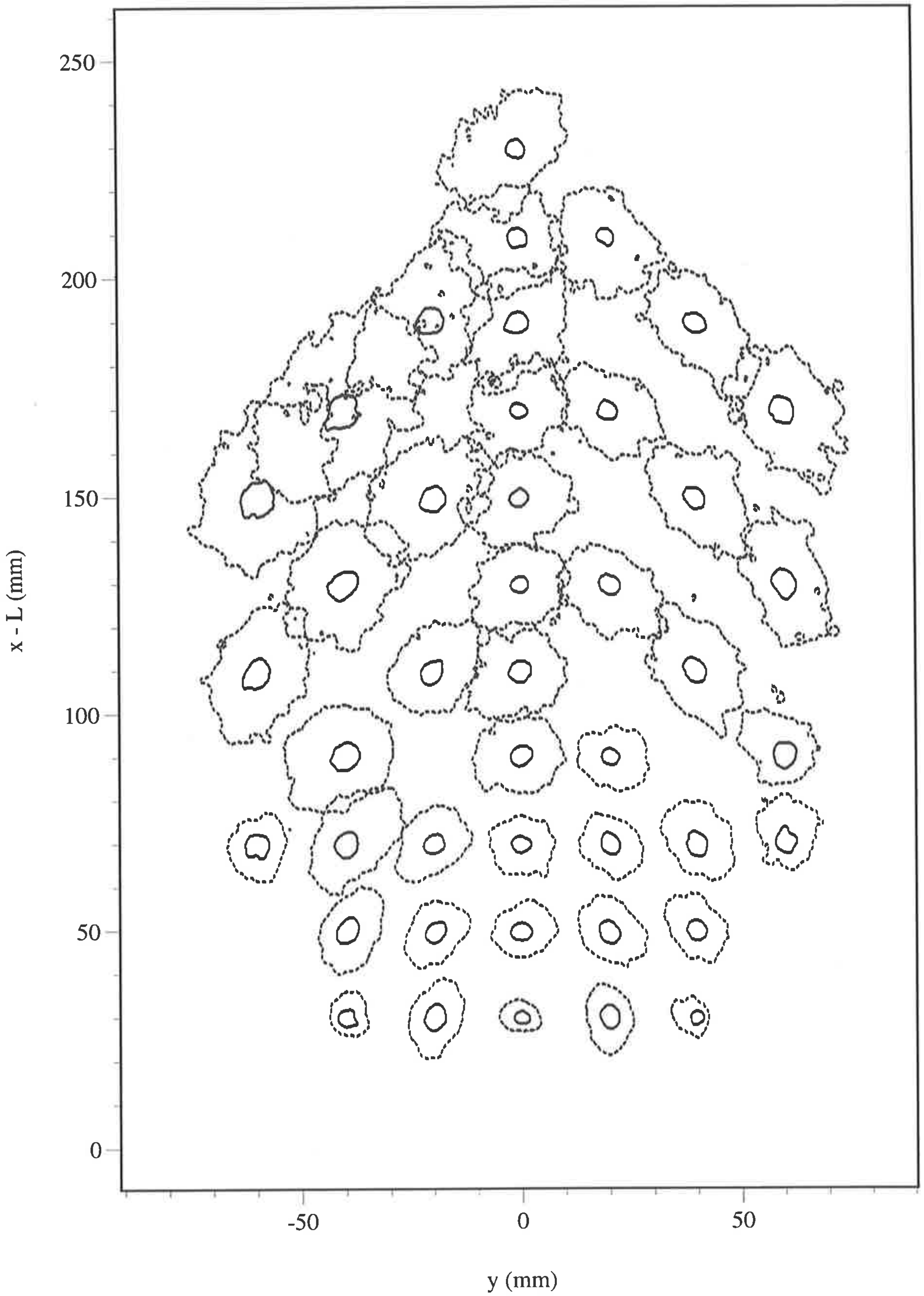

Figure 3.31 A composite image of multiple two-point spatial correlation results, R, for the FPJ flow (– – – $R_{11} = 0.50$; ——— $R_{11} = 0.75$). A limited number of contour line sets are presented for clarity. (Experimental conditions as for Figure 3.17)

3.4.7. Mixing Rate Measurements

Comparison is made between the mixing rate of the simple jet and the FPJ flows. Another measure of the mixing rate used in the present study is the scalar dissipation, χ. Schefer *et al.* (1994c) describes the scalar dissipation as "*...the rate at which concentration non-uniformities relax toward zero due to molecular diffusion. As such, it provides an important measure of the local rate of mixing at the molecular scale*".

The scalar dissipation, χ, is determined from the mixing field data that was presented in Section 3.4.2 for the simple jet flow and in Section 3.4.3 for the FPJ flow. The dissipation is usually determined from mass fraction measurements, although for the present constant density measurements, the mass fraction and the volume fraction are equal and can be used interchangeably with the jet concentration or mixture fraction, ξ. Bilger (1976) has defined χ as

$$\chi = 2\mathrm{D}\nabla^2 \xi$$

where,

$$\nabla^2 \xi = \left(\frac{\partial \xi}{\partial x}\right)^2 + \left(\frac{\partial \xi}{\partial y}\right)^2 + \left(\frac{\partial \xi}{\partial z}\right)^2$$

and D is the diffusivity of the molecular species (D = 1.5×10^{-6}m^2/s for air/air). The two dimensional ξ data can be used directly to determine the stream-wise (axial) gradient, $\partial \xi / \partial x$, and the cross-stream (radial) gradient, $\partial \xi / \partial y$. Here, partial isotropy is assumed for both the simple jet and the FPJ flows in order to determine the gradient in the out-of-plane (azimuthal) direction, that is, it is assumed that $\partial \xi / \partial y \approx \partial \xi / \partial z$. This assumption is commonly used to calculate the dissipation from planar ξ measurements in simple jets flows (Namazian *et al.*, 1988, van Cruyningen *et al.*, 1990, Schefer *et al.*, 1994a, and Feikema *et al.*, 1996). Here, the scalar gradient in each direction is determined at each point by a 3×3pixel central difference algorithm. This algorithm is based on the Roberts filter in which the gradient in a given direction at a point is weighted by 50% based on the gradient in that direction across the point and by 25% based on the gradient across adjacent parallel neighbouring points. For example $\partial \xi / \partial x$ is determined at the point (x,y) by

$$\frac{\partial \xi}{\partial x} = \tfrac{1}{8}\left[\xi(x+1, y+1) - \xi(x-1, y+1)\right] + \tfrac{1}{4}\left[\xi(x+1, y) - \xi(x-1, y)\right] + \tfrac{1}{8}\left[\xi(x+1, y-1) - \xi(x-1, y-1)\right].$$

Namazian *et al.* (1988) calculate $\partial \xi / \partial x$ from the gradient between (x,y) and a neighbouring pixel (x + 1, y), while Feikema *et al.* (1996) use a 5×5pixel central difference algorithm, so that the present choice represents a reasonable compromise between smoothing the gradient and suppressing noise present in the ξ measurements. The spatial resolution of the measure of χ is therefore three times that of ξ. Thus, relative to the Batchelor length-scale, χ can not be fully resolved in the imaged region (Section 2.2.3).

Three representative examples of the instantaneous χ field for the simple jet flow in the region $0 \le x \le 110d$ are shown in Figure 3.32. These examples correspond to the three planar ξ images that are shown in Figure 3.10. The images are displayed with a false colour map for a logarithmic χ scale. This presentation scheme enables the wide range of χ values to be displayed in a single image. Van Cruyningen *et al.* (1990) have determined an approximation to the scalar dissipation, which includes only the gradient terms in the calculation, from planar ξ data for a simple turbulent jet in the region $0 \le x \le 45d$. Their results show qualitative similarity to the present images.

The region of highest χ values is located in the shear layer adjacent to the potential core of the simple jet flow. The dissipation magnitude progressively decreases in the stream-wise direction. This is consistent with the decrease in local ξ values and the increase in the large-scale structure in the flow with increasing axial distance, which were demonstrated in Section 3.4.2 and Section 3.4.5 respectively. The local peak scalar dissipation is confined to thin layers which extend from the edge of the jet toward the jet axis and are aligned at approximately 45°, from a visual estimate. The alignment of the layers is parallel to the principal line of strain in the jet flow. This is consistent with the angle of the major axis in the macroscopic length-scales determined from the two-point spatial correlation in Figure 3.30. These layers appear to be associated with large-scale structures. Locally high χ layers mark the upstream edge of the structures, which is a consequence of the outward (radial) protrusions of jet fluid from the jet core. Schefer *et al.* (1994c) have investigated the jet concentration field associated with large-scale structures and show that local high χ layers exist along the outer edge of the structures.

Three representative examples of the instantaneous χ field in the FPJ flow are shown in Figure 3.33, each frame of which corresponds to the equivalent ξ images shown in Figure 3.17. The images are displayed with the same presentation scheme as used for the simple jet case. This allows direct comparison of magnitudes of the χ values. The underlying structure of the turbulence is clearly very different from that of the simple jet. The lines of peak dissipation are distributed differently in the flow.

Layers of fluid with high χ are seen in the region adjacent to the exit of the FPJ nozzle where the light sheet cuts through the emerging jet as it is directed instantaneously out of the image plane. Elsewhere layers of high χ are present at the jet-fluid/ambient-fluid interface. Islands of "jet" fluid at the edge of the FPJ flow and islands of "ambient" fluid in the core of the FPJ flow are visible. The presence of these islands is consistent with the decreased centre-line decay of ξ (Section 3.4.3) and a broader distribution of the ξ values (Section 3.4.5).

The mean values of χ on the jet centre-line are shown in Figure 3.34 for the simple jet and FPJ flows. The data are presented with a common origin ($x = 0$), corresponding to the location of the jet throat. It is apparent that there are generally more layers having high values of scalar dissipation in the FPJ flow than in the simple jet flow. It can also be observed that the values of peak instantaneous χ throughout the FPJ dissipation field tend to be greater than in the simple jet flow at the corresponding axial locations. True scalar dissipation occurs at the molecular scale. While the present technique is not capable of resolving down to the Batchelor length-scale in the near field, the layers of high χ appear to be genuinely associated with molecular processes. Thus the increased number of layers of high χ fluid in the FPJ flow suggests that precession of a jet acts to decrease mixing of jet fluid that would occur by straining of the flow field and to increase the importance of molecular diffusion across interfaces between fluid regions of different concentrations that have been "folded" together. These findings support the concept that the effect of precession is to change the underlying structure of turbulent mixing in a manner that augments large-scale engulfment and suppresses fine-scale turbulent mixing.

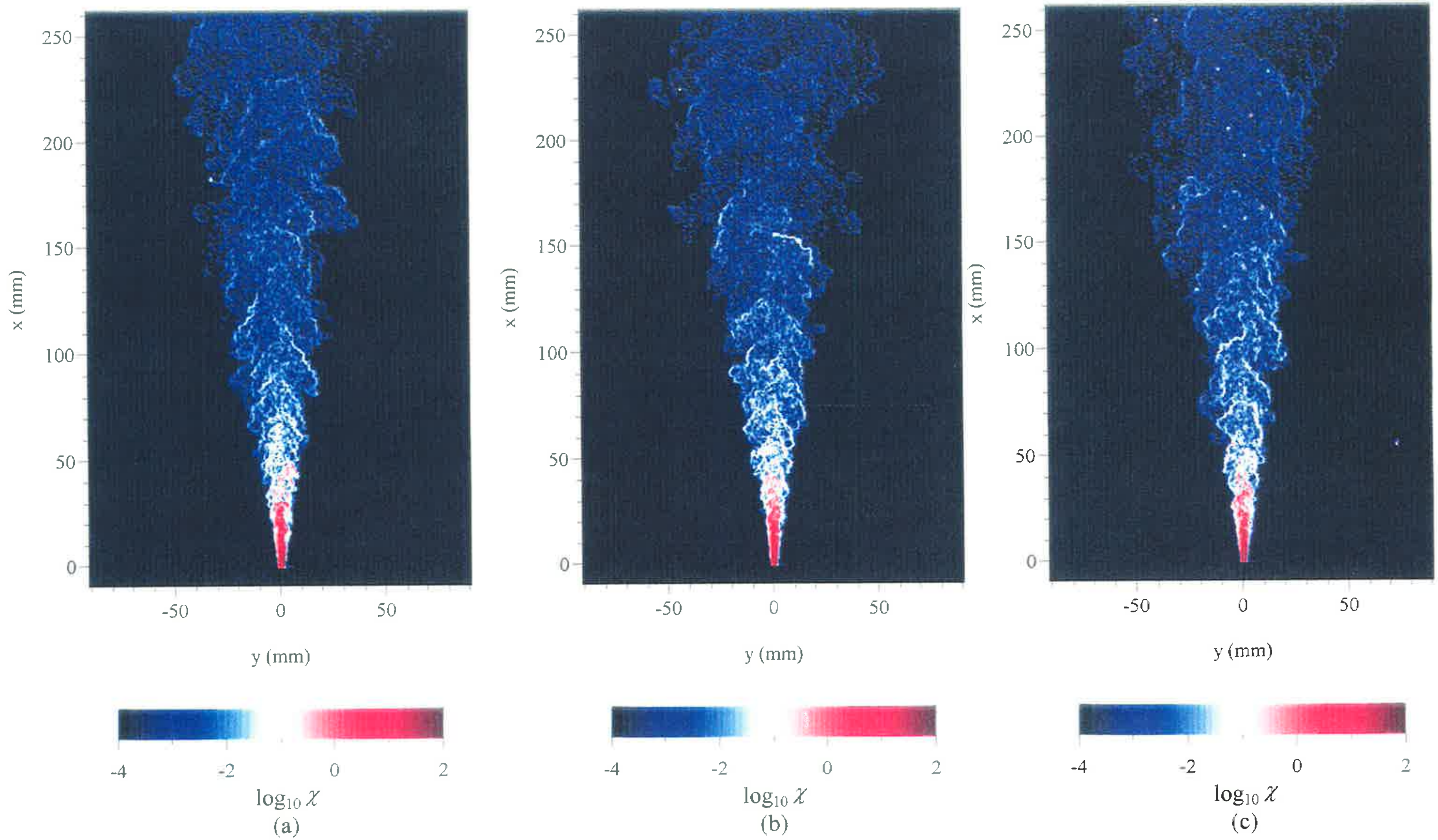

Figure 3.32 Instantaneous images of scalar dissipation field, χ, for the simple jet flow. (Experimental conditions as for Figure 3.10)

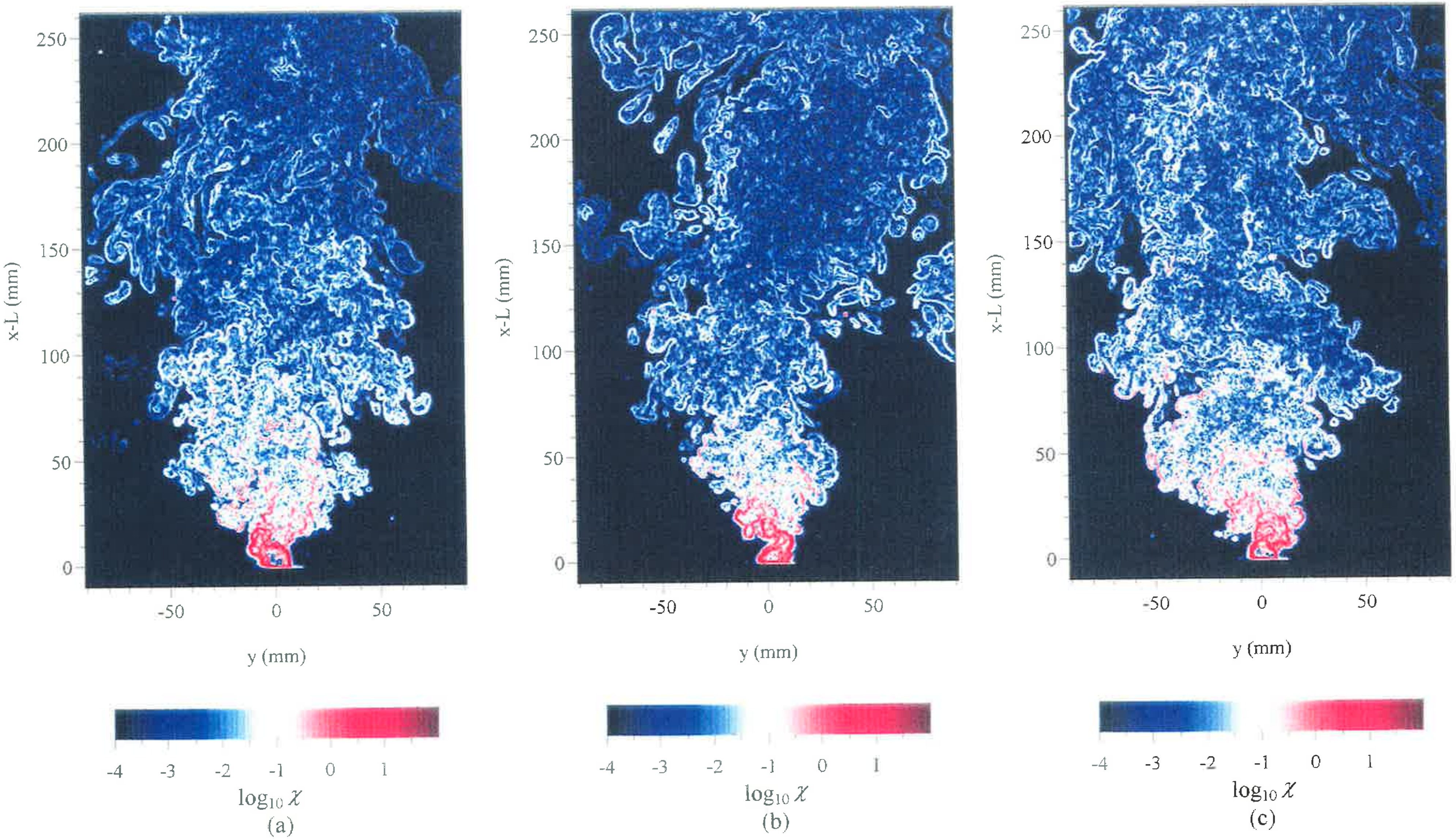

(a)

(b)

(c)

Figure 3.33 Instantaneous images of scalar dissipation field, χ, for the FPJ flow. (Experimental conditions as for Figure 3.17)

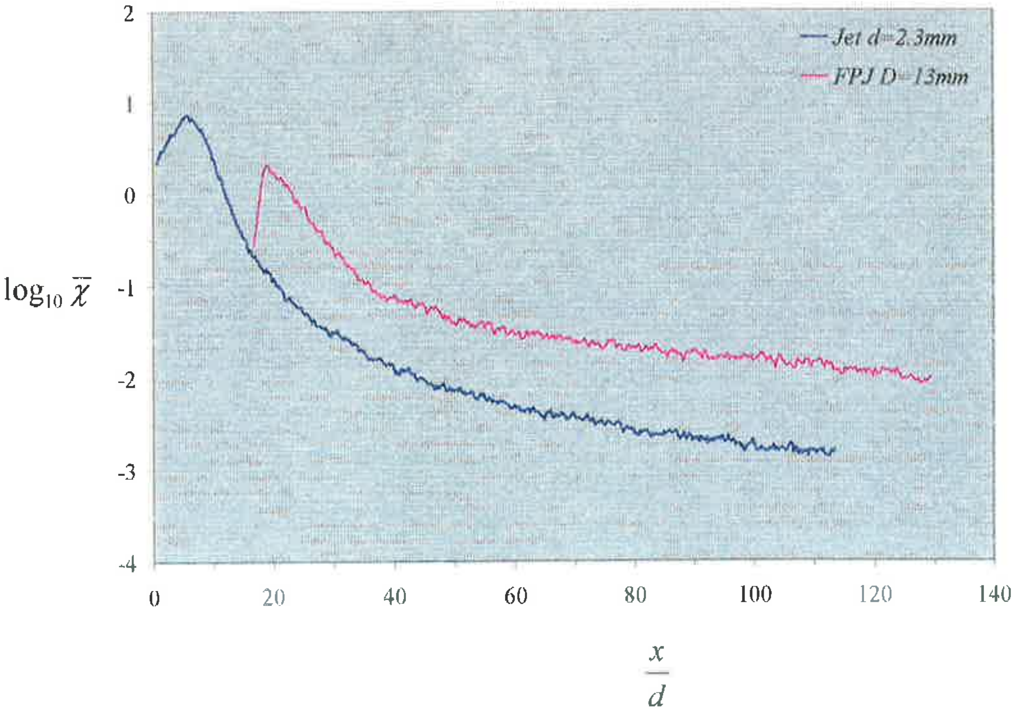

Figure 3.34 Mean scalar dissipation, $\overline{\chi}$, on the jet axis for the simple jet flow and the FPJ flow. (Experimental conditions as for Figure 3.10 and Figure 3.17)

3.5. Summary of the Non-Reacting Flow Investigations

Chapter 3 has presented qualitative and quantitative experimental data that characterise the effect of precession on the mixing of the simple turbulent jet flow with its surrounding ambient fluid. Precession in this jet is induced by the fluid mechanical instability generated by the FPJ nozzle. Direct comparison with the simple jet flow is possible because precession is achieved solely by the addition of the chamber section downstream from the jet throat. Changes to jet mixing downstream from the nozzle have been assessed from new experimental results by planar flow visualisations, planar velocity measurements and quantitative planar jet concentration measurements.

Flow visualisation has been used to characterise the gross flow motions of the simple jet issuing from the circular orifice. Precession of this jet is generated by the addition of the chamber section downstream from the jet throat. The chamber length is $L \approx 16d_1$. Flow visualisation of the FPJ flow in the region $0 \leq (x - L) \leq 27d_1$ has demonstrated the generation of larger scale flow structures that are responsible for entrainment of significant ambient fluid. Velocity measurements demonstrate that there is a dramatic reduction in the flow velocities in the region downstream from the nozzle, by two orders of magnitude relative to that of the jet throat.

Jet concentration statistics for the region $0 \leq x \leq 110d$ are used to characterise the simple jet flow issuing from the circular orifice (without the addition of the FPJ chamber section). These data have been compared with published statistics for a jet flow from a nozzle with a smooth contraction. The results show that the present jet, issuing from a sharp edged orifice plate, is characterised by:

- symmetry in the mean and RMS jet concentration about the jet axis, and linear relationships of the mean parameters with axial distance, as found by others,
- a potential core which extends along the jet axis to $x \approx 3d$,

- an increased rate of decay of the mean jet concentration along the jet axis by a factor of approximately two compared with the jet issuing from the smooth contraction nozzle investigated by Becker *et al.* (1967),
- an asymptotic half-width spreading angle of 6.6°, compared with 6.0° by Becker *et al.* (1967),
- radial mean and RMS jet concentration profiles that are consistent with a marginally wider spreading angle when compared with Becker *et al.* (1967),
- self-similarity of the radial mean jet concentration for $x \geq 20d$,
- self-similarity of the radial RMS jet concentration for $x \geq 80d$, and
- an increase in the asymtotic unmixedness value $\xi_{RMS} = 0.3\overline{\xi}$ on the jet axis compared with $\xi_{RMS} = 0.22\overline{\xi}$ found by Becker *et al.* (1967).

These characteristics demonstrate that the mixing processes throughout a jet produced by a sharp edged orifice are different from those generated by a nozzle with a smooth contraction.

The effect of precession on the scalar mixing field of the simple jet is significant. Precession of this jet is generated by the FPJ nozzle with a chamber length $L = 16d_1$. Jet concentration statistics presented for $0 \leq (x - L) \leq 110d_1$ show that the effect of precession on mixing, relative to the simple jet flow is to:

- increase the mean jet concentration along the jet axis by a factor of 2 (ie. half the centre-line decay rate),
- increase the half-width spreading angle from 6.6° to 11°,
- increase the distance required to achieve self-similarity of the radial mean jet concentration to $(x - L) \approx 40d_1$,
- increase the distance required to achieve self-similarity of the radial RMS jet concentration so that full similarity is not reached in the imaged region $(x - L) \leq 110d_1$,
- increase the unmixedness everywhere along the jet axis by about 50%,

- broaden the distribution of mixed fluid concentrations that can exist on the jet axis,
- increase the intermittency on the jet axis demonstrating the existence of "pure" ambient fluid along the axis,
- increase the macroscopic mixing length-scales, so that the axial integral length-scale of the concentration fluctuations is increased by a factor of 2.0, and
- increase the scalar mixing rate on the jet axis by an order of magnitude.

These findings demonstrate conclusively that the effect of precession is to change the underlying structure of the turbulence in a manner that suppresses fine-scale mixing and enhance large-scale engulfment of ambient fluid. Precession also reduces the role of the local strain rate in the flow.

Chapter 4

4. Flame Stabilisation in Precessing Jet Flames

4.1. Introduction

Stabilisation characteristics of fluidic precessing jet (FPJ) flames is addressed in the present chapter and both qualitative and quantitative experimental data are documented. FPJ flames are investigated for burners that have an optimal geometry for reliable precession (Hill *et al.*, 1992) and are geometrically similar to the commercial burner configuration (Rapson *et al.*, 1995). Mixing and combustion characteristics have been determined from visualisation of the flame envelope (Section 2.3.1), reaction zone imaging (Section 2.3.2) and non-reacting jet concentration measurements (Section 2.2.3). These techniques are used to resolve gross fluid motions in the flame (Section 4.2), the structure of the reaction zone (Section 4.3) and indicative jet concentration statistics in the flame stabilisation region (Section 4.4). Reference is made to numerous experimental results found in the literature on turbulent jet diffusion flames. The role of mixing and combustion characteristics in various stabilisation mechanisms that have been proposed for jet flames is broadly considered in relation to FPJ flame stabilisation (Section 4.5).

4.2. The Role of Large-Scale Structures in Precessing Jet Flames

4.2.1. Experimental Arrangement

Visible observations and imaging are made of the luminescent flame envelope of unconfined frames from a vertical FPJ nozzle firing commercial grade propane. A variety of FPJ flames are investigated from nozzles with chamber diameters of $D = 13\text{mm}$ and $D = 21\text{mm}$, with upstream throat diameters of $d_1 = 2.3\text{mm}$ and $d_1 = 4.4\text{mm}$ respectively. Reynolds numbers of $\text{Re}_{d_1} > 20{,}000$, based on flow variables at the upstream throat, are sufficiently high to ensure that the precession will occur reliably.

The flow visualisation has been recorded by a standard 16mm movie camera and a high-speed camera described in Section 2.3.1. The framing rate is sufficiently fast to capture large-scale dynamic motions in FPJ flames.

4.2.2. Images of the Visible Flame Envelope

A single image of a 44kW FPJ flame of commercial grade propane issuing from the $D = 13$mm FPJ burner, taken from a movie sequence discussed later, is shown in Figure 4.1. The edge of the flame is well resolved everywhere except near to the base of the flame, which is pale blue, consistent with the poorer response of the film to blue than to orange colours. Visual observation of that region and the photographic measurements that better highlight the blue tones in the flames from Nathan *et al.* (1996), suggest that the true lift-off height is less than the 50-100mm suggested by Figure 4.1. The data of Nathan *et al.* (1996), using the mechanical precessing jet (MPJ) burner nozzle, showed a reduction in the lift-off height of a flame by a factor of between five and ten relative to a jet diffusion flame.

Further down-stream from the initial blue region the entire flame envelope is dominated by visible radiation from incandescent soot, allowing a distinct definition of the visible flame boundary which is well resolved by the present technique. All of the soot produced is consumed before the flame tip. The maximum flame width, about 250mm, occurs close to the nozzle, such that the initial conical spread angle of the jet is in excess of 80°. The instantaneous flame length in this image is 790mm, giving a length to maximum diameter ratio of 3.2 which agrees well with the value of 3.1 measured by Nathan *et al.* (1996). Those authors used a long exposure photographic technique to observe high Strouhal number methane and propane flames generated by the MPJ nozzle.

As the flow rate is increased the general character of the FPJ flame shows no change up to the maximum supply pressure available ($\approx$150kPa). It is not possible to blow the flame off under these conditions, a result consistent with results found by Nathan and Luxton (1991c) who were able to operate the FPJ burner with 800kPa supply pressure firing natural gas.

Figure 4.2 shows a series of 20 frames from an 8s sequence filmed at 64 frames per second of which Figure 4.1 is the first. Analysis of the entire 8s sequence gives an average flame length of 850mm and an average apparent lift-off height of 40mm.

By comparing successive images in the sequence, observations of the flame tip can be made. The flame length is found to fluctuate periodically with time in such a manner that the reductions in length are much more rapid than the increases in length, similar to the trends found by Mungal *et al.* (1991) for simple jet diffusion flames. Near to the tip of the flame a large bulbous region, spanning nearly half the flame length, is seen to burn out in a short time interval. The stream-wise length-scale of this region, from the flame tip to the upstream edge of the structure where the flame necks in, is approximately equal to the span-wise scale of the flame. There is strong similarity between the present oscillations and the "puffing" oscillations observed by Zukoski *et al.* (1980) in pool fires, and their terminology describing flame "puffs" has been adopted here. However the present large-scale structures are significantly different from those observed in momentum dominated jet flames, which typically have about 8 visible structures at any instant in time (Mungal *et al.*, 1991) instead of the 2-3 observed here.

Broadwell *et al.* (1984) have proposed a model for flame blowout in jet diffusion flames in which the mixing and entrainment characteristics of large-scale structures are the physical mechanism responsible for flame stabilisation. These structures are investigated in the present chapter.

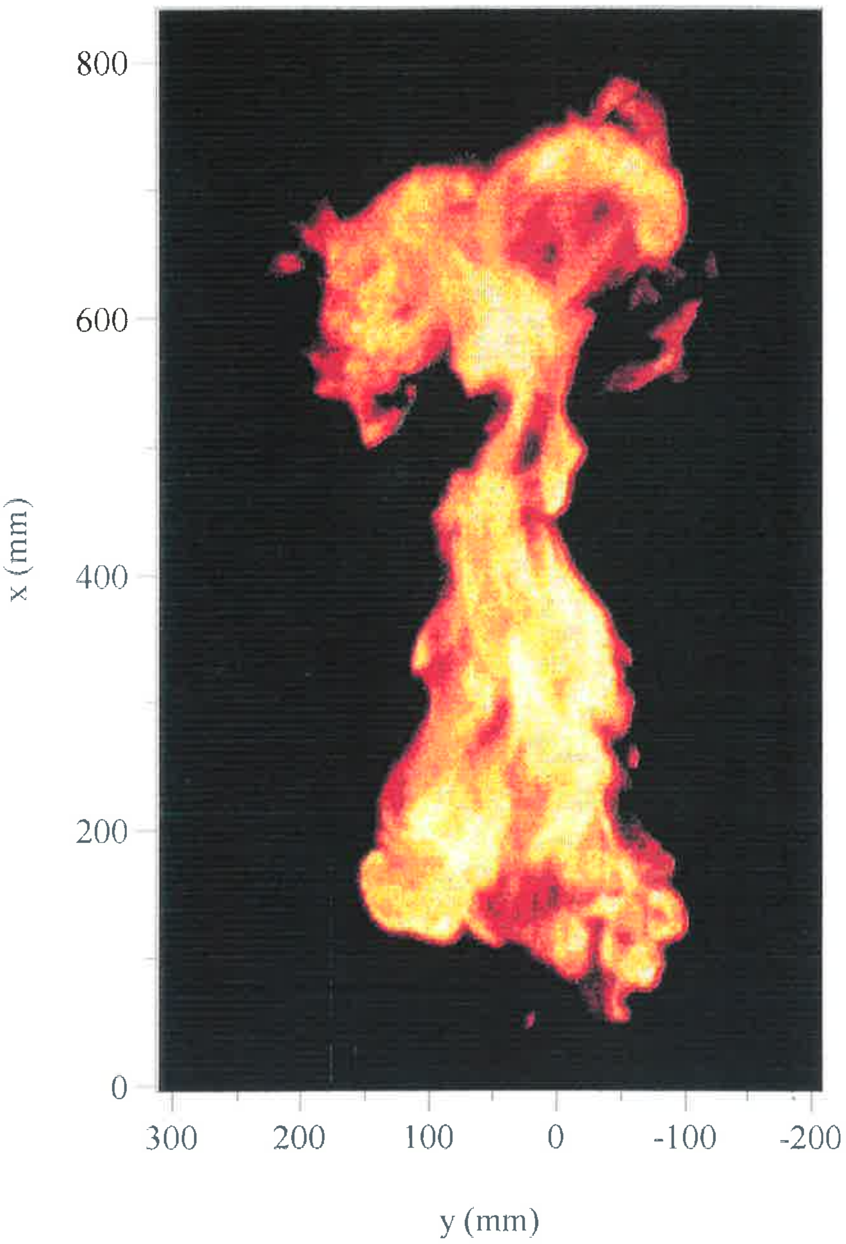

Figure 4.1 Photographic image of a vertically fired unconfined FPJ flame firing commercial propane using a standard 16mm movie camera. ($d_1 = 4.4\text{mm}$, $D = 21\text{mm}$, $\text{Re}_{d_1} = 70{,}800$, $Q = 44.1\text{kW}$, Exposure = 1/120s, Aperture = *f*/11)

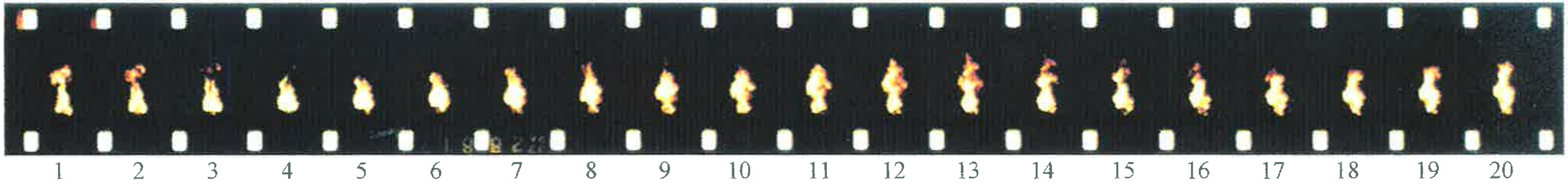

Figure 4.2 Temporal sequence of 20 movie frames of a vertically fired unconfined FPJ flame, of which Figure 4.1 is the first image. Time increases from left to right. (Experimental conditions as for Figure 4.1, Exposure = 1/120s, Framing Rate = 64 frames per second)

4.2.3. Measurements of Flame Length-Scales

Short image sequences of commercial propane flames from $D = 13\,\text{mm}$ and $D = 21\,\text{mm}$ FPJ nozzles have been recorded with the high-speed video at a framing rate of 250 frames per second (Table 4.1). From each of these sequences a temporal series of images has been selected and stored on a PC for further image processing, and on conventional video for further visual analysis. Each series consists of 200 individual images, with every fourth image selected from the recorded sequence so that images are spaced 16ms apart. Thus a total of 3.2s of real time is captured for each flame. Images have been processed to determine the flame length and to highlight the dynamic motions of the puff structures that propagate through it. One representative example of a flame from each burner has been chosen for illustration. A sample of 30 frames from a single flame run for each of the $D = 13\,\text{mm}$ and $D = 21\,\text{mm}$ burners is shown in Figures 4.3(a) and (b) respectively. Alternative views of these same images are presented in Figures 4.4(a) and (b) respectively. A perspective is created in which the (x,y) images have been stacked along the time axis (t), and projected back into the page.

The dynamic motion of the structures is clearly evident when the images are presented so that the edges of the flame line up, as in Figure 4.4. Each structure is seen to form near to the base of the flame and to move downstream. As the structure moves away from the near nozzle region a new structure is seen to form behind it. At the flame tip the final structure is seen to burn out in a fragmentary fashion.

Following the work of Zukoski *et al.* (1984) we can obtain quantitative information about the dynamic motions of large-scale structures in the flame from the image sequences. Here we measure the instantaneous flame length, X, the average flame length, $\overline{X}$, the height of the fluctuating region, ΔX, the average puffing frequency, f, and, further, the celerity with which a puff structure rises, S, and the global residence time, τ_G. The measured parameters are shown in Table 4.1 for each of the flames investigated.

In an image the edge of the flame is determined to be where pixel values are above a threshold that is 10% of the brightest point in the image, which is satisfactory due to the sharp flame edge in the image. The instantaneous flame length has been determined for each image in the series and subsequently the mean flame length, $\overline{X}$, has been calculated from this set of values (Table 4.1). The height of the fluctuating region as a measure of the length-scale of the final structure, $\Delta X/\overline{X}$, has been determined from intermittency length data, I, derived from the flame length data. Here I is the proportion of time that the flame tip is higher than that of a particular axial location ($0 \leq I \leq 1$). The value of ΔX has then been found from a linear extrapolation of a regression line fitted to the intermittency length data to determine the $\mathrm{I} = 0$ and $\mathrm{I} = 1$ axis intercepts. It is found that $\Delta X_{AVE} = 0.35\overline{X}$ for the $D = 13\,\mathrm{mm}$ FPJ burner and $\Delta X_{AVE} = 0.42\overline{X}$ for the $D = 21\,\mathrm{mm}$ FPJ burner. These values hold for the full range of heat outputs, consistent with trends in pool fires (Zukoski *et al.*, 1984), and coincide closely with the value found for buoyant fires from small burners at high heat outputs ($\Delta X_{AVE} = 0.42\overline{X}$ for a 0.10m diameter pool fire). By contrast, Mungal *et al.* (1991) has shown histograms of the flame length for momentum driven free turbulent jet flames in which the fluctuating region appears to only be about 30% of the average flame length. This result suggests that FPJ flames are buoyancy dominated and this is further investigated.

The puffing frequency, f, has been determined from observations of the sequences (Table 4.1). For a given burner diameter f is not constant across the range of heat outputs, unlike trends found for pool fires. Data for unconfined pool fires show a single dominant puffing frequency for a given burner diameter, regardless of fuel type (Weckman and Sobiesiak, 1988 and Cetegen and Ahmed, 1993). However the puffing frequency is known to be highly dependent upon initial conditions from these studies, such as physical disturbances obstructing airflow to the base of the flame.

Burner Diameter D (mm)	Flame Output Q (kW)	Reynolds Number Re_{d_1}	Flame Length $\overline{X}$ (m)	Fluctuation Length $\Delta X/\overline{X}$	Puffing Frequency f (Hz)	Puff Celerity S (m/s)	Residence Time $\tau_G = \overline{X}/S$ (ms)	$S/(0.4g\overline{X})^{\frac{1}{2}}$
13	28.3	45 400	0.73	0.40	5.8	1.3	560	0.76
-	45.7	73 300	0.84	0.34	6.0	1.6	530	0.88
-	62.	100 000	0.92	0.28	7.1	1.6	580	0.84
-	87.8	140 900	1.01	0.35	7.1	1.9	530	0.95
21	32.5	27 300	0.72	0.39	7.5	1.6	450	0.95
-	45.3	38 000	0.79	0.39	7.7	1.7	460	0.96
-	58.8	49 400	0.87	0.46	6.3	2.0	430	1.08
-	73.3	61 400	0.89	0.40	6.8	2.3	390	1.23
-	88.5	74 200	0.93	0.47	5.7	2.2	420	1.15
-	104.4	87 600	0.98	0.49	5.5	1.8	540	0.92
-	121.0	101 500	1.01	0.42	5.8	2.1	480	1.05

Table 4.1 The experimental conditions under which flames have been investigated and the results of measurements obtained.

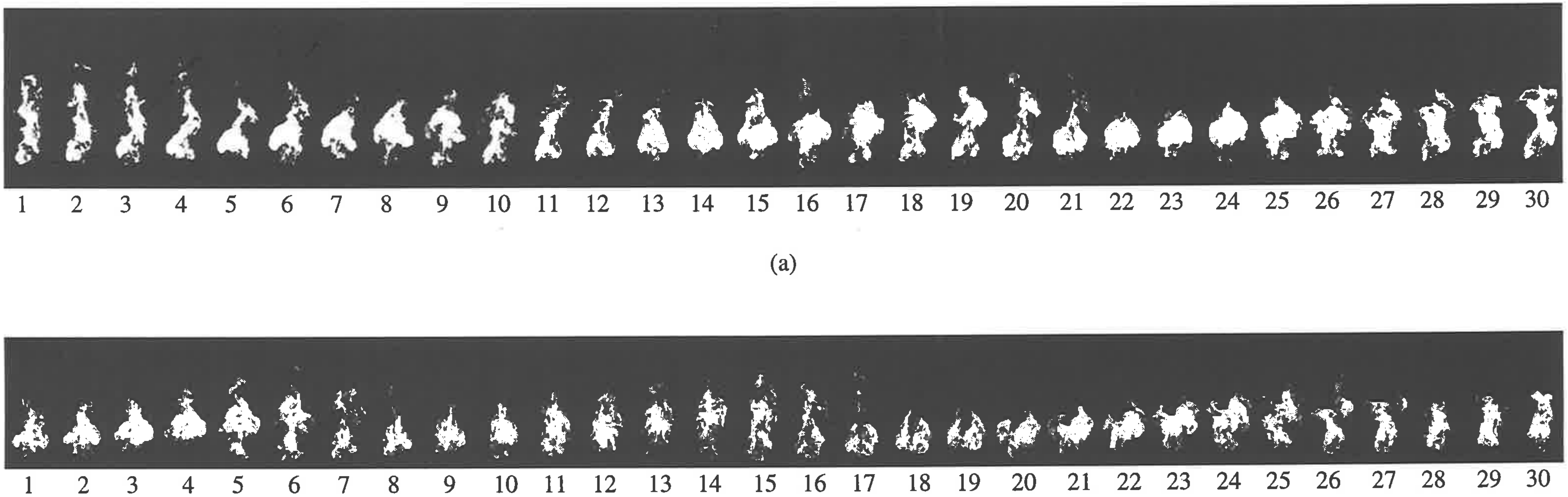

(a)

(b)

Figure 4.3 Temporal sequence of 30 image frames of vertically fired unconfined FPJ flames using a high speed digital video camera. Time increases from left to right. (a) $d_1 = 2.3\text{mm}$, $D = 13\text{mm}$, $\text{Re}_{d_1} = 73{,}300$ and $Q = 45.7\text{kW}$, and (b) $d_1 = 4.4\text{mm}$ $D = 21\text{mm}$, $\text{Re}_{d_1} = 87{,}600$ and $Q = 104.4\text{kW}$. (Fuel = commercial grade propane, Exposure = 1/250s, Aperture = *f*/4, Framing Rate = 250 frames per second)

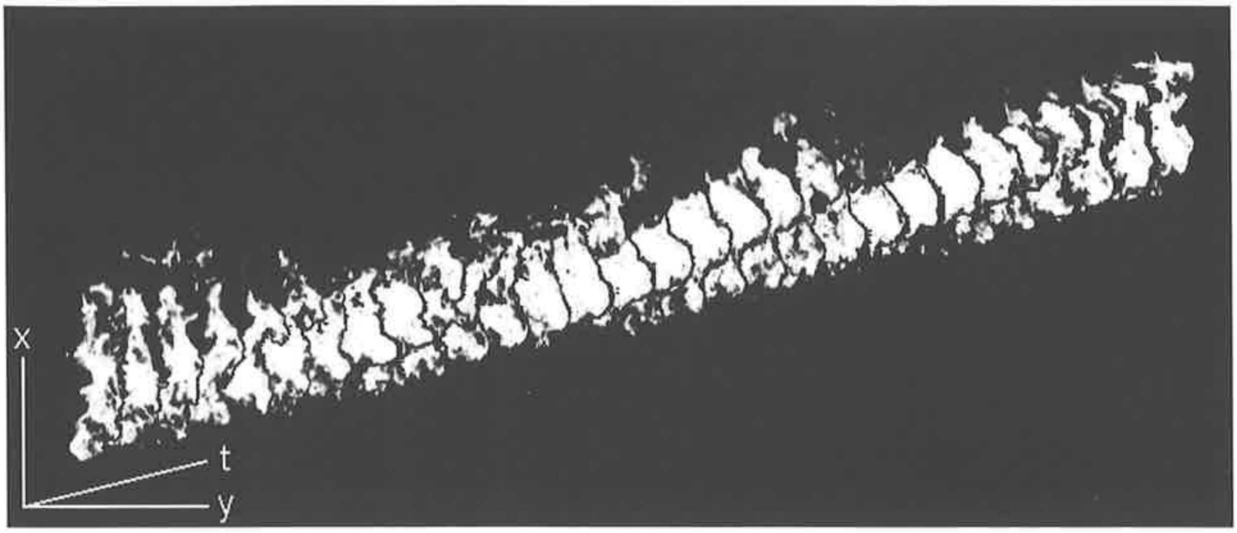

(a)

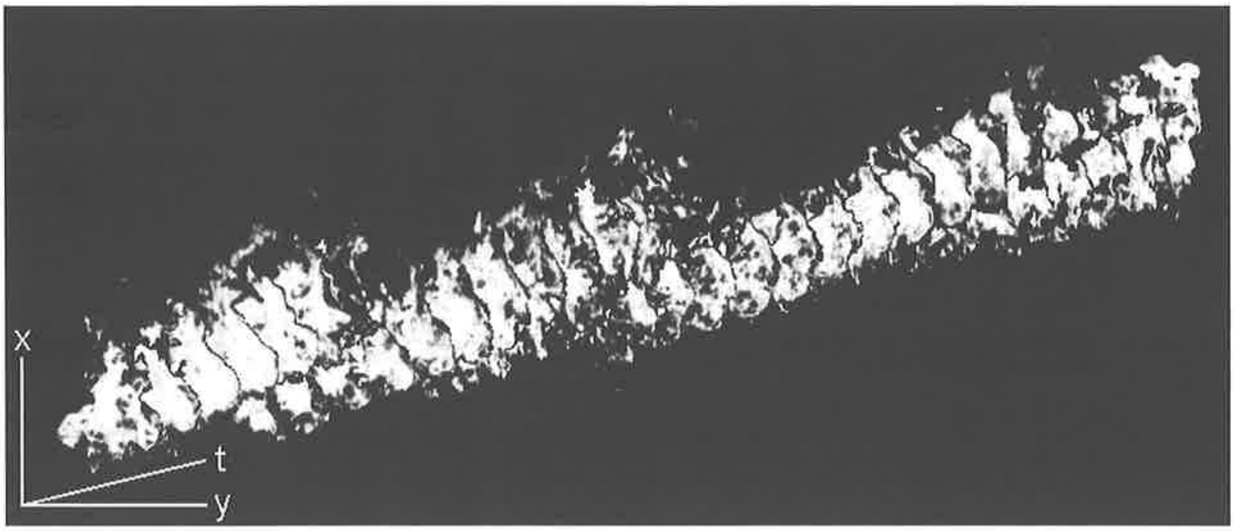

(b)

Figure 4.4 Alternative presentation of the images in Figure 4.3 with the time axis projected into the page. (Experimental conditions as for Figure 4.3)

4.2.4. Measurements of the Large-Scale Structure Celerities

Greater insight can be gained by further image processing of the large number of images to transform them into a single three-dimensional data set. The two dimensional (*x*-*y*) images from the movie sequence can be projected into the third dimension by stacking the temporal sequence along the third axis (*t*).

Computer graphic volume rendering techniques can be used as a means of displaying large quantitative scalar data sets of three-dimensional fields such as density, temperature or mixed fluid concentration. A surface of interest is extracted from the data set and the virtual solid object is rendered to produce a life-like view. A perspective and lighting are chosen that emphasise details of the data set which are not readily seen in the original data set, or to emphasise correlations in temporal sequences. Van Cruyningen *et al.* (1989) have applied this technique to concentration measurements in a horizontal buoyant jet to highlight the geometric azimuthal modes of flow. Instantaneous three dimensional iso-concentration surfaces from a simple turbulent jet have been used to deduce the jet structure and modal topology (Yoda *et al.*, 1994). Yoda and Hesselink (1990) have highlighted small-scale structures in the outer surface of the leading edge vortices shed from a delta wing. Mungal *et al.* (1991 and 1992) and van Cruyningen *et al.* (1991) have used the volume rendering technique to show *temporal correlations* in video sequences of jets and jet flames, such as the passage of large-scale structures.

The surface extracted here is the temporal evolution of the outer edge of the visible flame, with small artefacts removed. The edge of the flame in a given image is determined to be where pixel values are above a threshold that is 10% of the brightest point in the image, which is satisfactory due to the sharp flame edge in the image. A continuous surface is then generated which encloses the *x*-*y*-*t* volume representing the temporal evolution of the outer edge of the flame. The surface is composed of a series of triangular mesh faces, which interconnect neighbouring surface points. A rendering is generated by suitable illumination of the surface to highlight geometrical features of the volume by providing good depth cues to its surface. Protrusions, where the flame edge bulges out due to large-scale structures, produce ridges in the surface of the object, aligned in the time-axial direction. Indentations, where the flame necks in, produce valleys in the object's surface.

A volume has been rendered in Figures 4.5(a) and (b) for each the flames in Figures 4.3(a) and (b) respectively, for a series of 100 frames (1.6s) beginning with those already shown. A low ambient light level has been used in conjunction with a point light source located far to the left of the volume, along the upstream axis, so that the "ridge-tops" are brightly illuminated and the valleys are cast-in-shadow producing alternating dark and light bands. These conditions have been selected to match those selected by Mungal *et al.* (1991) to facilitate a direct comparison between the FPJ flame structures and those found in a simple jet flame. *Figure 4(a)* from Mungal *et al.* (1991) is reproduced here, with permission, as Figure 4.6 to more easily facilitate easy comparison of the flame structures produced by simple jet and FPJ flames.

Each large puff structure in the FPJ flame (Figure 4.5) is clearly seen to form at the very base of the luminous part of the flame and to grow in stream-wise extent. A fluctuation in the apparent lift-off height (bearing in mind that the camera does not detect the blue base of the flame) can be seen and this is associated with the formation of each new luminous structure. As the structure moves downstream it initially travels with a nearly constant celerity (speed), as seen from the straight edge of the light and dark bands. The comparable images from buoyancy and momentum dominated turbulent jet diffusion flames can be found in Figure 4.6 and in Mungal *et al.* (1991 and 1992). Figure 4.5 shows similar features to *Figure 6* of Zukoski *et al.* (1980), in which the motion of puff structures are tracked from the base of the flame to the tip. Likewise there is no pairing or large-scale interaction evident between the structures of the present flame.

As each puff structure in the FPJ flame burns out the flame tip drops back to the down stream edge of the next upstream structure. Occasionally indents occur near to the top of the volume as a consequence of the burn-out of a structure, or indents occur further upstream and bite more deeply into the volume as a burning structure detaches from the main body of the flame, termed a separation (Mungal *et al.*, 1991).

Measurements, based on the slope of the bands, have been made of the celerity of the puff structures, S, in the region where it is approximately constant (Table 4.1), ie. at about one third of the maximum flame length. Further downstream from this location there is an apparent acceleration as the structures burns inward and the remaining fuel in the structure is consumed.

The relationship between the celerity of a structure and the characteristic velocity of the gases in the flame is not yet fully understood. Mungal *et al.* (1991) measured the celerity of large-scale structures in turbulent jet diffusion flames ranging from momentum dominated to buoyancy dominated. They found that the celerity of the burning structures remains constant along the majority of the flame length with a value of 12% of the jet exit velocity and to be approximately independent of fuel type (ethylene and acetylene). This implies that the characteristic vertical velocity is lower for buoyancy dominated flames than for a momentum dominated one, which is to be expected. The celerity of the flames investigated by Mungal *et al.* (1991) was found to vary in the range $2 \le S \le 30$ m/s. The gas velocities at the visible flame tip were found to vary between 8% and 25% of the jet exit velocity. The present results are consistent with the celerity of a buoyancy dominated simple jet flame. Zukoski *et al.* (1984) suggest that S asymptotes to a maximum value of $S = 0.6(gx)^{\frac{1}{2}}$ at $x = 0.4\overline{X}$ in a pool fire and, by comparison with velocity measurements from the literature, deduce that the convection speed of the gas on the center-line of the flame is typically four times greater than S. Here we find that the value of $S = 1.0(gx)^{\frac{1}{2}}$ at $x \approx 0.4\overline{X}$ in broad agreement with the buoyant flames of Zukoski *et al.* (1984) again suggesting that the present flow structures are buoyancy dominated.

The relative significance of axial momentum and of buoyancy in a FPJ flame has been investigated further by firing a FPJ burner **horizontally**, mounted centrally under a fume hood with the burner axis located 900mm above the floor. A long exposure image of a 45kW flame is shown in Figure 4.7. The flame is seen to turn sharply upwards very close to the nozzle. Measurement from this photograph enables a comparison of the relative influences of jet exit momentum and buoyant forces on the flame. The base of the flame is significantly below the burner, consistent with the rapid initial spread of a FPJ flow, and is possibly influenced by the volumetric expansion that accompanies combustion. The maximum distance for which the flame exists below the nozzle axis is 13 nozzle exit diameters. This is compatible with the maximum spread found by Schneider *et al.* (1996b) for a jet produced by a MPJ. The axial throw of the flame is only 30% of the total vertical flame length, demonstrating that buoyancy forces dominate in both the mid and the far fields of the flame. A comparison with Figure 4.1 shows that, apart from the initial region, the overall flame shape is not very different from that of the vertically fired FPJ flame.

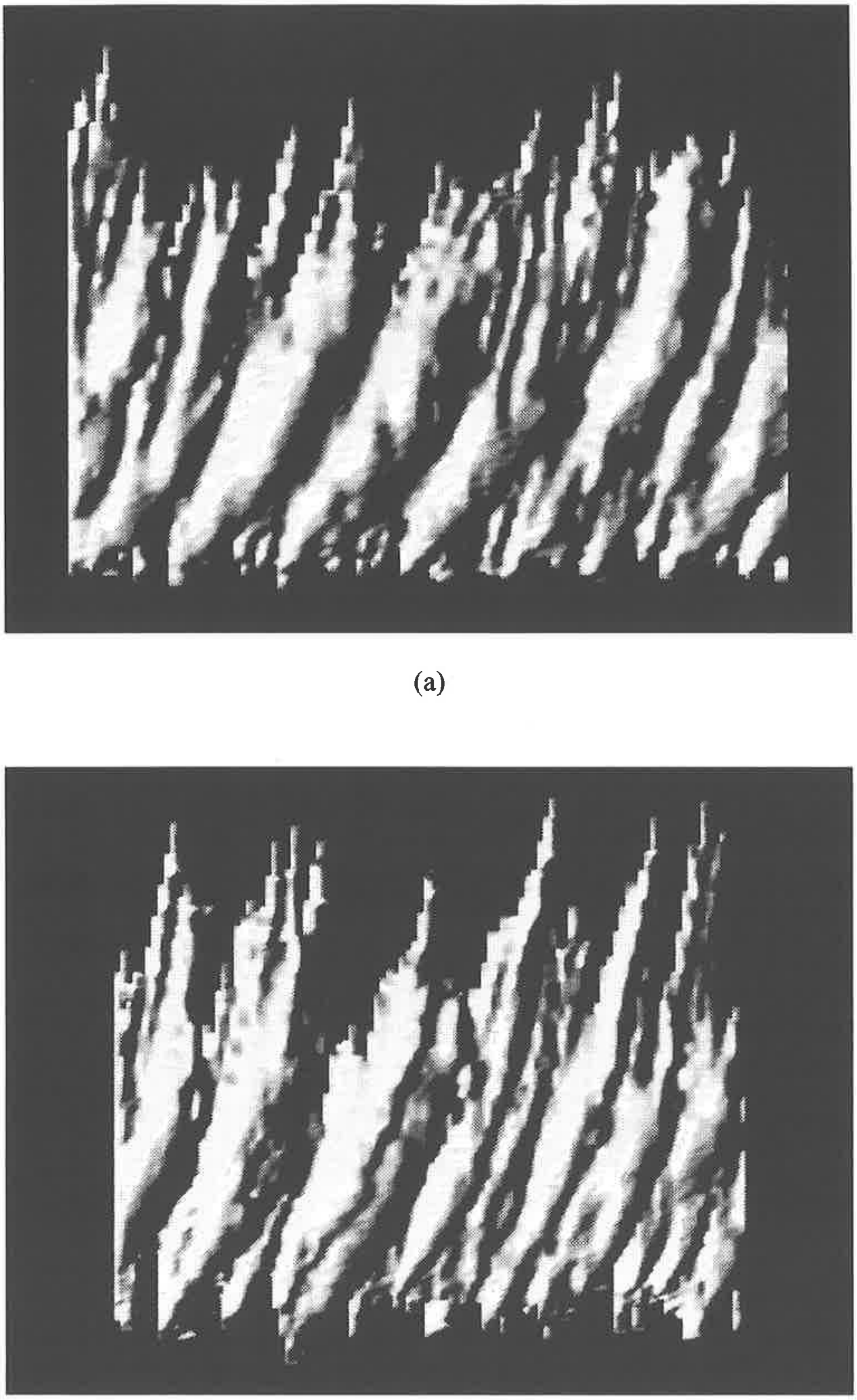

(a)

(b)

Figure 4.5 Volume rendering of an x-y-t object for each FPJ flame in Figure 4.3 that is composed of 100 consecutive x-y video images spaced $\Delta t = 16\text{ms}$ apart. The observer has a viewing angle that is rotated 90° to the time axis, t. Illumination is both from a point light source far to the left and a low ambient light level. (Experimental conditions as for Figure 4.3)

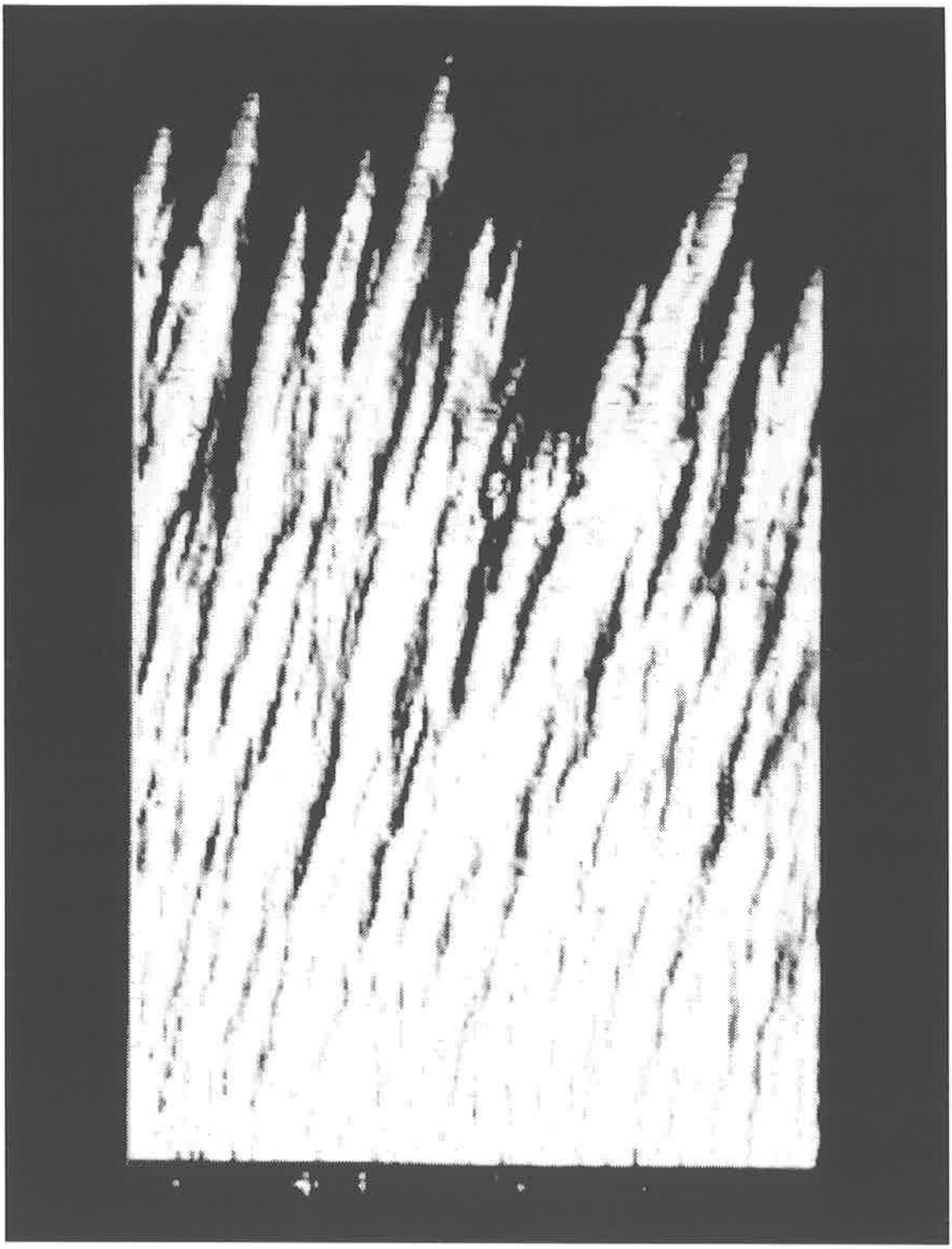

Figure 4.6 Volume rendering of a *x-y-t* object of a simple free turbulent ethylene jet diffusion flame. The image is reproduced, with permission, from *Figure 4a* of Mungal *et al.* (1991). The object is composed of 150 consecutive *x-y* images spaced Δt = 1/200s apart. The observer has a viewing angle that is rotated 90° to the time axis, *t*. Illumination is both from a point source far to the left of the observer and a low ambient light level. ($d = 3$mm, $\mathrm{Re}_d = 5{,}700$, Exposure = 1/200s)

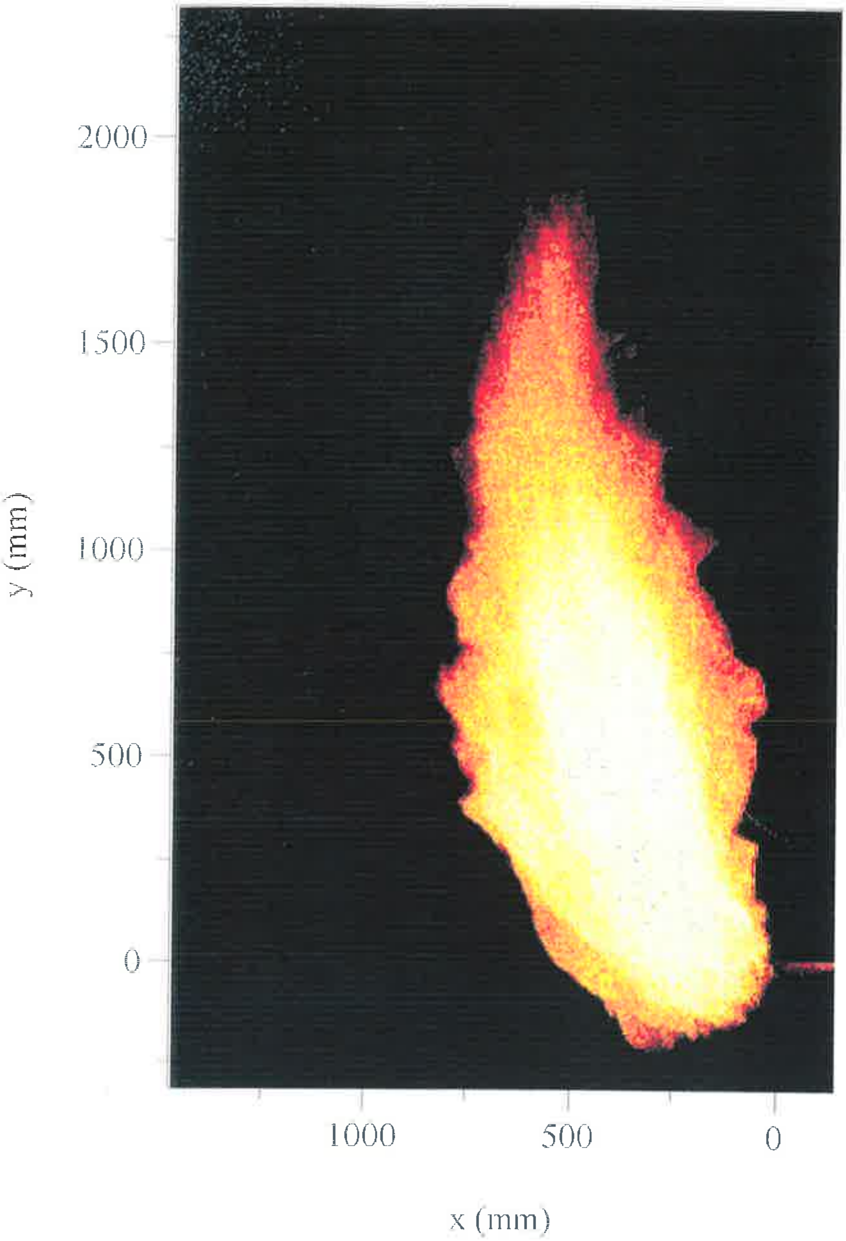

Figure 4.7 Long exposure photographic image of an unconfined FPJ flame fired *horizontally* and from the right with commercial grade propane. ($d_1 = 4.4$mm, $D = 21$mm, $Q = 45.1$kW, $\mathrm{Re}_{d_1} = 37{,}700$, Exposure = 1/2s, Aperture = $f/16$)

4.2.5. Determination of the Global Residence Time

For the present calculations of the global residence time, τ_G, we have used the celerity directly as a measure of the characteristic convection velocity so that $\tau_G = \overline{X}/S$ (Table 4.1). This makes intuitive sense and agrees well with the values of τ_G measured by Nathan *et al.* (1996) using an indirect measure based on global values of flame volume and throughput. The same method can also be used for the present flames if the equivalent exit diameter of the $D = 21\,\mathrm{mm}$ FPJ nozzle is assumed to be 11mm (Nathan *et al.* 1996), and the average flame volume is calculated from the edge of the images in Figure 4.5. This leads to an average value of global residence time for the present $D = 21\,\mathrm{mm}$ FPJ flames of τ_G= 450ms, which is reasonably close to the value of 400ms derived from the global flame volume and the exit velocity for a $d = 10\,\mathrm{mm}$ MPJ nozzle burning propane when the Strouhal number is $St_d = 0.03$ (Nathan *et al.*, 1996). The values for τ_G shown in Table 4.1, calculated from $\tau_G = \overline{X}/S$, are seen to be slightly greater for the $D = 13\,\mathrm{mm}$ nozzle than for the $D = 21\,\mathrm{mm}$ nozzle and to be roughly independent of flow rate. This is somewhat counter-intuitive, but is consistent with the greater buoyancy driven celerity of the larger flames. A good general agreement between the magnitude of τ_G as determined by all these methods supports the present, most direct, calculation procedure.

4.2.6. The Role of Large-Scale Structures in Precessing Jet Flame Stabilisation

It has been demonstrated that the far field of the FPJ flame is dominated by the entrainment into, and mixing within, discrete large-scale structures, in a manner analogous to the simple jet flames investigated by Mungal *et al.* (1991). The dynamic motions of the large-scale structures cause air to be entrained into these structures and to mix with the fuel and combustion products. The oscillation of the flame tip can be attributed to the rapid burnout of successive large-scale puff structures. These structures can be deduced to be of relatively uniform concentration so that the residual unburned fuel within it mixes to a flammable stoichiometry in a time scale that is short compared to the convection time-scale.

It is possible to trace the origin of a puff structure from the flame tip back to the base of the flame. A small radiant structure forms at the base of the flame, near to the burner, and bulges radially outwards as it grows with time. The initial down-stream movement of the new structure is not clearly distinguishable from the initial radial growth phase in the images presented. As the puff structure accelerates upwards, a new structure begins to form from within the non-radiant zone near to the burner where the flame is stabilised in the flow field created by the FPJ.

Nathan (1988) showed that the FPJ flow generates large-scale coherent motions in the region immediately downstream from the nozzle. These structures are also very clearly identified in the flow visualisation in Section 3.2 and are generated at the frequency of precession. The frequency of precession, f_p, can be calculated from the Strouhal number relation, St_M, developed by Hill *et al.* (1995) (see Section 2.1) and used here to compare the puffing frequency measurements in the present work. The precessional frequency is proportional to throughput and, for the present experimental conditions for the $D = 13\,\text{mm}$ nozzle(Table 4.1), is calculated to be $60 \le f_p \le 190\,\text{Hz}$. By contrast the puffing frequency, f, in the flame is roughly independent of throughput and, for the $D = 13\,\text{mm}$ nozzle, it has an average value of 6.5Hz (Table 4.1). Thus it is apparent that multiple precessional cycles (at least 10) occur during the formation of each new puff structure in the flame and that their frequencies are not directly related. Instead, buoyant forces dominate the motions of the large-scale vortical structures that propagate through an unconfined FPJ flame and their associated mixing characteristics. Thus it is apparent that the generation of the large puff structures is not by the vortex pairing mechanism that is usually associated with momentum-dominated jets and flames and was found to occur in the base of flames by Mungal *et al.* (1991). Nevertheless, the mixing field associated with the large-scale flame motions generated by the FPJ nozzle is clearly responsible for establishing the conditions required for the flame to be stabilised near to the nozzle. The FPJ flow is also characterised by a greatly increased rate of reduction in jet velocity. For the unconfined flame this can be expected to result in enhanced flame stability and a greater relative importance of buoyancy forces. The resulting flame has been shown to have improved stability, radiation and emission characteristics relative to momentum driven jet flames (Nathan *et al.*, 1996).

Schneider *et al.* (1997a and 1997b) conducted velocity measurements in the near nozzle region of cold precessing jet flows produced by a MPJ nozzle. They have shown that, within this region, jet precession results in an initial spreading with half-angles of about 45°, the generation of coherent motions over the entire scale of the motion transcribed by the jet precession, and an initial decay in mean jet velocity which is an order of magnitude greater than that in a simple jet. Given that the equivalent exit diameter of the $D = 21\,\text{mm}$ FPJ nozzle is about 11mm (Nathan *et al.*, 1996), the near field region corresponds approximately to the first 110mm downstream from the exit plane of the present $D = 21\,\text{mm}$ FPJ nozzle. Much of this region is upstream from the point of ignition and the remainder is within the flame stabilisation region. The high entrainment of ambient fluid close to the nozzle and the rapid decay of jet velocity there, as found by Schneider *et al.* (1997a and 1997b), are consistent with the establishment of a low velocity combustible mixture by the end of this region. The present measurements of velocity using PIV (Section 3.3) and jet concentration (Section 3.4) confirm that the FPJ flow also generates large regions of slow moving, flammable mixture. Ignition of the low velocity flammable mixture may be expected to generate buoyant forces which, for the present unconfined FPJ flames, dominate beyond the near burner region. Since the near burner region corresponds to only about 10% of the average flame length, the dominant flame motions are not significantly different from that which occurs above a pool fire (Zukoski *et al.*, 1980).

Cetegen and Ahmed (1993) have proposed a mechanism which attributes the puffing phenomenon found in pool fires to the fluid mechanics associated with the region external to the flame envelope. In their experiments they observed that the puffing phenomenon involves the acceleration of buoyant gases from within stagnant surroundings, which causes a toroidal vortex to form immediately outside the burner rim. The vortex initially increases the radial inflow of air, causing the flame to neck in and to move the buoyant mixture downstream. This causes the vortex to weaken and so reduces its influence on the flame envelope. The vortex convects downstream allowing more buoyant gas to accumulate at the flame base which initiates the formation of the next structure. This mechanism is consistent with the observed motions in the present FPJ flames. It relies only on the presence of buoyancy and further supports the notion that, for the FPJ flame, combustion must be stabilised upstream from the large buoyant puff structures which propagate through the flame.

Cetegen and Ahmed (1993) show that the puffing frequency in pool fires assumes a unique value, dependent upon the burner diameter alone. Consequently, there is a well defined characteristic length-scale associated with the large-scale vortex formed at the fixed rim of a pool fire. The dynamics of the large-scale structures in each of the FPJ flames, however, have been found to exhibit variability for a given burner. The mechanism responsible for the generation of large-scale structures in pool fires can be considered applicable if it is considered that the physical dimensions of the base of the FPJ flame are dependent upon the fluid dynamic motions in the flow field downstream from the nozzle. Consequently, the puffing frequency of the flame investigated here cannot "lock-on" to a constant value, as occurs in a pool fire, and this causes the variability of the puffing frequency of the FPJ flames.

The reaction zone at the base of simple jet flames is confined to thin regions around the edge of large-scale jet structures (Schefer *et al.*, 1994a). Intense reaction occurs at locations where mixed fluid is near to stoichiometric. Oscillation in the lift-off height is the result of interactions between shear layer structures and the reaction zone. The combustion zone is convected down-stream by the structures, and then rapidly propagates back upstream (Lin *et al.*, 1993, and Schefer *et al.*, 1994b). It appears, then, that the stabilisation of the FPJ flame is likely to occur in the blue region of the flame close to the nozzle corresponding to the end of the near burner region where the precessing jet issuing from the nozzle exit dominates the mixing processes. While the near burner zone is characterised by large-scale flow motions associated with precession, these motions are not directly related to the puff structures which propagate through the flame, since their frequency and driving forces are different. The buoyant puff structures which propagate through the unconfined FPJ flames are thus concluded to be the result of, rather than the cause of, the flame stabilisation.

4.3. The Structure of the Reaction Zone in a Precessing Jet Flame

4.3.1. Experimental Arrangement

Planar laser induced fluorescence of the hydroxyl radical (OH-PLIF) has been used to determine the structure of the reaction zone in the stabilisation region of a FPJ flame. PLIF measurements are made for a $Q = 16\text{kW}$ propane (LPG) flame issuing from a $D = 13\text{mm}$ FPJ burner, with a throat diameter of $d_1 = 2.3\text{mm}$ and Reynolds number $\text{Re}_{d_1} = 26{,}500$.

As described in Section 2.3.2, the thermal capacity of the extraction flue was restricted to a short term thermal capacity of 30kW and even the 16kW flame investigated here when fired continuously was found to cause temperatures to exceed the flue duct material limits (100°C). Thus the PLIF measurements were restricted to the smallest burner and a relatively low Reynolds number in comparison with the larger flames presented in Section 4.2, though still high enough to provide reliable precession. Nevertheless the Reynolds number is within the range investigated elsewhere so that reasonable similarity can be assumed.

The PLIF measurement technique is described in Section 2.3.2. A camera images a 125×53mm region of the flow downstream from the burner tip. Illumination is provided by an UV light sheet passing through the jet axis. The spatial resolution is 0.22×0.22×0.7mm, which is of comparable scale to the Batchelor length-scale in the non-reacting flow (Section 2.2.3) at the exit plane of the FPJ nozzle ($\lambda_b = 116\,\mu\text{m}$) and sufficiently small to provide good resolution of the flame front thickness. The fluorescence from the OH is collected through a narrow bandpass filter, which eliminates light scattered from soot particles.

4.3.2. Reaction Zone Imaging in a Precessing Jet Flame

Figure 4.8 contains three typical images of the OH radicals within the stabilisation region of a $D = 13$mm FPJ flame. These images are presented with image smoothing. Two types of reaction zones are observed, those with thin continuous structures typically 2-5mm thick (Fig. 4.8(a)), spanning the height of the imaging region, and diffuse zones, often thicker than 10mm (Fig. 4.8(b)), that can extend across the nozzle centre-line (Fig. 4.8(c)). The structure of the reaction field in simple jet diffusion flames is generally found to be of the former type, confined to zones typically 2mm thick at the edge of the fuel jet (Schefer *et al.*, 1994a). Similar diffuse reaction zones have also been observed, but at the tip of H_2 jet diffusion flames (Sietzman *et al.*, 1990).

The present flame is lifted in all cases and has a mean lift-off height of 9.7mm and a fluctuating height that varies in the range of 6-26mm for the throat velocity $u_{d_1} = 50$ m/s. Nathan and Luxton (1991c) determined visible lift-off heights for the same $D = 13$mm nozzle for commercial methane fuel (CNG – compressed natural gas). Their results show a comparable mean lift-off height of 15mm for a throat velocity $u_{d_1} = 50$ m/s.

The low signal to noise ratio in Figure 4.8, S/N < 1, results from the large attenuation of the narrow band-pass filter which is necessary to eliminate the scattered signal from soot particles present in the flame, and by the low power of the laser system at this wavelength (<10mJ/pulse). More recent experimental results with a $D = 10$mm methane FPJ flame, where soot is not present at the flame base to nullify the need for optical filtering, and allowing excitation of the fundamental transition with an associated increased pulse power, produces increased signal to noise, S/N > 10 (Alwahabi *et al.*, 1997). Those images obtained are qualitative by similarity to the images presented here. Thus the features identified above can be considered genuine, and are not an artefact of poor signal to noise ratio.

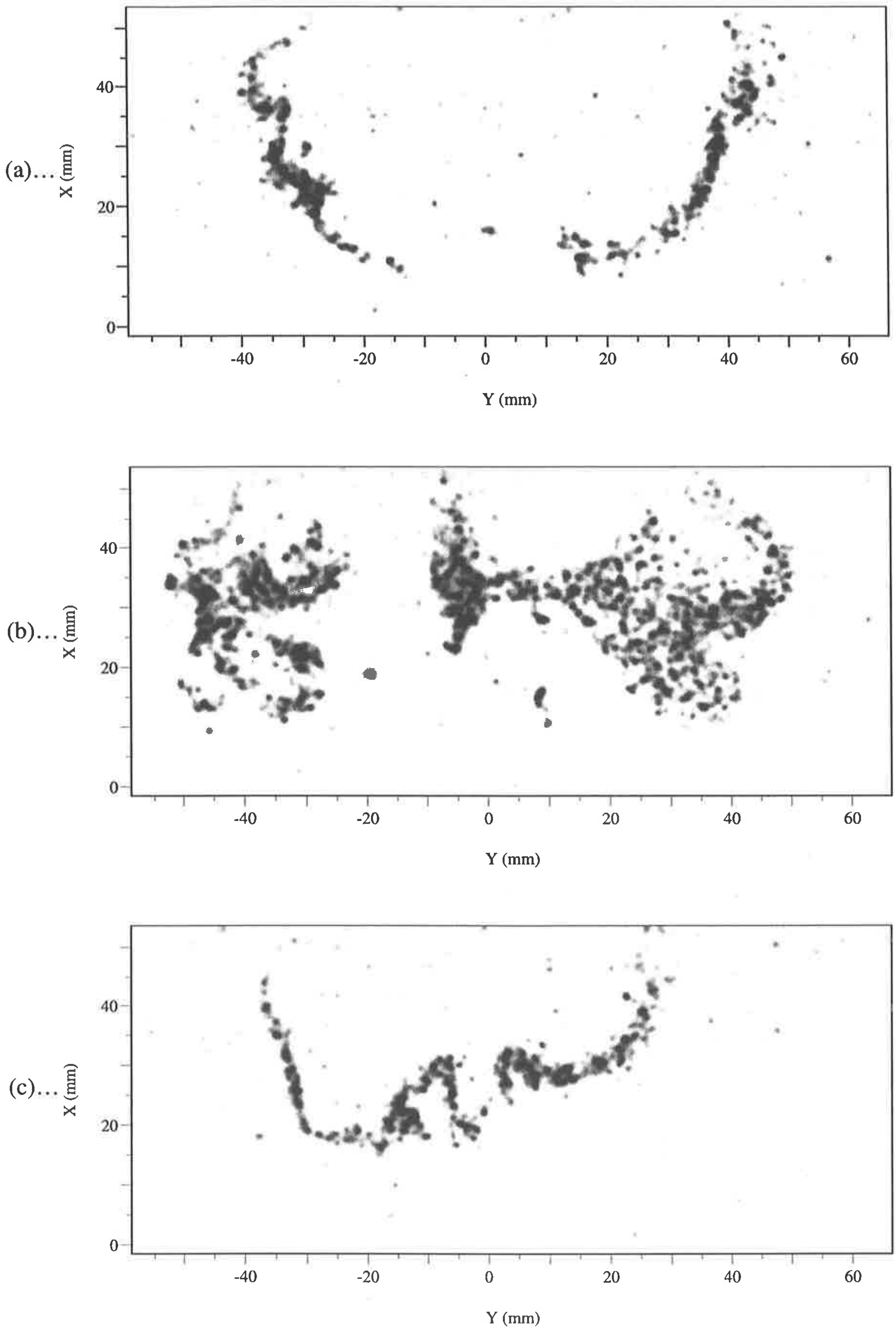

Figure 4.8 OH-LIF images for a vertically fired unconfined FPJ flame. ($d_1 = 2.3\text{mm}$, $D = 13\text{mm}$, $\text{Re}_{d_1} = 26{,}500$, $Q = 16\text{kW}$, Fuel = commercial grade propane)

4.4. The Flow Field Environment in the Region of Flame Stabilisation

4.4.1. Experimental Arrangement

A qualitative and quantitative comparison is made between the non-reacting scalar mixing field and the structure of the reaction zone in the FPJ flow in the vicinity of the stabilisation region, to provide insight into stabilisation processes in the ignition region. The scalar mixing field of a $D = 13\text{mm}$ FPJ non-reacting flow (Section 3.4) is compared with the reaction zone for a propane FPJ flame from the same burner nozzle (Section 4.3). The experimental and flow conditions for the two cases have been approximately matched based on the jet throat variables, with a throat diameter $d_1 = 2.3\text{mm}$ and a Reynolds number of $\text{Re}_{d_1} = 20{,}500$.

The instantaneous non-reacting jet concentration field has been determined using the planar Mie scattering technique described in Section 2.2.3. From these measurements a 125×55mm area of the flow is considered that is coincident with the field of view for the reaction zone imaging. It is noted that each pixel has a spatial resolution of 0.47×0.47×0.25mm so that the mixture field is not spatially resolved right down to the Batchelor length-scale at the exit plane of the FPJ nozzle ($\lambda_b = 116\,\mu\text{m}$). Nevertheless the resolution is found to be adequate for the evaluation purposes required.

4.4.2. Non-reacting Scalar Mixing Measurements

The non-reacting scalar mixing measurements are used to assess the nature of the mixing field in the FPJ flame stabilisation region, based on the reasoning that the cold flow turbulence controls mixing upstream of the reaction zone. Comparison of the structure of the reaction field marked by the presence of OH radicals (Figure 4.8) is made with the local instantaneous jet concentration field, ξ, that is mixed within the flammability limits. Fluid within the flammability limits of the commercial grade propane fuel used in the reaction zone imaging experiment, $0.02 \le \xi \le 0.10$ (Glassman, 1987), is displayed using a false colour scheme in Figure 4.9. Lower jet concentration values are coloured white and higher jet concentration values are coloured yellow. It is clear from these images that flammable mixtures exist in both broad and narrow regions at the outer edge of the flow. These regions exist near to the mean location of flame stabilisation. All of the features observed in the base of the flame in Figure 4.8, namely combustion being present along the nozzle axis, and broad regions of flammable mixture, can be observed in the characteristics of the flammable mixture in the non-reacting flow images. That the instantaneous structure of the reaction field is seen to coincide qualitatively with the structure of the flammable region suggests that the position of the reaction is controlled by the cold flow mixing required to generate a flammable mixture, a necessary prerequisite for reaction to occur. Thus the mixing upstream from the reaction must be a dominant element of the flame stabilisation model that applies to this flow. Chemical reaction will generate heat release and volume expansion that will influence the mixing downstream from the reaction zone and can be expected to smooth the reaction contours. Nevertheless, the qualitative similarity between hot and cold images suggests that the cold flow characteristics dominate the mixing in the stabilisation region at the base of the flame.

Vanquickenborne and van Tiggelen (1966) suggest that the stabilisation point of simple lifted jet flames occurs where the fuel and the air are premixed to a stoichiometric mixture, rather than to jet concentrations within the broader flammability limits of the fuel. In their model extinction of the flame is caused by local gas velocities exceeding some turbulent flame speed. Recent data from Muñiz and Mungal (1997) shows that the instantaneous fluid velocities in the flame never exceed three times the maximum laminar flame speed. Whilst the present data do not provide the instantaneous velocity field it has been demonstrated that generally low velocities exist in the region adjacent to the jet exiting the FPJ nozzle (Section 3.3). This result is consistent with the notion that flame stabilisation coincides with the creation of a low velocity flammable region in which combustion can be sustained. It can also be surmised that a very low velocity region must be present in order for combustion to be sustained away from the stoichiometric contour, as can be deduced to occur in the broad regions of flammable mixture that have been identified in both the hot and cold measurements. Low velocities are required because flame speed is at a maximum at slightly rich conditions but decreases markedly as the concentration moves either side of stoichiometric.

The scalar dissipation, χ, is considered an important parameter in the flamelet model of Peters and Williams (1983) and the QEDR model of Bilger (1988). Figure 4.10 shows the χ field for the jet concentration measurements presented in Figure 4.9. The calculation follows the calculation scheme that has been outlined in Section 3.4.7. It has been noted in Section 2.2.3 that the limited spatial resolution used here is not expected to fully resolve the true scalar mixing field and that would result in an underestimate of the peak χ. This is not considered to be important here, because extinction by high χ is shown later not to control combustion, so that knowledge of the true peak value is not critical.

The structure of the scalar dissipation field shows that high χ occurs principally in the vicinity of the jet emerging from the FPJ nozzle. Despite the limitations in resolving the peak

χ, the trends in the scalar dissipation field suggest a tendency for the highest values to occur at the edge of the jet emerging from the FPJ nozzle. This is consistent with the trends found to occur in a simple jet where high χ exists at the outer edge of vortical structures in the shear layer (Feikema *et al.*, 1996). Downstream from the instantaneous emerging jet the peak values of χ are significantly lower and are found to occur in regions adjacent to the flammable region. The regions in which local peak values of χ are found is confined to thin layer like structures associated with the interface between "islands" and "peninsulas" of jet fluid that is frequently of a flammable mixture.

Schefer *et al.* (1994a) have demonstrated that the instantaneous χ value immediately upstream from the flame stabilisation point in simple jet flames is significantly less than $\chi \approx 12\text{s}^{-1}$, which they used as the value of χ required to cause extinction of laminar flamelets. Likewise for the FPJ flow, regions where $\chi > 12\text{s}^{-1}$ are only evident at the edge of the jet exiting from the FPJ nozzle. Thus while it is possible that high χ prevents reaction in this region in FPJ flames, it does not control the combustion in the region of flame stabilisation.

The QEDR model of Bilger (1988) suggests that at the base of lifted jet flames the flamelet concept (Peters and Williams, 1983) is most likely to be valid and that the flame will more closely follow the stoichiometric contour than the dissipation contours. The dissipation layers that are observed throughout the present flow typically span 1mm. Dissipation layers also play a role in the SDRL model of Bish and Dahm (1995). Flamelet models require that laminar conditions exist in the reaction zone. The OH structures are significantly thicker than the thickness of the dissipation layer in which laminar-like conditions apply. This demonstrates that laminar flamelet concepts may be invalid, because turbulent conditions can exist within the reaction zone.

The correlation between ξ and χ is demonstrated from their joint probability density function, jpdf(ξ, χ). Here χ results are presented across the region of flow at the downstream location coincident with the mean lift-off height. It is possible to account for the difference in densities of the nozzle fluid, ie. the difference in density between the commercial propane that was used in the reacting flow study and the air that was used in the scalar mixing study. Jet concentration measurements can be suitably scaled by an effective diameter (Thring and Newby, 1953),

$$d^* = d_1\left(\frac{\rho_0}{\rho_\infty}\right)^{\frac{1}{2}}.$$

Pitts (1991) has demonstrated that this parameter correctly accounts for the variation in mixing behaviour for different density jets. For the commercial propane fuel $\rho_0/\rho_\infty = 1.52$, so that the mean stabilisation height of 9.7mm corresponds to $x = 7.9$mm in the non-reacting flow.

The jpdf(ξ, χ) for the axial position $x = 7.9$mm at the radial locations $y = 0$ and $y = 7.9$mm in the non-reacting FPJ flow are shown in Figure 4.11. The jpdfs are determined from a 7×7pixel sub-window that is centred on the relevant location corresponding to an area of 3.3mm×3.3mm. The centre-line jpdf (Figure 4.11(a)) demonstrates that the jet exiting the FPJ nozzle is characterised by a broad range of ξ and high χ. The broad ξ range is consistent with the high unmixedness found in Section 3.4.3 (Figure 3.23) in the region immediately downstream from the nozzle that is associated with the "flip-flop" motion of the emerging jet. High χ values are a consequence of the intense gradient across the shear layer of the emerging jet. However this is associated with fluid that is above the rich flammability limit. The off-axis jpdf (Figure 4.11(b)) shows considerably more fluid with lower values of ξ and a dominant peak at $\xi = 0$ demonstrating that this location is commonly external to the flow. For fluid within the flammability limits, $0.02 \le \xi \le 0.10$, the values of χ are significantly lower than those in the exiting jet and χ is one to two orders of magnitude less than $\chi \approx 12\text{s}^{-1}$ that would be required to cause extinction of laminar flamelets. A contribution to the jpdf from fluid with both high ξ and high χ is also evident, similar to that found to be characteristic of the jet exiting from the nozzle.

These results demonstrate that the characteristic features of fluid within the flammability limits in the non-reacting flow are consistent with the features found in the reaction field images that were presented in Figure 4.8. The cold mixing field data suggest that there is considerable fluid within the flammability range that exists in a low velocity region. It also demonstrates that the position of the flame front is not controlled by scalar dissipation. Rather all fluid in the vicinity of the flame front that is mixed within the flammability limits is found to have maximum values of χ which are one to two orders of magnitude below that required to cause extinction of laminar flamelets.

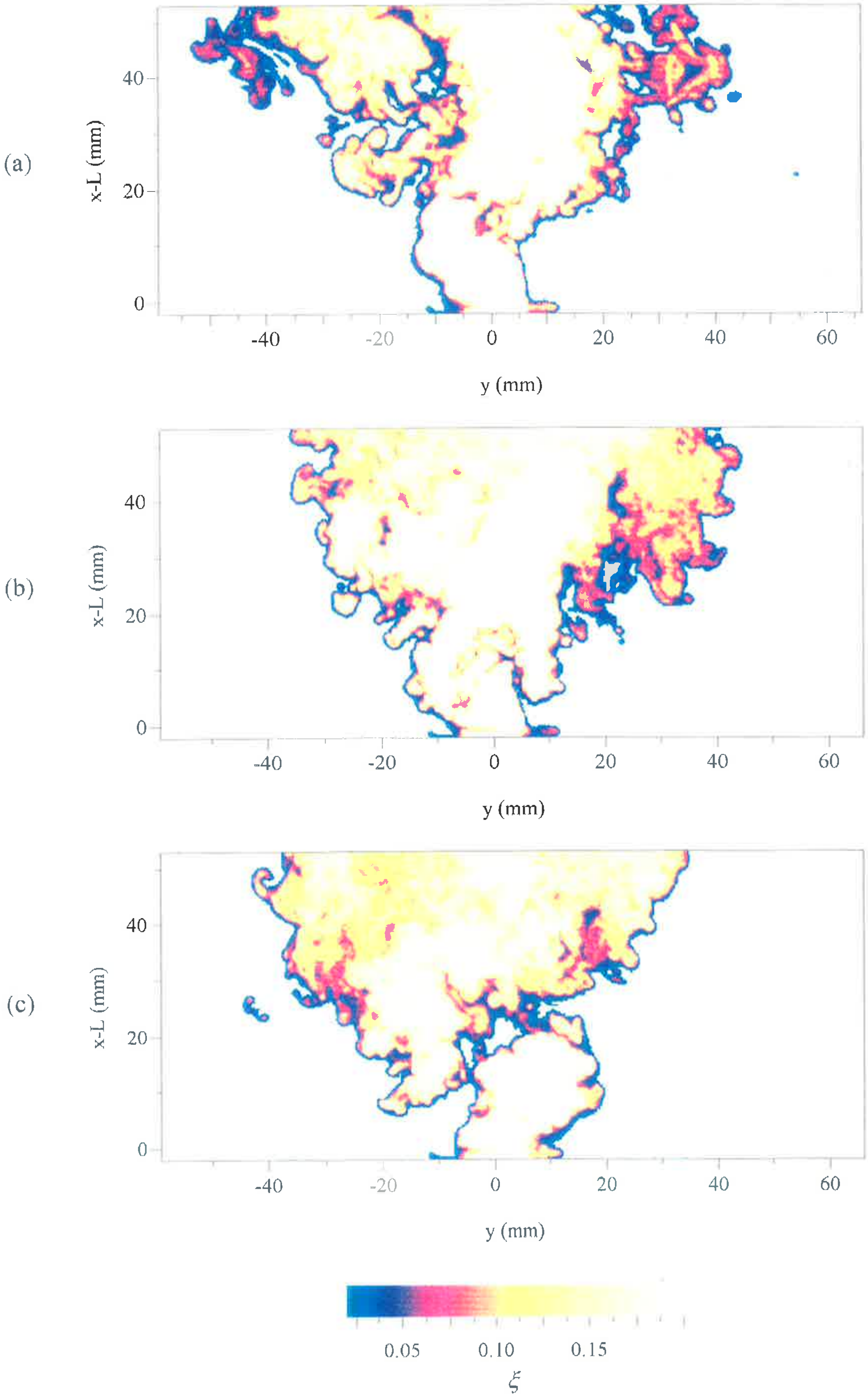

Figure 4.9 Instantaneous images of the jet concentration field in the non-reacting FPJ flow highlighting mixed fluid within the flammability limits of propane, $0.02 \le \xi \le 0.10$. ($d_1 = 2.3\mathrm{mm}$, $D = 13\mathrm{mm}$, $\mathrm{Re}_{d_1} = 20{,}500$, Working fluid = air)

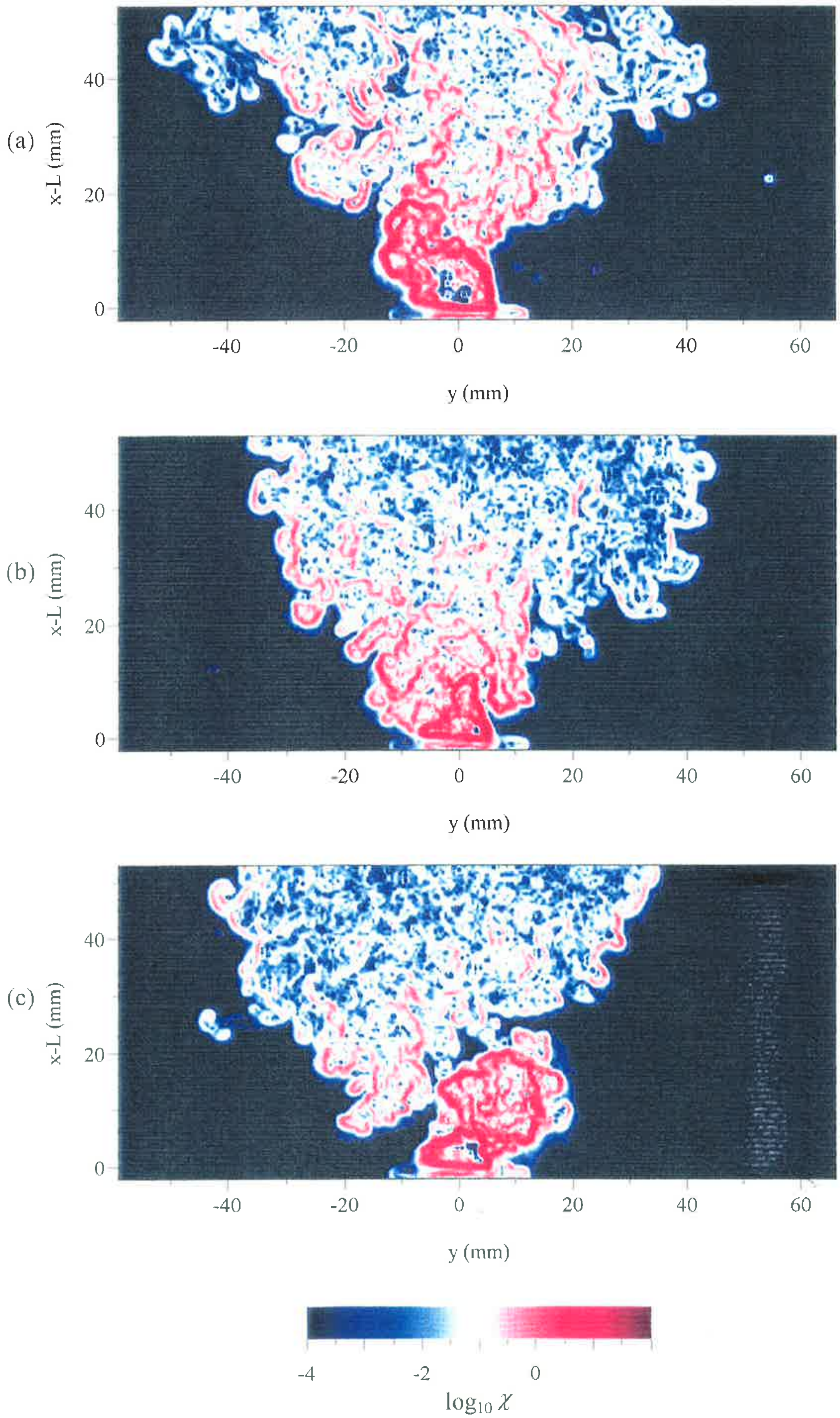

Figure 4.10 Instantaneous images of the scalar dissipation field, χ, for the non-reacting FPJ flow. (Experimental conditions as for Figure 4.9)

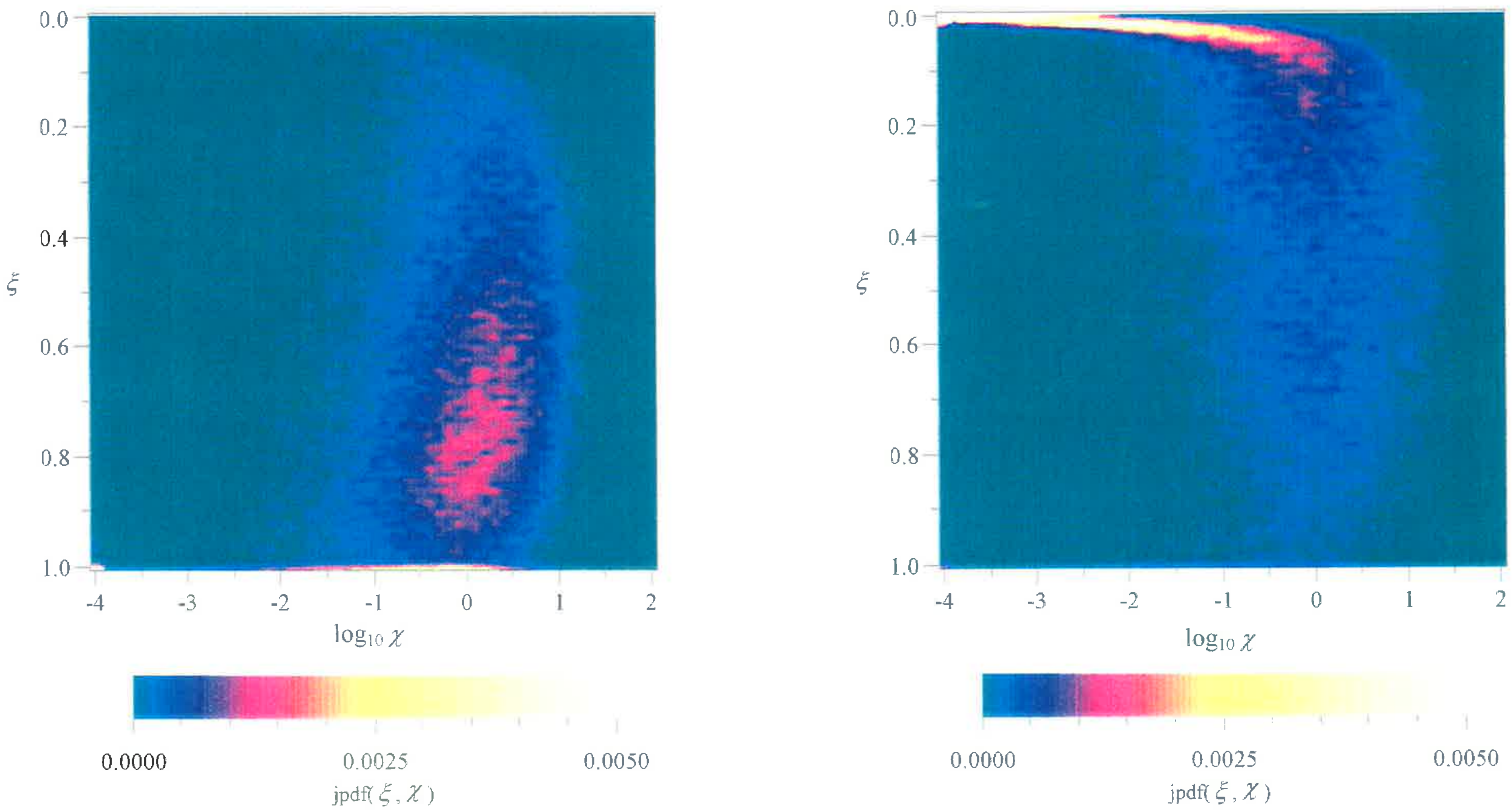

(a)

(b)

Figure 4.11 Joint probability distribution function of the jet concentration and the scalar dissipation, jpdf(ξ , χ), for the non-reacting FPJ flow. (a) On the jet centre-line at $x = 7.8\text{mm}$ and at (b) $x = 7.8\text{mm}$ and $y = 7.8\text{mm}$. (Experimental conditions as for Figure 4.9).

4.5. Flame Stabilisation Mechanisms in the Precessing Jet Flow

Qualitative and quantitative experimental data that can be used to explain the stabilisation process in FPJ flames has been presented and discussed. Precession of the jet is generated by the fluid mechanical instability within the FPJ nozzle formed by the addition of the chamber section downstream from the jet throat. Mixing and combustion characteristics of precessing jet flows have been assessed from visualisation of the flame envelope (Section 4.2), from reaction zone imaging (Section 4.3) and from non-reacting jet concentration measurements (Section 4.4).

The physical mechanisms responsible for jet flame stabilisation, which can be used to predict flame lift-off and blowout behaviour in simple jet flames, have been considered here in relation to FPJ flames.

The principal flame stabilisation models for simple jet flames have been discussed previously in Section 1.2.1. The physical combustion criteria considered in each of these models are as follows:

- Vanquickenborne and van Tiggelen (1966) propose that stabilisation occurs along the stoichiometric contour that results from the mixing upstream from the flame front.
- Peters and Williams (1983) suggest that there is insufficient time for significant premixing to occur upstream from the flame front and propose that stabilisation occurs in flamelets that are thin relative to the dissipation scales.
- Broadwell *et al.* (1984) propose that the flame must propagate from one large-scale coherent structures to its next upstream neighbour.
- Bilger (1988) proposes that reaction zones at the base of the flame will be thicker than the Kolmogorov scale and are centred very near to the stoichiometric contour so that they have the appearance of flamelets along the contour.

- Bish *et al.* (1995) relates the chemical state of combustion to the mixing state of a scalar. The presence of layer-like scalar dissipation structures in the mixing field is related to a locally one-dimensional structure in the underlying chemical species fields.

The findings presented here have been considered in relation to the possible stabilisation mechanisms by considering the validity of the proposed mixing and combustion characteristics. Large-scale buoyant structures, which propagate through the unconfined FPJ flames, are concluded to be the result of, rather than the cause of, the flame stabilisation. It has been demonstrated that combustion occurs in both thin and thick reaction zones that are generally located at the edge of the flow field but can span the entire base of the flame in a layer-like manner. The flame front is clearly not distributed in any uniform manner through large structures, so that the mechanism proposed by Broadwell *et al.* (1984) does not apply. The instantaneous structure of the reaction field has been shown to possess the same qualitative features as the structure of the flammable region in the non-reacting flow case as found in the same region. Comparison with velocity measurements in non-reacting FPJ flows in the stabilisation region suggests that the velocity in this region is generally low. The reaction layers are thick compared with the thickness of dissipation layers discounting the premixed flamelet stabilisation model of Peters and Williams (1983). High scalar dissipation is restricted to regions within the emerging jet, immediately downstream from the FPJ nozzle, which is well upstream from the mean stabilisation point. Thus high scalar dissipation does not cause local extinction or control the position of the flame front.

These results demonstrate conclusively that *the physical mechanism discussed above which have been proposed for simple jet flame stabilisation, other than those which include the existence of a premixed flame zone, are inappropriate for the precessing jet diffusion flame.* That is, the flame is stabilised at the edge of large, relatively slow moving structures, in regions where fluid is premixed and within the flammability limits upstream from the flame front.

Chapter 5

5. The Influence of Mixing on Sooting and NO_x Emission Characteristics of Precessing Jet Flames

5.1. Introduction

Changes to flame chemistry resulting from changes to the mixing by jet precession are investigated further in this chapter. Mixing is considered in relation to global trends in NO_x emissions and soot formation in precessing jet flames. Comparison is made with published empirical relations and models derived for simple turbulent jet diffusion flames.

Species emissions, flame shape and radiant fractions have been measured for unconfined flames of methane and propane issuing from a mechanical precessing jet (MPJ) nozzle (Nathan *et al.*, 1996) and Turns *et al.* (1994). The wide range of differing types of mixing that can be produced by a MPJ nozzle correspond to quite different radiant fractions and species emissions. The low St_d flames which are short and blue with high CO, have a high ratio of NO_2 to NO, while the high St_d flames, which are broader and orange, have lower NO_x emission indices than do simple jet flames. They found that global characteristics of FPJ flames are closely matched to those from high St_d MPJ flames. High St_d MPJ flames show an increase of about 15% in the radiant fraction and a reduction of about 25% in the NO_x emissions relative to a simple jet flame. The link between the mixing characteristics and NO_x emissions and soot formation in flames is explored with regard to the strain rate at the flame tip in this chapter.

5.2. Mean Strain Rate in Precessing Jet Flames

Further insight into the effect of precession on the combustion characteristics of a jet flame can be determined by comparison of the characteristic strain rates in simple and FPJ flames. Reference is made to the results that were presented in Section 4.2 for commercial grade propane flames from FPJ burners with chamber diameters of D = 13mm and D = 21mm (Table 4.1).

The characteristic strain rate at the tip of vertical unconfined simple jet flames can be calculated from the characteristic vertical velocity divided by the flame diameter at the tip of the flame. Røkke *et al.* (1994) estimated this tip strain based on the exit conditions and used empirical relations to obtain values for the variables at the flame tip. If the characteristic vertical velocity is taken instead as the celerity, S, then the strain rate can be calculated for the present FPJ flames and a comparison with free turbulent jet diffusion flames can be made, using the findings of Mungal *et al.* (1991).

Table 5.1 shows the strain rate at the jet throat, u_0/d, for both FPJ flames and the flames investigated by Mungal *et al.* (1991). This table shows that the D = 21mm FPJ flames span a similar Reynolds number and jet throat strain rate range to that of Mungal *et al.* (1991) for simple jet flames. The buoyancy parameter provides a criterion by which the effects of buoyancy can be quantified in simple jet flames. A value of this parameter less than 2 is considered to indicate a momentum dominated flame and a value greater than 10 is considered to indicate a buoyancy dominated flame. It is apparent that Mungal *et al.* (1991) investigated simple jet diffusion flames ranging from momentum dominated to buoyancy dominated.

Mungal *et al.* (1991) found that the celerity of the burning structures remains constant along the majority of the flame length with a value of $S \approx 0.12u_0$ and found the celerity to be approximately independent of fuel type (ethylene and acetylene). This implies that the characteristic vertical velocity is lower for buoyancy dominated flames than for a momentum dominated one, which is to be expected. The local gas velocities at the visible flame tip, $u_{\overline{X}}$, were found to vary $0.08u_0 \leq u_{\overline{x}} \leq 0.25u_0$, so that S is a reasonable estimate of the gas velocity at the flame tip. They demonstrated that the fluctuations in flame length, ΔX, resulted from the burnout of successive large-scale structures, which scales with the local large-scales in the flow, namely $u_{\overline{X}}$ and the jet diameter, l. Thus the length-scale of fluctuations in simple jet flame lengths, ΔX, was determined to scale in direct proportion with l at the mean position of the flame tip, determined from the relation $l = 0.44\overline{X}$. Consequently, the strain rate at the tip of a jet flame can be determined from the relation $S/\Delta X$. The range of simple jet flames that they investigated demonstrate that the flame length asymptotes to $\overline{X} \approx 230d$. Thus, these relations show that S is linearly proportional to u_0, and ΔX is linearly proportional to d, so that $S/\Delta X$ will scale directly with u_0/d for momentum dominated simple jet flames. Consequently, trends in the strain rate at the jet throat scale in proportion with the strain rate at the flame tip for those flames.

The celerity, S, and fluctuation length, ΔX, for each of the FPJ flames was determined previously (Table 4.1). It was shown that S is not strongly dependent upon burner diameter or flow rate at the nozzle throat for the FPJ flames and its values are measured to be of the order of $S \approx 2$ m/s. The celerity of the flames investigated by Mungal *et al.* (1991) was found to increase with exit velocity over the range $2 \leq S \leq 30$ m/s. The fluctuations in the FPJ flame length are roughly a constant proportion of the flame length and do not change significantly with exit velocity. Relative fluctuations in flame length, $\Delta X/\overline{X}$, in the FPJ flames are roughly twice that in the simple jet flames.

Table 5.1 shows that the strain rate at the flame tip in all of the FPJ flames have a value of about 5s^{-1} which is comparable with that calculated for the buoyancy driven jet flames investigated by Mungal *et al.* (1991). The value of strain rate at the flame tip in FPJ flames is independent of burner throughput in contrast to simple jet flames. These results are consistent with the finding that the large-scale structures in FPJ flames are buoyancy driven across the wide range of burner throughputs that are investigated in Chapter 4 of the present study. However the strain rate at the flame tip of the simple jet flames increases with exit velocity so that the buoyancy dominated flames have a tip strain rate that is an order of magnitude higher than that of FPJ flames. These trends, taken together, are unambiguous and clearly demonstrate that the characteristic strain rates through the majority of the flame produced by jet precession are lower than those in momentum dominated non-precessing flames.

Note that this type of dimensionless comparison based on a direct measure of actual flame properties also avoids any problems associated with attempting a direct comparison between the exit flows produced by a FPJ (which are not well defined) and those of a simple jet. While an "equivalent" exit diameter and velocity of the jet leaving the FPJ nozzle have been defined by Nathan and Luxton (1991c), the jet which leaves the chamber is not of circular cross section, does not fill the exit plane of the nozzle, and fluctuates with time, so that this definition is necessarily somewhat arbitrary.

Burner Diameter	Fuel	Reynolds Number Re_{d_1}	Jet Throat Strain Rate $\frac{u_0}{d}$ (s^{-1})	Buoyancy Parameter	Flame Tip Strain Rate $\frac{S}{\Delta X}$ (s^{-1})
D = 13mm	Propane	45 400	37 000		4.5
(d = 2.3mm)	-	73 300	59 500		5.6
-	-	100 000	81 500		6.2
-	-	140 900	115 000		5.4
D = 21mm	-	27 300	6 100		5.7
(d = 4.4mm)	-	38 000	8 400		5.5
-	-	49 400	11 000		5.0
-	-	61 400	13 700		6.5
-	-	74 200	16 500		5.0
-	-	87 600	19 500		3.7
-	-	101 500	22 500		5.0
d = 3mm	Ethylene	5 700	5 300	10.2	6.9
-	-	10 900	10 000	6.4	13.6
-	-	21 400	20 000	4.4	24.2
-	-	43 500	40 000	2.9	47.4
-	Acetylene	5 380	5 300	9.9	7.3
-	-	9 830	10 000	5.4	16.5
-	-	19 600	20 000	3.9	28.7
-	-	39 400	40 000	2.9	49.5
-	-	78 800	76 700	1.9	90.9
-	-	86 500	83 300	1.8	98.8

Table 5.1 Flame strain rate for flames presented in Table 4.1. Data for d = 3mm flames from Mungal *et al.* (1991).

5.3. The Relationship Between Soot Formation and Strain Rate in Precessing Jet Flames

The effect of mixing parameters on soot volume fraction and flame temperature in acetylene turbulent jet diffusion flames have been investigated by Kent and Bastin (1984). They determine from measurements of soot volume fraction that at low strain rates at the jet throat, u_0/d (where u_0 is the jet throat velocity and d is the throat diameter), soot formation and oxidation are controlled by the mixing rate while at high strain rate they are controlled by soot kinetics. Soot volume fraction profiles were found to scale with respect to a characteristic flame mixing time, d/u_0. This mixing time is also the inverse of the strain rate at the jet throat. That is, low strain rate correlates with high soot volume fraction for a simple jet flame. They also show that soot oxidation (burnout) is predominantly mixing rate dependent although temperature and species concentrations also play a significant role. A balance must be achieved between the soot production and soot oxidation rates if a non-smoking flame is to occur. At sufficiently low temperature (<1100°C) the oxidation of soot is quenched and the flame will emit smoke.

Comparison of the strain rate at the flame tip in simple jet and FPJ flames has been made in Section 5.2. It has been shown that the strain rate at the tip of an FPJ flame is lower than in a simple jet flame. This is consistent with the higher sooting tendency deduced to occur in the present FPJ flames (Section 4.2) and also for the high St_d MPJ flames (Nathan *et al.*, 1996).

Nathan *et al.* (1996) present images of a low St_d and a high St_d MPJ flame with the same u_0 and d, and therefore constant jet throat strain rate, as defined by parameter u_0/d. However these images visually demonstrate different sooting characters that can only be attributed to the effect of jet precession on mixing, suggesting that strain is altered by precession for the same u_0/d. The low St_d flame is pale blue due to gas chromatic radiation while the high St_p flame is bright orange due to soot luminescence. This implies that combustion occurs predominantly in a region characterised by increased strain in low St_d flames while it predominantly occurs in a region characterised by reduced strain in high St_d flames. The change in sooting character found in MPJ flames correlates with the trends of reduced mixing rate trends for soot formation in free turbulent jet diffusion flames. Thus it is concluded that (precession of a jet at high St_d produces a flow in which the strain rate in the main body of the flame is reduced resulting in increased sooting tendency, and that the strain rate at the jet throat is not representative of the local strain rate within a precessing jet flame.)

5.4. Mixing and NO_x Emissions in Precessing Jet Flames

The decrease in the NO_x emissions which result from high St_d mixing ($St_d > 0.015$) in MPJ flames has been related to changes in the global residence time and characteristic flame temperature of the gases in the flame by Nathan *et al.* (1996) and Turns *et al.* (1994). The flame temperature was calculated based on flame volume and measured radiant fractions. The trend for MPJ flames is consistent with similar trends measured in free turbulent jet diffusion flames by Turns and Myhr (1991) and Turns *et al.* (1993) in which the radiant fraction changed with the differing sooting propensity of different fuels. The influence of flame radiation on NO_x emissions can also be seen in the work of Boerstoel *et al.* (1994 and 1995). They perform a numerical simulation of combustion in a glass furnace and show that flue NO_x emissions are reduced by 40% by including soot formation in their combustion model and better agree with the furnace measurements. This demonstrates that soot has a clear effect on flame temperature and thus on NO_x production.

As deduced from the large-scale flame characteristics in Section 5.2, the characteristic strain rate at the tip of the FPJ flame is lower than in a non-precessing jet flame. It is noted that the reduced strain rate also deduced to occur in high St_d MPJ flames relative to the simple jet flames correlates with reduced NO_x emissions and increased emissivity (Nathan *et al.*, 1996). This trend is the opposite of that found by Røkke *et al.* (1992 and 1994) in an examination of a wide range of free turbulent jet diffusion flames. An explanation of this seeming contradiction may be found in the difference in the mixing character of the two types of jet flows and the resulting effect on the dominant combustion mechanisms. A lifted turbulent jet diffusion flame is typically stabilised some ten to twenty jet throat diameters downstream from the nozzle tip, in a region where the turbulence properties (eg. mean and RMS velocity profiles, energy spectra) have reached or are approaching self-similarity. Thus it may be deduced that the mixing characteristics (eg. the spectrum of mixing scales and local fine-scale strain rates) which propagate throughout a flame are generally similar. This argument applies for the flames examined by Røkke *et al.* (1992 and 1994). (In contrast, as discussed later, the turbulence characteristics of simple jet flames are different from those in the FPJ flames). For the simple jet flames the mixing characteristics depend principally on jet diameter and exit velocity for a given type of fuel.

Røkke *et al.* (1992 and 1994) have characterised the NO_x emissions from simple jet diffusion flames of methane, propane and natural gas and partly premixed flames of propane from a strained flamelet model of combustion. Their model postulates that radiation effects on flame temperature are less significant than the influences of finite rate chemical kinetics. From this model they derive scaling relations based on a characteristic strain rate at the tip of the flame (Røkke *et al.*, 1994). Their theory predicts that the NO_x emissions scale as

$$E_{\mathrm{NO_x}} = 8Fr^{\frac{3}{5}}Y_f^{-\frac{1}{5}}\left(\frac{d_0^{0.55}}{\rho_0 u_0}\right) \quad \left[\frac{\mathrm{g\ NO_x}}{\mathrm{kg\ fuel}}\right]$$

with Fr being the Froude number (u_0^2/gd_0) and Y_f being mass fraction of the fuel. In this model $d^{0.55}/u_0$ can be considered to be the inverse of a modified strain rate. That is, decreased strain rate and the subsequent reduction of the scalar dissipation acts to increase the importance of the Zeldovich mechanism relative to the prompt mechanism by increasing temperatures and to increase NO_x formation by making the reaction zone thinner, resulting in a higher flame temperature. Their prediction was shown to agree well with measurements for partly premixed flames, where the mixing characteristics of the flow are deduced to be closely self-similar for all flames.

By contrast the turbulence characteristics at the region of flame stabilisation in precessing jet flows are far from self-similar (Section 3.4) and the turbulence properties there differ drastically from those in simple jet flows (Schneider *et al.*, 1997a and 1997b, and Nathan *et al.*, 1997). The data presented in Section 5.2 demonstrates that jet precession acts to reduce the characteristic strain rate at the tip of the flame. This trend, taken together with the increased radiant fraction associated with high St_d MPJ flames (Nathan *et al.*, 1996), suggests that the effect of radiation on the temperature of methane and propane jet flames can become significant when strain rate characteristics are modified sufficiently. This finding is entirely consistent with the trend found by Kent and Bastin (1984).

5.5. Summary

Precession of a jet is shown to reduce the strain rate at the tip of an open FPJ flame compared with a simple jet flame. It is argued here that the reduced strain increases the sooting tendency and so results in the subsequent increase in the radiant fraction that was measured by Nathan *et al.* (1996). The correlation is consistent with trends found by Kent and Bastin (1984) for simple jet diffusion flames, where the strain is characterised by the throat velocity and diameter. The decrease in the NO_x emissions has previously been found to correlate with an increase in global residence time and reduction in the temperature of the gases in the flame (Nathan *et al.*, 1996). The present work demonstrates that the local strain rate in FPJ flames is reduced by an order of magnitude relative to momentum dominated simple jet flames and this difference is shown to correlate with reduced NO_x emissions and increased emissivity measured by Nathan *et al.* (1996). This trend is the opposite of that found by Røkke *et al.* (1992 and 1994) for free turbulent jet flames. This strongly implies that the effect of radiation on the temperature of jet flames can become significant when the similarity characteristics of jet turbulence characteristics are modified to reduce the strain rate.

Chapter 6

6. Conclusions

6.1. Experimental Results

A wide range of qualitative and quantitative experimental techniques have been used to investigate the effect of precession on a simple turbulent jet flow. Of special interest have been the mixing and combustion characteristics of the flow. Here precession of the jet flow results from the addition of the chamber section downstream from the throat of the simple jet. A fluid mechanical instability is generated in the chamber and this causes the emerging jet to precess. The nozzle is termed the fluidic precessing jet (FPJ) nozzle. FPJ flows and flames have been investigated for nozzles that have an optimal geometry to generate precession reliably (Hill *et al.*, 1992) and which are similar to the commercial burner configuration (Rapson *et al.*, 1995).

Changes to jet mixing characteristics in the non-reacting flow have been determined in the region downstream from the nozzle by use of flow visualisation in water, particle image velocimetry in water and jet concentration measurements in air. These techniques have also been used to resolve large-scale dynamic motions, instantaneous planar velocity measurements, statistical properties of jet concentration in the flow, macroscopic length-scales and the scalar mixing rate. Together they have been used to characterise changes to turbulent mixing in jet flows that result from precession of the jet.

Mixing and combustion characteristics have been determined from visualisation of the flame envelope, from reaction zone imaging and from non-reacting jet concentration measurements. These techniques have allowed gross fluid motions in the flame, the structure of the reaction zone and indicative jet concentration statistics to be resolved in the flame stabilisation region. The roles of mixing and combustion characteristics in the stabilisation have been assessed in relation to the mechanisms that have been proposed by others for simple jet diffusion flames.

The significance of changes in the mixing characteristics that result from precession of a jet is also considered in relation to soot formation and NO_x emission characteristics. Based on the above findings a mechanism for the simultaneous reduction of NO_x emissions and increase of radiant heat transfer observed in precessing jet gas flames has been proposed.

6.1.1. Mixing in Precessing Jet Flows

Qualitative and quantitative experimental data have been used to characterise the effect of precession on the mixing of a simple turbulent jet flow with its surrounding ambient fluid. New experimental results obtained from planar flow visualisations, planar velocity measurements and quantitative planar jet concentration measurements allow the precession induced changes to jet mixing downstream from the nozzle to be assessed with a degree of rigour which has not been provided previously.

Flow visualisation of the FPJ flow has demonstrated the existence of large-scale structures that are responsible for entrainment of significant quantities of ambient fluid. Velocity measurements demonstrate that there is a dramatic reduction in the flow velocities, by two orders of magnitude relative to the jet throat, in the region immediately downstream from the nozzle.

Statistical properties of the jet concentration have been obtained with high temporal and spatial resolution that resolves the Batchelor-scale in the far field of the jet. The data shows that the present simple jet which issues from a sharp edged orifice plate (ie. without the FPJ chamber) is characterised by:

- symmetry in the mean and RMS jet concentrations about the jet axis, and linear relationships in mean parameters with axial distance, as reported by others,
- a potential core which extends along the jet axis to $x \approx 3d$,
- an increase in the rate of decay of mean jet concentration along the jet axis by a factor of approximately two compared with the jet issuing from the smooth contraction nozzle investigated by Becker *et al.* (1967),
- an asymptotic half-width spreading angle of 6.6°, compared with 6.0° reported by Becker *et al.* (1967),
- radial mean and RMS jet concentration profiles that are consistent with a

marginally wider spreading angle than that found by Becker *et al.* (1967),

- self-similarity of the radial mean jet concentration for $x \geq 20d$,
- self-similarity of the radial RMS jet concentration for $x \geq 80d$, and
- an increase in the asymtotic unmixedness value $\xi_{RMS} = 0.3\overline{\xi}$ on the jet axis compared with $\xi_{RMS} = 0.22\overline{\xi}$ found by Becker *et al.* (1967).

These characteristics demonstrate that the mixing processes throughout a jet from a sharp edged orifice are different from those of a jet from a nozzle with a smooth contraction.

Precession, caused by the addition of the FPJ nozzle chamber downstream from the simple orifice, causes the scalar mixing field to change from that produced by the simple jet in the following ways:

- the mean jet concentration along the jet axis is increased by a factor of 2 (ie. the centre-line decay rate is halved),
- the half-width spreading angle is increased from 6.6° to 11°,
- the distance required to achieve self-similarity of the radial mean jet concentration is increased to $(x - L) \approx 40d_1$,
- the downstream distance required to achieve self-similarity of the radial RMS jet concentration is increased so that full similarity is approached but not reached within the imaged region $(x - L) \leq 110d_1$,
- the unmixedness is increased everywhere along the jet axis by about 50%,
- the distribution of mixed fluid concentrations that can exist on the jet axis is broadened,
- the intermittency on the jet axis demonstrating the existence of "pure" ambient fluid along the axis is increased,
- the macroscopic mixing length-scales are increased and in particular the axial integral length-scale of the concentration fluctuations is increased by a factor of 2.0,

- the scalar mixing rate on the jet axis is increased by an order of magnitude.
- the strain rate in the transition region and far field, as deduced from the reduction in the aspect ratio of the elliptical R correlation contours is decreased from 1.7:1 in a simple jet flow to 1.4:1 in a FPJ flow.

The above findings support the concept that the effect of precession is to change the underlying structure of the turbulence in a manner that reduces the magnitude of the local strain rate in the flow. Taken together with the results of the present simple jet issuing from an orifice, and the jet investigated by Becker *et al.* (1967) issuing from a smooth contraction, it is clear that the structure of the turbulence (in particular the distribution of turbulent length-scales) at the exit of the nozzle propagates through the entire jet and determines the statistical description of the scalar mixing field in both the near field (developing region) and the far field (asymptotic region). These results also demonstrate conclusively that *the effect of precession of a jet is to enhance large-scale engulfment of ambient fluid and to suppress fine-scale mixing between the jet and ambient fluid streams.*

6.1.2. Stabilisation Mechanisms in Precessing Jet Flames

Qualitative and quantitative experimental data have been used to investigate stabilisation of FPJ flames. Mixing and combustion characteristics of precessing jet flows have been assessed from visualisation of the flame envelope, reaction zone imaging and jet concentration measurements of the non-reacting jet.

The models of physical mechanisms responsible for jet flame stabilisation, which predict flame lift-off and blowout behaviour in simple free jet flames, are considered in relation to FPJ flames. The physical combustion criteria considered in each of the principal flame stabilisation models which have been proposed for simple jet flames are:

- Vanquickenborne and van Tiggelen (1966) propose that stabilisation occurs along the stoichiometric contour, that results from the mixing upstream from the flame front.
- Peters and Williams (1983) suggest that there is insufficient time for significant premixing to occur upstream from the flame front and propose that stabilisation occurs in flamelets that are thin relative to the dissipation scales.
- Broadwell *et al.* (1984) propose that the flame must propagate from one large-scale coherent structures to its next upstream neighbour.
- Bilger (1988) proposes that reaction zones at the base of the flame will be thicker than the Kolmogorov scale and are centred very near to the stoichiometric contour so that they have an appearance of flamelets along the contour.
- Bish *et al.* (1995) relate the chemical state of combustion to the mixing state of a conserved scalar. The presence of layer-like scalar dissipation structures in the mixing field is related to a locally one-dimensional structure in the underlying chemical species fields.

The findings presented here have been considered in relation to the possible stabilisation mechanisms by considering the validity of the proposed mixing and combustion characteristics. Large-scale buoyant structures, which propagate through the unconfined FPJ flames, are concluded to be the result of, rather than the cause of, the flame stabilisation. It has been demonstrated that combustion occurs in reaction zones that are located at the edge of the flow field rather than distributed throughout a large-scale structure. The instantaneous structure of the reaction field can be seen, qualitatively, to coincide with the structure of the flammable region in the non-reacting flow case. The reaction layers are thick compared with the thickness of dissipation layers. High scalar dissipation is restricted to the jet emerging from the FPJ nozzle, which is well upstream of the mean stabilisation point.

These above results demonstrate conclusively that *the physical mechanisms discussed above which have been proposed for simple jet flame stabilisation ,other than those which include the existence of a premixed flame zone, are inappropriate for the fluidic precessing jet diffusion flame*. That is, stabilisation depends upon the mixing characteristics upstream from the reaction zone to provide regions of sufficiently low velocity that are within the flammability limits.

6.1.3. The Influence of Mixing on Sooting and NO_x Emission Characteristics of Precessing Jet Flames

Precession of a jet is shown to reduce the strain rate at the tip of an open FPJ flame compared with a simple jet flame by an order of magnitude compared with momentum dominated flames. Here the strain rate at the flame tip has been measured directly from the characteristic celerity and width of the large-scale structures at the tip of the flame. It has been calculated for the simple jet flames from the data of Mungal *et al.* (1991) who used the same measurement technique. At the same time the global residence time is increased. It is argued here that the reduced strain rate and increased residence time increases the sooting tendency and so results in a subsequent increase in the radiant fraction and reduction in flame temperature in precessing jet flames. The argument extends the findings of Turns and Myhr (1991) who found that a decrease in global NO_x emissions correlates with increased radiant fraction and decreased global residence time. Nathan *et al.* (1996) found a similar trend when the radiant fraction and the global residence time are altered by changes in the mixing, but did not quantify strain rate directly. The reduced strain rate measured in the present work in FPJ flames relative to the simple jet flames is shown to correlate with reduced NO_x emissions and increased emissivity. This trend is the opposite from that found from laminar flamelet calculations of unconfined turbulent jet flames. It strongly implies that the effect of radiation on the temperature of jet flames can become significant when the structure of jet turbulence, and hence the mixing characteristics, have been modified to reduce the characteristic strain rate of the reacting flow. It also provides a mechanism whereby NO_x emissions can be reduced and radiant heat transfer increased simultaneously by proper control of turbulent mixing parameters.

6.2. Further Work

6.2.1. Mixing in Reacting Precessing Jet Flows

The present work has shown that precession of a jet changes the scalar mixing field in the non-reacting flow significantly. Further work should therefore be directed towards identifying how the reacting flow differs from the non-reacting precessing jet flow. It is apparent that the volumetric expansion and the heat release of combustion will cause changes to the mixing field in the reacting flow. It is necessary to use a technique that employs a tracer that is not consumed by combustion or that allows direct imaging of the fuel species. It has been demonstrated that the mixing in the non-reacting precessing jet flow is dominated by coherent motions so that knowledge of the spatial mixing field is necessary.

6.2.2. Stabilisation in the Precessing Jet Flow

The current investigation of FPJ flames has identified that the FPJ flame is likely to be stabilised by a reaction zone that contains low velocity regions of fluid mixtures that are within the flammability limits of the fuel. The present study has not determined the instantaneous local flow and mixing environment in the stabilisation region of the precessing jet flame. The structure of the fuel species, temperature, reaction and velocity fields are required to determine the underlying physical stabilisation mechanism. Such data enables the determination of the flammable, dissipation, and strain rate fields, which have all been considered in models for simple jet flames. It is possible that there are significant differences between the physical structures of the reaction zones in simple jet flames and precessing jet flames.

Chapter 7

7. Publications Originating from This Thesis

1. Newbold, G.J.R., Nathan, G.J., and Luxton, R.E. (1993a). Large scale motions in an unconfined precessing jet diffusion flame. *The Australian Symposium on Combustion/Third Flame Days.* University of Newcastle, Australia, November 1-2, A5, 1-4.
2. Newbold, G.J.R., Nathan, G.J., and Luxton, R.E. (1993b). Large scale dynamics of the precessing jet flame. *Fifth Australasian Heat and Mass Transfer Conference.* The University of Queensland, Australia, December 6-9, 46.1-46.6.
3. Newbold, G.J.R., Nobes, D.S., Alwahabi, Z.T., Nathan, G.J., and Luxton, R.E., (1995). The application of PIV to the precessing jet nozzle. *Twelfth Australasian Fluid Mechanics Conference.* The University of Sydney, Australia, December 10-15, 395-398.
4. Newbold, G.J.R., Nobes, D.S., Nathan, G.J., Luxton, R.E., Alwahabi, Z.T., and King, K.D. (1996). Visualisation and mixing in the precessing jet flow. *First Australian Conference on Laser Diagnostics in Fluid Mechanics and Combustion.* The University of Sydney, Australia, December 5-6, 253.
5. Newbold, G.J.R., Nathan, G.J., and Luxton, R.E. (1997a). Large-scale dynamics of an unconfined precessing jet flame. *Comb. Sci. Tech.*, 126(1-6), 53.
6. Newbold, G.J.R., Nobes, D.S., Nathan, G.J., Luxton, R.E., Alwahabi, Z.T., and King, K.D. (1997b). Reaction and flow field in the stabilisation region of a fluidic precessing jet flame. *The Australian Symposium on Combustion Fifth Flame Days.* The University of Sydney, Australia, November 20-21.
7. Nobes, D.S., Newbold, G.J.R., Nathan, G.J., Luxton, R.E., Alwahabi, Z.T., and King,

K.D. (1997). The mixing field of a simple round jet and a fluidic precessing jet. *The First Asia-Pacific Conference on Combustion.* Osaka University, Japan, May 12-15, 334-337.

Chapter 8.

8. References

1. Abramovich, G.N. (1963). *The theory of turbulent jets.* MIT Press, Cambridge, Massachusetts.
2. Adrian, R.J. (1991). Particle-imaging techniques for experimental fluid mechanics. *Ann. Rev. Fluid Mech.*, 23, 261-301.
3. Agui, J.C., and Jiménez, J. (1987). On the performance of particle tracking. *J. Fluid Mech.*, 185,447-468.
4. Alwahabi, Z.T., King, K.D., Nathan, G.J., Nobes, D.S., Newbold, G.J.R., and Luxton, R.E. (1996). Planar laser induced fluorescence studies of OH and CH radicals in precessing jet flames. *First Australian Conference on Laser Diagnostics in Fluid Mechanics and Combustion.* The University of Sydney, Australia, December 5-6, 252.
5. Alwahabi, Z.T., King, K.D., Nathan, G.J., Nobes, D.S., Newbold, G.J.R., and Luxton, R.E. (1997). Planar laser induced fluorescence studies of radicals in precessing jet flames. *Chemeca*, Rotorua, New Zealand, September 29 – October 1.
6. Batchelor, G.K. (1959). Small-scale variation of convected quantities like temperature in turbulent fluid: Part 1. General discussion and the case of small conductivity. *J. Fluid Mech.*, 5, 113-133.
7. Becker, H.A., Hottel, H.C., and Williams, G.C. (1967). The nozzle-fluid concentration field of the round, turbulent, free jet. *J. Fluid Mech.*, 30(2), 285-303.
8. Becker, H.A., and Yamazaki, S. (1977). Soot concentration field of turbulent propane/air diffusion flames. *Sixteenth Symposium (International) on Combustion*, The

Combustion Institute, 681-691.

9. Berlman, I.B. (1971). *Handbook of fluorescence spectra of aromatic molecules.* Academic Press, New York. Second Edition.

10. Bilger, R.W. (1976). The structure of diffusion flames. *Comb. Sci. Tech*, 13, 155-170.

11. Bilger, R.W. (1988). The structure of turbulent nonpremixed flames. *Twenty-Second Symposium (International) on Combustion*, The Combustion Institute, 475-488.

12. Bish, E.S., and Dahm, W.J.A. (1995). Strained dissipation and reaction layer analyses of nonequilibrium chemistry in turbulent reacting flows. *Comb. Flame*, 100,457-464.

13. Boerstoel, G.P., Wieringa, J.A., van der Meer, T.H., and Hoogendoorn, C.J. (1994). Numerical modelling of soot formation in glass melting furnaces. *EUROTHERM*. ENEA Research Centre, Saluggia, Italy, 5-7 October.

14. Boerstoel, G.P., van der Meer, T.H., and Hoogendoorn, C.J. (1995). Numerical simulation of soot-formation and –oxidation in high temperature furnaces. *Eighth International Symposium on Transport Phenomena in Combustion.* San Francisco, USA, July.

15. Bremhorst, K., and Hollis, P.G. (1990). Velocity field of an axisymmetric pulsed, subsonic air jet. *AIAA J.*, 28, 2043-2049.

16. Broadwell, J.E., Dahm, W.J.A., and Mungal, M.G. (1984). Blowout of turbulent diffusion flames. *Twentieth Symposium (International) on Combustion*, The Combustion Institute, 303-310.

17. Buch, K.A., Dahm, W.J.A., Dibble, R.W., and Barlow, R.S. (1992). Structure and equilibrium reaction rate fields in turbulent jet diffusion flames. *Twenty-Fourth Symposium (International) on Combustion*, The Combustion Institute, 295-301.

18. Buch, K.A., and Dahm, W.J.A. (1996). Experimental study of the fine-scale structure of conserved scalar mixing in turbulent shear flows. Part I. *Sc* >> 1. *J. Fluid Mech.*, 317, 21-71.

19. Byggstøyl, S., and Magnussen, B.F. (1985). A model for flame extinction in turbulent flow. *Turbulent Shear Flows 4* (Ed. L.J.S. Bradbury *et al.*), Springer, 381-395.

20. van Cruyningen, I., Lozano, A., and Hanson, R.K. (1989). Interpretation of planar laser-induced fluorescence flow field images. *Flow Visualisation*, Winter Annual Meeting of the ASME, San Fransisco, USA, December 10-15, 109-114.

21. van Cruyningen, I., Lozano, A., and Hanson, R.K. (1990). Quantitative imaging of concentration by planar laser-induced fluorescence. *Expt. Fluids*, 10, 41-49.

22. van Cruyningen, I., Lozano, A., Mungal, M.G., and Hanson, R.K. (1991). Three-dimensional visualisation of temporal flow sequences. *AIAA Journal*, 29, 479-482.

23. Cetegen, B.M., and Ahmed, T.A. (1993). Experiments on the periodic instability of buoyant plumes and pool fires. *Comb. Flame*, 93, 157-184.

24. Chen, L.-D., and Roquemore, W.M. (1986). Visualisation of jet flames. *Comb. Flame*, 66, 81-86.

25. Chen, L.-D., Seaba, J.P., Roquemore, W.M., and Goss, L.P. (1988). Buoyant diffusion flames. *Twenty-Second Symposium (International) on Combustion*, The Combustion Institute, 677-684.

26. Dahm, W.J.A., Southerland, K.B., and Buch, K.A. (1991). Direct, high resolution, four-dimensional measurement of the fine scale structure of Sc>>1 molecular mixing in turbulent flows. *Phys. Fluids A*, 3(5), 1115-1127.

27. Dahm, W.J.A., and Dimotakis, P.E. (1987). Measurements of entrainment and mixing in turbulent jets. *AIAA Journal*, 25(9), 1216-1223.

28. Dimotakis, P.E., Miake-Lye, R.C., and Papantoniou, D.A. (1983). Structure and dynamics of round turbulent jets. *Phys. Fluids*, 26(11), 3185-3192.

29. Dowling, D.R., and Dimotakis, P.E. (1990). Similarity of the concentration of gas-phase turbulent jets. *J. Fluid Mech.*, 218, 109-141.

30. Dyer, M.J., and Crosley, D.R. (1982). Two-dimensional imaging of OH laser-induced

fluorescence in a flame. *Opt. Let.*, 7(8), 382-384

31. Eickhoff, H., and Winandy, A. (1985). Visualisation of vortex formation in jet diffusion flames. *Comb. Flame*, 60, 99-101.

32. Escoda, M.C., and Long, M.B. (1983). Rayleigh scattering measurements of the gas concentration field in turbulent jets. *AIAA Journal*, 21(1), 81-84.

33. Feikema, D.A., Everest, D., and Driscoll, J.F. (1996). Images of dissipation layers to quantify mixing within a turbulent jet. *AIAA Journal*, 34(12), 2531-2538.

34. Glassman, I. (1987). *Combustion*, Academic Press, Second Edition.

35. Hill, S.J., Nathan, G.J., and Luxton, R.E. (1992). Precessing and axial flows following a sudden expansion in an axisymmetric nozzle. *Eleventh Australasian Fluid Mechanics Conference*, University of Tasmania, Hobart, Australia, 14-18 December, 1113-1116.

36. Hill, S.J., Nathan, G.J., and Luxton, R.E. (1995). Precession in axisymmetric confined jets. *Twelfth Australasian Fluid Mechanics Conference*, The University of Sydney, Australia, December 10-15, 135-138.

Not published [illegible] Invalid

37. Hill, S.J. (1998). Precession in flows through axisymmetric sudden expansions. *Ph.D. Thesis*, The University of Adelaide, Australia.

38. Horch, K. (1978). *Ph.D. Thesis*, Universität Karlsruhe.

39. Jenkins, B.G., Nathan, G.J., and Manias, C.G., (1995). Modelling of precessing jet burners and their application to rotary alumina kilns. *Third International Conference on Combustion Technologies for a Clean Environment*, July.

40. Kalghatgi, G.T. (1981). Blow-out stability of gaseous jet diffusion flames. Part I: In still air. *Combust. Sci. Tech.*, 26, 233-239.

41. Kalghatgi, G.T. (1984). Lift-off heights and visible lengths of vertical turbulent jet diffusion flames in still air. *Combust. Sci. Tech.*, 41, 17-29.

42. Karasso, P.S., and Mungal, M.G. (1996). Scalar mixing and reaction in plane liquid shear layers. *J. Fluid Mech.*, 323, 23-63.

43. Kent, J.H., and Bastin, S.J. (1984). Parametric effects on sooting in turbulent acetylene diffusion flames. *Comb. Flame*, 56, 29-42.

44. Koochesfahani, M.M., Dimotakis, P.E., and Broadwell, J.E. (1985). A "flip" experiment in a chemically reacting mixing layer. *AIAA Journal*, 23(8), 1191-1194.

45. Koochesfahani, M.M., and Dimotakis, P.E. (1985). Laser-induced fluorescence measurements of mixed fluid in a liquid plane shear layer. *AIAA Journal*, 23(11), 1700-1707.

46. Koochesfahani, M.M., and Dimotakis, P.E. (1986). Mixing and chemical reaction in a turbulent liquid mixing layer. *J. Fluid Mech.*, 170, 83-112.

47. Kychakoff, G., Hanson, R.K., and Howe, R.D. (1984). Simultaneous multi-point measurements of OH in combustion gases using planar laser-induced fluorescence. *Twentieth Symposium (International) on Combustion*, The Combustion Institute, 1265-1272.

48. Lin, C-K., Jeng, M-S., and Chao, Y-C. (1993). The stabilisation mechanism of the lifted jet diffusion flame in the hysteresis region. *Expt. Fluids*, 14, 353-365.

49. Luxton, R.E., Nathan, G.J., and Luminis Pty. Ltd. (1991). *Controlling the motion of a fluid jet.* USA Letters Patent No.5,060,867.

50. Manias, C.G., and Nathan, G.J. (1993). The precessing jet gas burner – a low NOx burner providing process efficiency and product quality improvements. *World Cement*, March, 24(3), 4-11.

51. Manias, C.G., and Nathan, G.J. (1994). Low NOx clinker production. *World Cement*, May, 25(5), 54-56.

52. Monin, A.S., and Yaglom, A.M. (1975). *Statistical fluid mechanics.* MIT Press.

53. Mungal, M.G., and O'Neil, J.M. (1989). Visual observations of a turbulent diffusion flame. *Comb. Flame* 78, 377-389.

54. Mungal, M.G., Karasso, P.S., and Lozano, A. (1991). The visible structure of turbulent

jet diffusion flames: Large-scale organisation and flame tip oscillation. *Comb. Sci. Tech.*, 76, 165-185.

55. Mungal, M.G., Lozano, A., and van Cruyningen, I. (1992). Large-scale dynamics in high Reynolds number jets and jet flames. *Expt. Fluids*, 12, 141-150.
56. Muñiz, L., and Mungal, M.G. (1997). Instantaneous flame-stabilisation velocities in lifted-jet diffusion flames. *Comb. Flame*, 111, 16-31.
57. Namazian, M., Schefer, R.W., and Kelly, J. (1988). Scalar dissipation measurements in the developing region of a jet. *Comb. Flame*, 74, 147-160.
58. Namazian, M., Kelly, J., and Schefer, R.W. (1992). Concentration imaging measurements in turbulent concentric-jet flows. *AIAA Journal*, 30(2), 384-393.
59. Nathan, G.J. (1988). The enhanced mixing burner. *Ph.D. Thesis*, The University of Adelaide, Australia.
60. Nathan, G.J., and Luxton, R.E. (1991a). Flame stability and emission characteristics of the enhanced mixing burner. *Second European Conference on Industrial Furnaces and Boilers,* Algarve, Portugal, April 2-5, vol 1.
61. Nathan, G.J., and Luxton, R.E. (1991b). Mixing enhancement by a self-exciting, asymmetric precessing flow-field. *Fourth International Symposium on Transport Phenomenon* (Ed. Reizes, J.A.), Sydney, Australia, July 14-19, 1297-1037. Elsevier.
62. Nathan, G.J., and Luxton, R.E. (1991c). The entrainment and combustion characteristics of an axi-symmetric, self exciting, enhanced mixing nozzle. *Third ASME/JSME Thermal Engineering Proceedings*, Reno, USA, March 17-22, vol. 5, 145-152.
63. Nathan, G.J., Luxton, R.E., and Smart, J.P. (1992). Reduced NO_x emissions and enhanced large scale turbulence from a precessing jet burner. *Twenty-Fourth Symposium (International) on Combustion*, The Combustion Institute, 1399-1405.
64. Nathan, G.J., and Luxton, R.E. (1992). A low NO_x gas burner with a radiant flame.

International Conference on Energy Efficiency in Process Technology, Athens, Greece, October 19-22, 883-892. Elsevier.

65. Nathan, G.J., Turns, S.R., and Bandaru, R.V. (1996). The influence of fuel jet precession on the global properties and emissions of unconfined turbulent flames. *Comb. Sci. Tech.*, 112, 211-230.

66. Nathan, G.J., Nobes, D.S., Mi. J.C., Schneider, G.M., Newbold, G.J., Alwahabi, Z.T., Luxton, R.E., and King, K.D. (1997). Exploring the relationship between mixing, radiation and NOx emissions from natural gas flames. *Combustion and Emissions Control III*, The Institute of Energy, 49-69.

67. Nathan, G.J., Hill, S.J, and Luxton, R.E. (1998). An axisymmetric 'fluidic' nozzle to generate jet precession. *J. Fluid Mech.*, accepted for publication.

68. Newbold, G.J.R., Nathan, G.J., and Luxton, R.E. (1993a). Large scale motions in an un-confined precessing jet diffusion flame. *The Australian Symposium on Combustion/Third Flame Days.* University of Newcastle, Australia, November 1-2, A5, 1-4.

69. Newbold, G.J.R., Nathan, G.J., and Luxton, R.E. (1993b). Large scale dynamics of the precessing jet flame. *Fifth Australasian Heat and Mass Transfer Conference.* The University of Queensland, Australia, December 6-9, 46.1-46.6.

70. Newbold, G.J.R., Nobes, D.S., Alwahabi, Z.T., Nathan, G.J., and Luxton, R.E., (1995). The application of PIV to the precessing jet nozzle. *Twelfth Australasian Fluid Mechanics Conference,* The University of Sydney, Australia, December 10-15, 395-398.

71. Newbold, G.J.R., Nobes, D.S., Nathan, G.J., Luxton, R.E., Alwahabi, Z.T., and King, K.D. (1996). Visualisation and mixing in the precessing jet flow. *First Australian Conference on Laser Diagnostics in Fluid Mechanics and Combustion.* The University of Sydney, Australia, December 5-6, 253.

72. Newbold, G.J.R., Nathan, G.J., and Luxton, R.E. (1997a). Large-scale dynamics of an

unconfined precessing jet flame. *Comb. Sci. Tech.*, 126(1-6), 53.

73. Newbold, G.J.R., Nobes, D.S., Nathan, G.J., Luxton, R.E., Alwahabi, Z.T., and King, K.D. (1997b). Reaction and flow field in the stabilisation region of a fluidic precessing jet flame. *The Australian Symposium on Combustion/Fifth Flame Days.* The University of Sydney, Australia, November 20-21.

74. Nobes, D.S., Newbold, G.J.R., Nathan, G.J., Luxton, R.E., Alwahabi, Z.T., and King, K.D. (1996a). A planar imaging technique for measurement of concentration in a jet. *First Australian Conference on Laser Diagnostics in Fluid Mechanics and Combustion.* Sydney University, Australia, December 5-6, 148-153.

75. Nobes, D.S., Newbold, G.J.R., Nathan, G.J., Luxton, R.E., Alwahabi, Z.T., and King, K.D. (1996b). Phase average planar imaging of concentration of a precessing jet flow. *First Conference on Laser Diagnostics in Fluid Mechanics and Combustion.* The University of Sydney, Australia, December 5-6, 154-159.

76. Nobes, D.S. (1997). The generation of large-scale structures by jet precession. *Ph.D. Thesis*, The University of Adelaide, Australia.

77. Nobes, D.S., Newbold, G.J.R., Nathan, G.J., Luxton, R.E., Alwahabi, Z.T., and King, K.D. (1997). The mixing field of a simple round turbulent jet and a fluidic precessing jet. *The First Asia-Pacific Conference on Combustion.* Osaka University, Japan, May 12-15, 334-337.

78. Peters, N., and Williams, F.A. (1983). Liftoff characteristics of turbulent jet diffusion flames. *AIAA Journal*, 21(3), 423-429

79. Pitts, W.M. (1988). Assessment of theories for the behaviour and blowout of lifted turbulent diffusion flames. *Twenty-Second Symposium (International) on Combustion*, The Combustion Institute, 809-816.

80. Pitts, W.M. (1989). Importance of isothermal mixing processes to the understanding of lift-off and blowout of turbulent jet diffusion flames. *Comb. Flame*, 76, 197-212.

81. Pitts, W.M. (1990). Large-scale turbulent structures and the stabilisation of lifted turbulent jet diffusion flames. *Twenty-Third Symposium (International) on Combustion*, The Combustion Institute, 661-668.

82. Pitts, W.M. (1991). Effects of global density ratio on the centre-line mixing behaviour of axisymmetric turbulent jets. *Expt. Fluids*, 11, 125-134.

83. Press, W.H., Flannery, B.P., Teukolsky, S.A., and Vetterling W.T. (1986). *Numerical recipes*. Cambridge Press.

84. Rapson, D., Stokes, B., and Hill, S.J. (1995). Kiln flame shape optimisation using a Gyro-Therm gas burner. *World Cement*, July, 26, July, 2-5.

85. Røkke, N.A., Hustad, J.E., Sønju, O.K., and Williams, F.A. (1992). Scaling of nitric oxide emissions from buoyancy-dominated hydrocarbon turbulent-jet diffusion flames. *Twenty-Fourth Symposium (International) on Combustion*, The Combustion Institute, 385-393.

86. Røkke, N.A., Hustad, J.E., and Sønju, O.K. (1994). A study of partially premixed unconfined propane flames. *Comb. Flame*, 97, 88-106.

87. Schefer, R.W., Namazian, M., and Kelly, J. (1988). Structural characteristics of lifted turbulent-jet flames. *Twenty-Second Symposium (International) on Combustion*, The Combustion Institute, 833-842.

88. Schefer, R.W., Namazian, M., and Kelly, J. (1994a). Stabilisation of lifted turbulent-jet flames. *Comb. Flame*, 99, 75-86.

89. Schefer, R.W., Namazian, M., and Kelly, J. (1994b). Temporal evolution of turbulence/chemistry interactions in lifted, turbulent-jet flames. *Twenty-Fifth Symposium (International) on Combustion*, The Combustion Institute, 1223-1231.

90. Schefer, R.W., Kerstein, A.R., Namazian, M., and Kelly, J. (1994c). Role of large-scale structure in a nonreacting turbulent CH_4 jet. *Phys. Fluids*, 6(2), 652-661.

91. Schneider, G.M. (1996). Structures and turbulence characteristics in a precessing jet

flow. *Ph.D. Thesis*, The University of Adelaide, Australia.

92. Schneider, G.M., Hooper, J.D., Musgrove, A.R., Nathan, G.J., and Luxton, R.E. (1997a). Velocity and Reynolds stresses in a precessing jet flow. *Expt. Fluids*, 22, 489-495.

93. Schneider, G.M., Froud, D., Syred, N., Nathan, G.J., and Luxton, R.E. (1997b). Velocity measurements in a precessing jet flow using a three dimensional LDA system. *Expt. Fluids*, 23, 89-98.

94. Seitzman, J.M., Üngüt, A., Paul, P.H., and Hanson, R.K. (1990). Imaging and characterisation of OH structures in a turbulent nonpremixed flame. *Twenty-Third Symposium (International) on Combustion*, The Combustion Institute, 637-644.

95. Sutalo, I.D., Harris, J.A., Jorgensen, F.R.A., and Gray, N.B. (1993). An experimental and numerical study of a flash smelting burner. *Fifth Australasian Heat and Mass Transfer Conference*, The University of Queensland, Brisbane, Australia, 6-9 December, 50.1–50.6.

96. Sutalo, I.D., Harris, J.A., Jorgensen, F.R.A., and Gray, N.B. (1994). An unstable jet in a water model of a flash smelting burner. *International Colloquium on Jets, Wakes and Shear Layers*, CSIRO-DBCE, Highett, Melbourne, Australia, April 18-20, 31.

97. Thring, M.W., and Newby, M.P. (1953). Combustion length of enclosed turbulent jet flames. *Fourth Symposium (International) on Combustion*, The Combustion Institute, 789-796.

98. Turns, S.R., and Myhr, F.H. (1991). Oxides of nitrogen emissions from turbulent jet flames: Part I – Fuel effects and flame radiation. *Comb. Flame*, 87, 319-335.

99. Turns, S.R., Myhr, F.H., Bandaru, R.V., and Maund, E.R. (1993). Oxides of nitrogen emissions from turbulent jet flames: Part II – Fuel dilution and partial premixing effects. *Comb. Flame*, 93, 255-269.

100. Turns, S.R., Bandaru, R.V., and Nathan, G.J. (1994). Oxides of nitrogen emissions

from turbulent hydrocarbon/air jet diffusion flames. *Annual Report*, Dept. Mech. Eng., for the Gas Research Institute. GRI Contract No. 5092-260-2596.

101. Vanquickenborne, L., and van Tiggelen, A. (1966). The stabilisation mechanism of lifted diffusion flames. *Comb. Flame*, 10, 59-69.

102. Versluis, M., Boogaarts, M., Klein-Douwel, R., Thus, B., de Jongh, W. Braam, A., ter Meulen, J.J., Meerts, W.L., and Meijer, G. (1992). Laser-induced fluorescence imaging in a 100kW natural gas flame. *App. Phys. B*, 55, 164-170.

103. Ward, D.E., Nathan, G.J., Luxton, R.E., and Truce, R.J., (1990). An enhanced mixing PF burner for the QEC Swanbank-A Power Station. *First Australian Flame Days*, Brisbane, December.

104. Weckman, E.J., and Sobiesiak, A. (1988). The oscillatory behaviour of medium-scale pool fires. *Twenty-Second Symposium (International) on Combustion*, The Combustion Institute, 1299-1310.

105. Willert, C.E., and Gharib, M. (1991). Digital particle image velocimetry. *Expt. Fluids*, 10, 181-193

106. Yoda, M., and Hesselink, L. (1990). A three-dimensional visualisation technique applied to flow around a delta wing. *Expt. Fluids.*, 10, 102-108.

107. Yoda, M., Hesselink, L., and Mungal, M.G. (1994). Instantaneous three-dimensional concentration measurements in the self-similar region of a round high-Schmidt-number jet. *J. Fluid Mech.*, 279, 313-350.

108. Zukoski, E.E., Kubota, T., and Cetegen, B.M. (1980). Entrainment in fire plumes. *Fire Safety Journal*, 3, 107-121.

109. Zukoski, E.E., Cetegen, B.M., and Kubota, T. (1984). Visible structure of buoyant diffusion flames. *Twentieth Symposium (International) on Combustion*, The Combustion Institute, 361-366.